

Universidade de São Paulo  
Instituto de Física

## Condensados na casca esférica: misturas e ondas de Faraday

Leonardo Brito da Silva

Orientador: Prof. Dr. Arnaldo Gammal

Tese de doutorado apresentada ao Instituto de Física da  
Universidade de São Paulo como requisito parcial para obtenção  
do título de Doutor em Ciências.

Banca Examinadora:

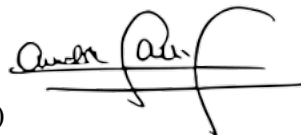
Prof. Dr. Arnaldo Gammal - Orientador (IFUSP)

Prof. Dr. Aristeu Rosendo Pontes Lima (UNILAB)

Prof. Dr. Emanuel Henn (IFSC/USP)

Prof. Dra. Marijana Brtko (UFABC)

Prof. Dr. Marcelo Martinelli (IFUSP)



São Paulo  
2023

**FICHA CATALOGRÁFICA**  
**Preparada pelo Serviço de Biblioteca e Informação**  
**do Instituto de Física da Universidade de São Paulo**

Silva, Leonardo Brito da

Condensados na casca esférica: misturas e ondas de Faraday. São Paulo, 2023.

Tese (Doutorado) - Universidade de São Paulo. Instituto de Física. Depto. de Física Experimental.

Orientador: Prof. Dr. Arnaldo Gammal

Área de Concentração: Condensados de Bose-Einstein

Unitermos: 1. Condensado de Bose-Einstein; 2. Misturas de condensados; 3. Armadilha de bolha; 4. Ondas de Faraday.

USP/IF/SBI-049/2023

University of São Paulo  
Institute of Physics

Condensates on the spherical shell:  
mixtures and Faraday waves

Leonardo Brito da Silva

Advisor: Prof. Dr. Arnaldo Gammal

Ph.D. thesis submitted to the Physics Institute of the University  
of São Paulo in partial fulfillment of the requirements for the  
degree of Doctor of Science.

Examining Committee:

Prof. Dr. Arnaldo Gammal - Advisor (IFUSP)

Prof. Dr. Aristeu Rosendo Pontes Lima (UNILAB)

Prof. Dr. Emanuel Henn (IFSC/USP)

Prof. Dra. Marijana Brtko (UFABC)

Prof. Dr. Marcelo Martinelli (IFUSP)

São Paulo  
2023



# Acknowledgments

I acknowledge the Brazilian agency Coordenação de Aperfeiçoamento de Pessoal de Nível Superior (CAPES) for financial support, Proc. 88887.374855/2019-00. I thank the institutional committee Comissão de Pós-Graduação (CPG) of the Institute of Physics (IFUSP) for all support, and specially financial support for upgrade of my personnel laptop, which was very important to improve my performance in computational simulations.

I thank my advisor Prof. Dr. Arnaldo Gammal for his support and effort in helping me to reach the required level to be able to perform physics simulations and improve my tools, and for his hospitality when I joined the group. I thank the Ph.D. student former colleague Alex Andriati for the cooperation in our common works, for helping me to learn the main research branches of our group, and share his ideas. I also recognize the cooperation and lessons from Prof. Dr. Lauro Tomio when we worked together. I also acknowledge the valuable discussions, cooperation, and pretty good relationship with all my current colleagues of the research group, Raphael Wicky Sallatti, Jonata Santos Soares, and Gustavo Henrique dos Santos Silva.

I also thank Prof. Dr. A. F. R. T. Piza and Prof. Dr. E. J. V. Passos for valuable lessons and discussions in our weekly Journal Club meeting.

# Abstract

We study the stability properties of Bose-Einstein condensate mixtures trapped on the surface of spherical shells. This work is strongly motivated by the recent achievements in the confinement of ultracold gases into shell-shaped two-dimensional geometries in microgravity environments aboard the International Space Station. We observe two main setups. In the first one, we analyze stationary homogeneous and vortex states, settled as a hidden vorticity system, where the vortex states are achieved with opposite vortex charges in each species. In the second one, we study time-periodic spatial-homogeneous states, driven by Rabi oscillations, where each species can convert in the other one. The oscillation frequency can be tuned in order to get parametric resonance. We deeply analyze the role of the interaction parameters and the Rabi coupling on the resulting stability profile of the mixture solutions. Once the instability runs the dynamics, it can lead the atomic clouds to break into a well-defined number of immiscible pieces, and when parametric resonance is triggered, Faraday waves can coexist with the immiscible profile. In both problems, we consider a mean-field theory to describe the condensates, and we assume that the gases are trapped on the surface of an ideal hard spherical shell. In this context, we can track the rise of instability through the familiar math of spherical harmonics angular modes. We can predict the dynamic stability profile by handling Bogoliubov-de Gennes and Floquet theories for stationary, and periodic states, respectively. Next, we are able to check the predictions by observing the full dynamics of the states driven by the Gross-Pitaevskii equation. In this way, by investigating these problems, we provide reliable studies on the stability of several states which can be performed in future experiments with condensates in bubble traps.

**Keywords:** Bose-Einstein Condensate. Condensate Mixtures. Bubble trap. Faraday Waves.

# Resumo

Estudamos propriedades de estabilidade de misturas de condensados de Bose-Einstein confinados na superfície de cascas esféricas. Este trabalho é fortemente motivado pelos avanços recentes no confinamento de gases ultrafrios criados em geometrias de cascas bidimensionais em ambientes de microgravidade a bordo da Estação Espacial Internacional. Nós observamos duas configurações principais. Na primeira, analisamos estados estacionários homogêneos e de vórtices, configurados de maneira que o sistema tenha vorticidade oculta, onde estados de vórtices são tais que as espécies tenham carga de vórtice oposta. Enquanto que na segunda, estudamos estados espacialmente homogêneos e periódicos no tempo, dirigidos por oscilações de Rabi, onde cada espécie pode ser convertida na outra. A frequência de oscilação pode ser sintonizada de maneira a obter ressonância paramétrica. Analisamos em detalhes o papel dos parâmetros de interação e acoplamento de Rabi no perfil de estabilidade resultante das misturas. Uma vez que a instabilidade dirige a dinâmica, ela é capaz de levar as nuvens atômicas a quebrarem em um número bem definido de pedaços imiscíveis. E quando existe ressonância paramétrica, ondas de Faraday podem coexistir com o perfil imiscível. Nos dois problemas, consideramos uma teoria de campo médio para descrever os condensados e assumimos que os gases estão confinados sobre a superfície de uma casca esférica impenetrável ideal. Neste contexto, nós podemos rastrear o surgimento da instabilidade em termos dos modos angulares dos esféricos harmônicos, cuja matemática é bem conhecida. Podemos prever o perfil de estabilidade dinâmica usando teorias de Bogoliubov-de Gennes e Floquet, para estados estacionários e periódicos, respectivamente. Em seguida, somos capazes de checar as previsões observando a dinâmica completa dos estados dirigidos pela equação de Gross-Pitaevskii. Desta maneira, investigando esses dois problemas, promovemos sólidos estudos sobre a estabilidade de diversos estados que podem ser obtidos em futuros experimentos futuros com misturas de condensados em armadilhas de bolha.

**Palavras-Chave:** Condensado de Bose-Einstein. Misturas de condensados. Armadilha de bolha. Ondas de Faraday.

# List of Abbreviations and Acronyms

**ADI** Alternating Direction Implicit

**BdG** Bogoliubov-de Gennes

**BEC** Bose-Einstein Condensate

**BKT** Berezinskii–Kosterlitz–Thouless

**BECCAL** Bose–Einstein Condensate and Cold Atom Laboratory

**CAL** NASA Cold Atom Laboratory

**CN** Crank-Nicolson

**DLR** German Aerospace Center

**FD** Finite differences

**FDPBC** Finite differences with periodic conditions

**GP** Gross-Pitaevskii

**HV** Hidden vorticity

**IFSC** São Carlos Institute of Physics

**IFT** Institute of Theoretical Physics

**IFUSP** Institute of Physics of University of São Paulo

**ISS** International Space Station

**LU** Lower-upper

**NASA** National Aeronautics and Space Administration

**NLSE** Nonlinear Schrödinger equation

**rf** Radio-frequency

**UFSCar** Federal University of São Carlos

**UNILAB** University of International Integration of Afro-Brazilian Lusofonia

**USP** University of São Paulo

**ZARM** Center of Applied Space Technology and Microgravity



**1D** One-dimensional

**2D** Two-dimensional

**3D** Three-dimensional

# List of Symbols

$N$  Number of bosons.

$a_s$  S-wave scattering length.

$d$  Average distance between the bosons.

$i$  Imaginary unit, equivalent to  $\sqrt{-1}$ .

$t$  Time.

$\hbar$  Planck constant divided by  $2\pi$ .

$M$  Atomic mass.

$\nabla$  Gradient.

$\nabla^2$  Laplacian.

$V_{trap}$  Trap potential.

$\dagger$  Transpose complex conjugate.

$*$  Complex Conjugate.

$\hat{\psi}(\mathbf{r})$  Annihilation boson-field operator of a particle at the position  $\mathbf{r}$ .

$\hat{\psi}^\dagger(\mathbf{r})$  Creation boson-field operator of a particle at the position  $\mathbf{r}$ .

$\rho^{(1)}$  One-body density matrix.

$\varphi_j$  Single-particle eigenfunction  $j$  of the matrix  $\rho^{(1)}$ .

$n_j$  Eigenvalue of  $\rho^{(1)}$ , and occupation number of the orbital  $\varphi_j$ .

$\hat{a}_j$  Annihilation operator of a particle at the state  $\varphi_j$ .

$\hat{a}_j^\dagger$  Creation operator of a particle at the state  $\varphi_j$ .

$\delta_{i,j}$  Kronecker delta.

$\psi$  Condensate wave function, or parameter of order.

$V_{int}$  Interaction potential.

$V_{eff}$  Effective potential.

$g$  Interacting parameter.

$g_{11}, g_{22}$  Intra-species interactions between the bosons of the same species 1 and 2, respectively.

$g_{12}, g_{21}$  Inter-species interactions between the bosons of different species 1 and 2.

$\hat{H}_{GP}$  Gross-Pitaevskii Hamiltonian.

$\Lambda$  Overlap function.

$P_j$  Population of species  $j$ .

$\mu$  Chemical potential.

$\eta$  Fluctuation around the stationary state.

$u_k, v_k$  Fluctuation amplitudes.

$\omega$  Excitation frequency.

$M$  Bogoliubov-de Gennes matrix.

$T$  Period in time.

$\hat{H}_0$  Nonperturbed Hamiltonian.

$\hat{H}_{ext}$  Perturbed Hamiltonian.

$\hat{H}_F$  Periodic Hamiltonian.

$\tilde{M}$  Floquet matrix.

$\tilde{\phi}_j$  Periodic function.

$c_j$  Coefficients of a linear combination of functions  $\phi_j$ .

$\epsilon_j$  Floquet quasienergies.

$f(t)$  Periodic function in time.

$\epsilon_k$  Free particle energy corresponding to a momentum  $k$ .

$\tilde{\mathbf{u}}$  Vector of the Floquet amplitudes.

$\alpha$  Real function of time.

$\mathbf{p}$  Periodic function in time.

$\lambda$  Floquet exponent.

Re Real part.

Im Imaginary part.

$V_h$  Spherical harmonic potential.

$\omega_0$  Harmonic trap frequency.

$\Delta$  Detuning parameter of the external field.

$\Omega_Z$  Strength of the external field.  
 $\Delta E$  Energy difference between the Zeeman sublevels achieved.  
 $G$  Earth gravitational acceleration.  
 $V_t$  Total potential including trap and gravitational potential.  
 $V_{bubble}$  Bubble trap potential.  
 $\nabla_{\theta,\phi}^2$  Angular part of the Laplacian.  
 $\nabla_r^2$  Radial part of the Laplacian.  
 $r$  Radius in spherical coordinates.  
 $\theta$  Polar angle in spherical coordinates.  
 $\phi$  Azimuthal angle in spherical coordinates.  
 $f(r)$  Radial function of a Ansatz for ground state in a bubble trap.  
 $\sigma$  Width (or standard deviation) of a radial Gaussian Ansatz.  
 $R_0$  Spherical shell mean radius of a radial Gaussian Ansatz.  
 $\delta R$  Shell thickness of a spherical bubble.  
 $V_{box}$  Spherical box trap potential.  
 $Y_{\ell,m}$  Spherical harmonics with orbital integer number  $\ell$  and azimuthal integer number  $m$ .  
 $j_\ell$  Spherical Bessel function of order  $\ell$ .  
 $n_\ell$  Spherical Neumann function of order  $\ell$ .  
 $g_{2D}$  Interaction parameter in two-dimensional reduction.  
 $\gamma_{jk}$  Interaction parameter.  
 $\mathbf{L}$  Angular momentum operator.  
 $f_j(\theta)$  Azimuthal-symmetric ansatz for wave function of species  $j$ .  
 $\mu_j$  Chemical potential corresponding to the species  $j$ .  
 $E$  Total energy.  
 $E_{var}$  Variational energy.  
 $E_{asy}$  Variational energy in the asymptotic limit.  
 $\beta$  Variational parameter.  
 $s_j$  Vortex charge of species  $j$ .  
 $\Omega$  Rabi frequency.  
 $\sigma_y$  Pauli matrix for  $y$ -coordinate.

**R** Evolution operator.

**1** Identity operator.

$\omega_\ell$  Excitation frequency corresponding to the angular orbital mode  $\ell$ .

$\epsilon_\ell$  Free energy corresponding to a excitation of the angular orbital mode  $\ell$ .

$\eta_{j,\ell}$  Fluctuation function for the species  $j$  and angular orbital mode  $\ell$ .

$\psi_\pm$  Dressed states.

$\zeta_{j,\ell}$  Fluctuation function for the species  $j$  and angular orbital mode  $\ell$ .

$\lambda_\ell$  Floquet exponent corresponding to the angular orbital mode  $\ell$ .

**F** Vector of the Floquet amplitudes.

log Natural logarithm.

$\Delta(t)$  Perturbation function in time.

$\xi$  Difference between the intra- and inter-species interactions.

$\delta\mu$  Phase correction.

$S$  Solid angle.

$c_{\ell,m}$  Spherical harmonics Coupling coefficients.

# List of Figures

3.1	Available experimental setups to handle bubble shaped cold gases. . . . .	30
3.2	Dressed potential and matter-wave shell at microgravity environment. From [58]. . .	33
3.3	Bare and dressed potential under effect of the gravity. From [14]. . . . .	33
3.4	Dressed potential and matter-wave shell at microgravity environment. From [16]. . .	34
3.5	Matter-wave bubble. From [16]. . . . .	34
4.1	Modes diagram for homogeneous ( $s_1 = s_2 = 0$ ) solutions depending on the interactions $\gamma_{12}$ versus $\gamma_{11} = \gamma_{22}$ , following the Eq. (4.15). Stable regions stand for parameters for which no mode has imaginary part higher than zero. The lines presents when the unstable modes $\ell = 1, 2$ , and 3 emerge. From [18]. . . . .	45
4.2	Stability diagram for homogeneous solutions as a function of intra- and inters-species $\gamma_{11}$ and $\gamma_{12}$ , respectively, see Eq. (4.15). Black spaces stand for stable regions. Violet, orange and yellow places refer to unstable regions where the dominant mode is $\ell = 1, 2$ , and 3, respectively. From [18]. . . . .	45
4.3	Imaginary spectrum of modes $\ell = 1, 2, 3$ , and 4 as functions of the inter-species interaction $\gamma_{12}$ , based on analytical unstable frequencies, see Eq.(4.14). The intra-species interactions are fixed in $\gamma_{11} = \gamma_{22} = 10$ . . . . .	46
4.4	Pattern of $ f_j(\theta) ^2$ , $j = 1, 2$ when the system goes from the miscibility to the immiscibility, for fixed $\gamma_{11} = 10$ when the inter-species interaction increases. (a) $\gamma_{12} = 10$ and $\Lambda = 1$ . (b) $\gamma_{12} = 20$ and $\Lambda = 0.17$ . (c) $\gamma_{12} = 100$ and $\Lambda = 0.00$ . Solid-black line refers to the species 1, and red-dashed line to the species 2. From the author. . . . .	47
4.5	Density wave patterns $ \psi_j(\theta, \phi) ^2$ , $j = 1, 2$ , with (a), (b), and (c) following the parameters of (a), (b) and (c) from Fig. 4.4 for species 1. And (d), (e), and (f) corresponding to the species 2. Low density regions are darker and higher density regions are lighter. Note the pole $\theta = 0$ is localized on the top of the spheres, and $\theta = \pi$ at the bottom. From the author. . . . .	47
4.6	Variational quantities in terms of the interaction parameter $\gamma$ . (a) Minimization variational parameter $\beta$ where the solid-red line is the variational parameter and the blue-dashed line is the asymptotic approximation. (b) Comparison between variational and exact-numerical results for the energies and chemical potentials. Solid-red line with circles and the blue-solid line are the numerical energy and chemical potential, respectively. The dashed-red and dashed-blue lines are the corresponding quantities by variational approximation. From [18]. . . . .	49
4.7	Numerical and Variational results (with $\beta$ indicated) for $ f ^2$ . (a) The quantity is shown as a function of $\theta$ . (b) Is presented the maximum values ( $\theta = \pi/2$ ) as function of $\gamma$ . From [18]. . . . .	50
4.8	Stability diagram for hidden vorticity solutions ( $s_1 = -s_2 = 1$ ) displayed as a function of the interactions parameters $\gamma_{12}$ versus $\gamma_{11} = \gamma_{22}$ , obtained by the diagonalization of Eq. (4.27). The index 's' refers to the stable region and the numbers present the modes $m = 0, \dots, 7$ , which are dominant in that unstable regions. From the author.	52

4.9	Maximum imaginary BdG spectrum $\text{Im}(\omega)$ returned by diagonalization of (4.27) as a function of the interaction parameters, driven by the excitation modes $m = 0, \dots, 5$ . (a) Spectrum when $\gamma_{11} = 10$ is fixed. (b) Spectrum when $\gamma_{12} = 0$ is fixed. From [18].	52
4.10	Ansatz for both species at the time $t = 0$ when we have the parameters $\gamma_{11} = 10$ and $\gamma_{12} = 12$ , and vortex charges $s_1 = -s_2 = 1$ , see Eq. (4.4). Note that each species has a vortex-antivortex pair. At this perspective, we only can see the bottom vortices, but also have the top ones. Unfortunately, we can not see all vortex in only one 2D picture. From the author.	53
4.11	Properties dynamics of the unstable case where parameters are $\gamma_{11} = 10$ and $\gamma_{12} = 12$ . (a) Average angular momentum $\langle L_z \rangle_j$ , see Eq.(4.8). (b) Overlap $\Lambda(t)$ evolution in time, see Eq.(2.24). From [18].	53
4.12	Densities of species 1, 2 and the sum them (from left to right) at the time $t = 55$ when $\gamma_{11} = 10$ and $\gamma_{12} = 12$ , same case of Fig. 4.11. Row (a) presents the spheres with z-direction pointing outwards the page. And row (b) presents the spheres with y-direction pointing inwards the page. From [18].	54
5.1	(Color online) Density oscillating period $T$ as a function of the absolute difference of the interaction parameters $ g - g_{12} $ . The results stand for different Rabi couplings $\Omega$ , as indicated. From [19]	61
5.2	(Color online) Time-evolution of the atom-number ratio (normalized densities), $N_j(t)/N \equiv 4\pi n_j = 4\pi  \psi_j(t) ^2$ , with initial condition $n_j(0) = 1/2$ , for constant Rabi couplings $\Omega = 0.01, 0.1$ , and $0.2$ , where the absolute difference between the interaction parameters are given by $ g - g_{12}  = 0$ (a) and $ g - g_{12}  = 10$ (b). In both panels, the black dashed lines refer to species 1 and the red solid lines to species 2, where the horizontal blue dotted line stands for $\Omega = 0$ .	62
5.3	(Color on-line) BdG stability diagrams, as given by Eq. (5.20). Black places are stable regions ( $\text{Im}(\omega_{\ell,\pm}) = 0$ ) and the colors provide the dominant unstable angular modes ( $\text{Im}(\omega_{\ell,\pm}) \neq 0$ ). Violet places stand for the unstable angular mode $\ell = 1$ and orange for $\ell = 2$ . (a) Rabi coupling constant $\Omega = 0.1$ . (b) $\Omega = 0.9$ . From [19].	64
5.4	(Color on-line) BdG stability diagrams regarding the extreme regimes. Black places are stable regions ( $\text{Im}(\omega_{\ell,\pm}) = 0$ ) and the colors provide the dominant unstable angular modes ( $\text{Im}(\omega_{\ell,\pm}) \neq 0$ ). Violet places stand for the unstable angular mode $\ell = 1$ and orange for $\ell = 2$ . (a) Zero Rabi coupling regime, see Eq. (5.21). (b) Strong Rabi coupling regime, see Eqs. (5.31a) and (5.31b).	66
5.5	(Color on-line) Floquet stability diagrams based on $\text{Max}[\text{Re}(\lambda_\ell)]$ , see Eq. (5.34). Black places are stable regions ( $\text{Max}[\text{Re}(\lambda_\ell)] \leq 0$ ) and the colors provide the dominant angular unstable modes ( $\text{Max}[\text{Re}(\lambda_\ell)] > 0$ ), violet places stand for the unstable angular mode $\ell = 1$ , orange for $\ell = 2$ and yellow for $\ell = 3$ . (a) Rabi coupling constant $\Omega = 0.1$ . (b) $\Omega = 0.9$ . From [19].	68
5.6	(Color on-line) Floquet spectrum $\text{Max}[\text{Re}(\lambda_\ell)]$ as a function of inter-species interaction, see Eq. (5.34). Violet solid lines stand for the unstable angular mode $\ell = 1$ , and red dashed lines refer to $\ell = 2$ . Intra-species interaction and Rabi coupling constant are given by $(g, \Omega) = (20, 0.1)$ and $(40, 0.9)$ . Which are displayed in panels (a) and (b), respectively. Inset panels show the lower peaks in the main panel. From [19].	68

5.7	(Color online) Resonance couplings and unstable Floquet spectrum as functions of the Rabi coupling $\Omega$ . The vertical dashed lines stand for the three predicted resonance critical couplings (5.51a), (5.51b) and (5.51c) for $g = 1$ , while the peaks are provided by the unstable Floquet spectrum ( $\text{Max}[\text{Re}(\lambda_\ell)]$ ), see Eq. (5.34). Only the unstable angular mode $\ell = 1$ is actually important for the chosen parameters. (a) Cases where the inter-species interactions are $g_{12} = 1.1, 1.3, \text{ and } 1.5$ , on black/bottom, red/middle and blue/top set of peaks, respectively. (b) Cases where $g_{12} = 3.0, 5.0, \text{ and } 8.0$ , on black/bottom, red/middle and blue/top peaks, respectively. From [19]. . . . .	71
5.8	Overlap $\Lambda(t)$ (see Eq. (2.24)) between the species for cases 1 to 4, depicted in $\Lambda_1$ to $\Lambda_4$ , where the corresponding values are calculated for the set of parameters intra- and inter-species interaction, and Rabi coupling constant $(g, g_{12}, \Omega) = (1, 8, 0.50), (40, -10, 0.94), (1, 10, 0.10), \text{ and } (1, 25, 0.99)$ , respectively. Cases 1 and 2 are presented in the main panel on violet and orange solid lines, respectively. Cases 3 and 4 are displayed in the inset panel on the red-solid and black-dotted lines, respectively. From [19]. . . . .	72
5.9	(Color on-line) Population dynamics $P_j(t)$ (see Eq. (2.25)) of the species for the cases 1 and 2, with intra- and inter-species, and Rabi coupling constant given by $(g, g_{12}, \Omega) = (1, 8, 0.50), (40, -10, 0.94)$ , respectively. The cases are displayed in panels (a) and (b), respectively. Solid lines stand for the full GP calculation of the system given by Eqs. (5.3a) and (5.3b), taking into account spatial-time-dependent wave functions and the dotted ones are homogeneous only time-dependent solutions (5.15). Black lines are species 1 and the red ones are species 2. . . . .	73
5.10	(Color on-line) Population $P_j(t)$ and Overlap $\Lambda(t)$ dynamics, see Eqs. (2.25) and (2.24), respectively. Black and red solid lines are populations of species 1 and 2, respectively. The overlap between the species is displayed in the dashed blue line. (a) Case 2, with intra- and inter-species interaction, and Rabi coupling constant given by $(g, g_{12}, \Omega) = (40, -10, 0.94)$ . (b) Case 5, with parameters $(-10, 20, 0.90)$ . . . . .	75
5.11	(Color online) Density dynamics $ \psi_j ^2$ of the case 1 with intra- and inter-species interaction, and Rabi coupling constant given by given by $(g, g_{12}, \Omega) = (1, 8, 0.50)$ . Species one is displayed on the left, and species two on the right. Panels (a)-(e) refer to time $t = 0, 15, 35, 42, \text{ and } 60$ , respectively. Species 1 is displayed on the left, and species 2 on the right. . . . .	76
5.12	(Color online) Density dynamics $ \psi_j ^2$ of the cases 2, and 5 with intra- and inter-species interaction, and Rabi coupling constant given by $(g, g_{12}, \Omega) = (40, -10, 0.94), \text{ and } (-10, 20, 0.90)$ , respectively. Species one is displayed on the left, and species two on the right. The first row displays case 2 on panels (a)-(c) for time $t = 0, 20, \text{ and } 30$ , respectively. The second row presents the case 5 on the panels (d)-(f) for $t = 0, 10, \text{ and } 15$ , respectively. . . . .	76
5.13	(Color online) Coupling parameters $ c_{\ell,m}(t) ^2$ of species 1 as functions of time $t$ [Eq. (5.52)]. Cases 1, 2, and 5 are depicted in (a), (b), and (c), with intra- and inter-species interaction, and Rabi coupling constant given by $(g, g_{12}, \Omega) = (1, 8, 0.50), (40, -10, 0.94), \text{ and } (-10, 20, 0.90)$ , respectively. The insets in panels (a) and (b) stand for the lower lines of the main panels. . . . .	77



5.14	(Color on-line) Maximum unstable spectrum for each unstable angular mode $\ell$ as function of the inter-species interaction $g_{12}$ and Rabi coupling constant $\Omega$ , with fixed intra-species interaction $g = 1$ . BdG unstable spectrum is given by $\text{Max}[\text{Im}(\omega_{\ell,\pm})]$ and Floquet unstable spectrum is provided by $\text{Max}[\text{Re}(\lambda_\ell)]$ . The numbers stand for the corresponding angular mode $\ell$ . dashed lines refer to BdG spectrum, see Eq. (5.20). Empty squares present the BdG regime $\Omega = 0$ , see Eq. (5.21). Violet dots show the strong BdG regime $\Omega \rightarrow \infty$ , see Eqs. (5.31a) and (5.31b). Red solid lines display the Floquet spectrum, see Eq. (5.34). (a) $\Omega = 0.01$ . (b) $\Omega = 0.50$ . (c) $\Omega = 0.99$ . . . . .	79
5.15	(Color on-line) Floquet maximum spectrum ( $\text{Max}[\text{Re}(\lambda_\ell)]$ ) of each unstable angular mode $\ell$ as a functions of the Rabi coupling $\Omega$ , see Eq. (5.34). Cases $(g, g_{12}) = (1, 15)$ and $(40, -10)$ are displayed on red dashed lines and black solid lines, respectively. The numbers stand for the corresponding unstable angular mode $\ell$ . . . . .	80
5.16	(Color on-line) Stability diagram as a function of inter-species interaction and Rabi coupling, with fixed intra-species interaction $g = 1$ . Black places are stable regions and the colors provide the dominant unstable angular modes $\ell$ . Violet places stand for $\ell = 1$ and the orange ones for $\ell = 2$ . (a) BdG, see Eq. (5.20). (b) Floquet, see Eq. (5.37). . . . .	80

\*

# List of Tables

5.1 Stability status given by the three methods, given the parameter of intra- and inter-species interaction, and Rabi coupling constant  $\Omega, g, g_{12}$ . Unstable cases are displayed with the dominant unstable mode  $\ell$ . The reference figures where the results can be checked are set in parentheses. . . . . 80

\*

# Contents

<b>1</b>	<b>Introduction</b>	<b>17</b>
1.1	Thesis outline . . . . .	19
<b>2</b>	<b>Weakly Interacting Bosons</b>	<b>21</b>
2.1	Gross-Pitaevskii equation . . . . .	23
2.1.1	Binary condensate mixtures . . . . .	24
2.2	Bogoliubov-de Gennes theory . . . . .	25
2.3	Floquet theory . . . . .	26
<b>3</b>	<b>Condensates on the spherical bubble</b>	<b>29</b>
3.1	Ultracold gas trapped on the bubble . . . . .	31
3.2	Dimensional reduction . . . . .	35
3.3	Validity of a two-dimensional approximation . . . . .	37
3.4	Dimensionless model . . . . .	39
<b>4</b>	<b>BEC Mixtures Stability</b>	<b>41</b>
4.1	Model . . . . .	42
4.2	Homogeneous system . . . . .	44
4.2.1	Stability . . . . .	44
4.3	Hidden-vorticity system . . . . .	48
4.3.1	Variational approximation . . . . .	48
4.3.2	Stability . . . . .	50
4.3.3	Dynamics . . . . .	52
4.4	Conclusions . . . . .	54
<b>5</b>	<b>Faraday Waves on Mixtures Driven by Rabi Coupling</b>	<b>56</b>
5.1	Mixtures driven by Rabi oscillations . . . . .	58
5.2	Model . . . . .	59
5.2.1	Non-interacting system . . . . .	59
5.2.2	Interacting system . . . . .	60
5.3	Stability of stationary solutions . . . . .	62
5.3.1	Zero coupling . . . . .	64
5.3.2	Strong coupling . . . . .	64
5.4	Stability of periodic solutions . . . . .	66
5.4.1	Resonance conditions . . . . .	68
5.5	Dynamics . . . . .	72
5.6	Methods comparison . . . . .	78
5.7	Conclusions . . . . .	81
<b>6</b>	<b>Conclusions</b>	<b>82</b>
6.1	Perspectives . . . . .	83

<b>Bibliography</b>	<b>85</b>
<b>A Methods</b>	<b>93</b>
A.1 Split-Step method . . . . .	93
A.2 Two-dimensional spherical shell: Spectral and finite differences method . . . . .	95
A.3 Polar-direction finite differences . . . . .	95
A.4 Polar-direction Bogoliubov de-Gennes method . . . . .	98
A.5 Spatial-homogeneous Time-periodic solutions by Runge-Kutta method . . . . .	99
A.6 Floquet method for spatial-Homogeneous time-periodic solutions . . . . .	100

# Chapter 1

## Introduction

A system of bosons was first described with an appropriate statistics in 1924 [1], originally aiming to find the black-body radiation spectrum without elements from the classical physics. Bose introduced an innovative statistics where the particles are indistinguishable and can occupy discrete states, and these states can be occupied by more than one particle. Einstein extended these ideas to an ideal atomic gas (massive particles), where he observed that at very low temperatures this distribution over the quantized energy levels gives rise to a large occupation of the lowest quantum state [2, 3], today called *Bose-Einstein condensation* phenomenon. Seven decades later, this regime was experimentally observed with dilute weakly interacting gases of alkali atoms of  $^{87}\text{Rb}$  [4], which was followed by the observation with  $^{23}\text{Na}$  [5], and  $^7\text{Li}$  [6]. The success of these experiments engaged many research groups to study the properties of ultracold atomic gases [7, 8].

The properties of a Bose-Einstein condensate (BEC) of a dilute gas can be very well described by the mean-field model, where the system is driven by a nonlinear Schrödinger equation (NLSE) known as Gross-Pitaevskii (GP) equation [8]. The GP framework allows several studies, and we perform some of them in this project, focusing on the analysis of the dynamics of condensates.

A numerically expensive way to find out the stability profile of an initial state is to perform the full dynamics simulation of these states for a very long time, and observe whether the initial state changes. It is not a feasible task when we want to establish the stability profile for a large range of parameters. Therefore, we must resort to a theoretical tool to predict stability profiles. This tool only requires the initial state information and system parameters, without the need for a long time simulation. The main tools for such endeavor are based on the solutions of the linearized GP equations, from where we get the eigenvalues of the small amplitude oscillations. In this way, we can figure out how the fluctuations increase with time. For stationary states, this approach is called Bogoliubov-de Gennes (BdG) theory [7–9], and when we have time-periodic states, we call Floquet theory [10–12]. Therefore, by handling GP equations and the linearized methods, we have powerful tools to predict stability profile of Bose-Einstein condensates.

About two decades ago, some techniques were introduced aiming to confine ultracold gases in two-dimensional ellipsoidal closed shell [13, 14]. However, the gravitational sag always was an inherent challenge for Earth-based laboratories. In this way, the wondered kind of system once proposed could be feasible just recently by the breakthrough experiments with ultracold gases in microgravity environment of space-based laboratories [15–17]. Since then, all community of cold atoms physics is deeply interested in the physics of cold atoms trapped on two-dimensional bubbles. Therefore, our research group is strongly motivated to take part in the new achievements with condensates in these geometries.

In this Thesis, we focus on stability properties of Bose-Einstein condensate mixtures trapped on the surface of an ideal spherical shell. First, we consider stationary systems, for which we can handle a BdG analysis to predict how long both spatial-homogeneous and vortex-antivortex states are dynamically stable. Second, we investigate spatially-homogeneous states with populations periodically driven by Rabi coupling, where parametric resonance can be achieved and give rise to Faraday waves. To our knowledge, our findings are the first investigations on stability behavior of mixtures in the context of condensates confined on the same surface of bubbles.

In the first work presented here, we study stability of binary BEC mixtures initially arranged as miscible stationary states. We consider homogeneous gases, or gases designed in vortex-states where each species has a vortex-charged with opposite sign to each other. Here, the last case is called hidden-vorticity (HV) set up. An interacting gas mixture has intra- (same species) and inter-species (different species) interactions. The ratio between them affects the gases' miscibility properties, and therefore, it influences the stability of stationary solutions. For both kind of configurations, we analyze the elementary excitation spectrum around the states by using the BdG technique. We find the region of stability in terms of the interaction parameters and the number of particles of each species, and we are also able to track which angular modes are actually driving the dynamics. Since an angular mode arise, it can drive the system to a broken picture, where the species become immiscible clouds. The number of clouds is related to the angular mode that governs the dynamics. Our main results are displayed in the paper published in the **Physical Review A** journal [18].

In the second work, we study time-periodic spatially homogeneous states driven by Rabi oscillations, where each species can convert into the other. In this kind of system, we have the remarkable feature that it is possible effectively handle time-dependent interaction energy with no need of periodic modulations in the scattering length or the trap frequencies. The population oscillations are sufficient to trigger parametric resonance. Then, once the Rabi coupling is tuned to achieve the natural excitation frequencies, spatial patterns emerge, and Faraday waves arise in the sys-

tem. Similar to the first work, here unstable modes can take over the dynamics and lead the initial state to a break into a well defined number of pieces corresponding to the angular dominant mode. With the Floquet method, we can predict the stability profile of a system given the interaction parameters and the Rabi coupling by performing a linearized method to get the time-dependent excitation modes behavior. This powerful method enables us to get some insight about the dynamics of the system just with only one complete period of simulation. Once an angular mode breaks the system into pieces, Faraday waves can coexist with the immiscible profile. Our results are available in a preprint version at arXiv [19].

## 1.1 Thesis outline

This text is organized as follows. In chapter 2, we introduce the mean-field theory, Gross-Pitaveskii equation and we describe the stability methods based on Bogoliubov-de Gennes and Floquet theories. It is followed by an introduction to the bubble trap in chapter 3, where we also handle a dimensionally-reduced model, and we discuss its validity. We present the first original work in chapter 4, where we study the stability of stationary states in homogeneous and vortex-charged solutions. In chapter 5, we present the second original work, where we study the stability of spatial-homogeneous time-periodic solutions. We finish the main text with a conclusion in chapter 6, where we also present our perspectives for the next research years. In addition, in appendix A, we present the main numerical techniques used to solve the problems.

The contents of this thesis are displayed in the papers:

- Stability of a Bose-condensed mixture on a bubble trap. Alex Andriati, **Leonardo Brito**, Lauro Tomio, and Arnaldo Gammal. Phys. Rev. A **104**, 033318 (2021) [18].
- Faraday waves on a bubble Bose-Einstein condensed binary mixture. **Leonardo Brito**, Lauro Tomio, and Arnaldo Gammal [19].

During this period, the author also worked on the projects below, but we do not present them in this text for better focus on a subject.

- Coherent control of nonlinear mode transitions in Bose-Einstein condensates. **L. B. da Silva**, and E. F. de Lima. J. Phys. B: At. Mol. Opt. Phys. **53** 125302 (2020) [20].

- Breakup of rotating asymmetric quartic-quadratic trapped condensates. **Leonardo Brito**, Alex Andriati, Lauro Tomio, and Arnaldo Gammal. *Phys. Rev. A* **102**, 063330 (2020) [21].



# Chapter 2

## Weakly Interacting Bosons

A realistic approach for the gas of  $N$  bosons can be to consider an interacting dilute gas in a potential trap at low temperatures. This is the scenario for an experiment in a laboratory, where a trap potential is required to confine the bosons, and that potential leads the system to an inhomogeneous pattern. In a first approximation, we can take into account a weakly interaction between the pairs of bosons, which is a good model to describe cold alkali gases, which are largely used in actual experiments.

The gas of bosons is called *dilute* if the range of interatomic interactions is much smaller than the average distance  $d$  between the bosons. At low temperatures, and therefore, at low energies, an interaction parameter can be the s-wave scattering length  $a_s$ , and the gas is weakly interacting if we have [7, 8]

$$|a_s| \ll d, \quad (2.1)$$

and since that condition is satisfied we can neglect three-body interactions and more. Then, we are able to write the Schrödinger equation for bosons with mass  $M$  in a potential trap  $V_{trap}$  with only two-body interactions driven by a potential  $V_{int}$  as [8]

$$i\hbar \frac{\partial}{\partial t} \hat{\psi}(\mathbf{r}, t) = \left[ -\frac{\hbar^2}{2M} \nabla^2 + V_{trap}(\mathbf{r}, t) + \int d\mathbf{r}' \hat{\psi}^\dagger(\mathbf{r}', t) V_{int}(\mathbf{r}' - \mathbf{r}) \hat{\psi}(\mathbf{r}', t) \right] \hat{\psi}(\mathbf{r}, t), \quad (2.2)$$

where  $\hbar$  is the Planck  $h$  constant divided by  $2\pi$ , and  $i = \sqrt{-1}$  is the imaginary unit. The system is described by boson-field operators  $\hat{\psi}^\dagger(\mathbf{r})$ , and  $\hat{\psi}(\mathbf{r})$  which, respectively, create and annihilate a boson at position  $\mathbf{r}$ . They obey the commutation relations

$$[\hat{\psi}(\mathbf{r}), \hat{\psi}^\dagger(\mathbf{r}')] = \delta(\mathbf{r} - \mathbf{r}'), [\hat{\psi}(\mathbf{r}), \hat{\psi}(\mathbf{r}')] = [\hat{\psi}^\dagger(\mathbf{r}), \hat{\psi}^\dagger(\mathbf{r}')] = 0. \quad (2.3)$$

We can introduce the one-body density matrix  $\rho^{(1)}$ , that can be written in the position-space as [8]

$$\rho^{(1)}(\mathbf{r}, \mathbf{r}') = \left\langle \hat{\psi}^\dagger(\mathbf{r}') \hat{\psi}(\mathbf{r}) \right\rangle, \quad (2.4)$$

it can express an amplitude for removing a boson at  $\mathbf{r}$  and set it at  $\mathbf{r}'$ . The average  $\langle \dots \rangle$  meaning depends on the physical situation. If we handle a system in a pure state  $|\psi\rangle$ , represented by a many-body wave function  $\psi_n(\mathbf{r}_1, \dots, \mathbf{r}_N)$ , the average is

the trace of all particles except one [7], but if we deal with a statistical mixture, we suppose to average that trace over the probabilities of a system occupying different many-body states  $\psi_n$  [8]. Here we focus on the first case where we can describe a pure condensate. The diagonal of  $\rho^{(1)}(\mathbf{r}, \mathbf{r}')$  is the particle density  $n$

$$n(\mathbf{r}) = \rho^{(1)}(\mathbf{r}, \mathbf{r}) , \quad (2.5)$$

then the one-body density matrix is normalized by

$$\int d\mathbf{r} \rho^{(1)}(\mathbf{r}, \mathbf{r}) = N , \quad (2.6)$$

where  $N$  is the number of bosons. The matrix  $\rho^{(1)}(\mathbf{r}, \mathbf{r}')$  is Hermitian and positive definite. Therefore, it has real and positive eigenvalues [7], and we can write it in a diagonalized form, in terms of its eigenvalues  $n_j$  and the corresponding eigenfunctions  $\varphi_j$

$$\rho^{(1)}(\mathbf{r}, \mathbf{r}') = \sum_j n_j \varphi_j^*(\mathbf{r}') \varphi_j(\mathbf{r}) . \quad (2.7)$$

We remark that  $\{\varphi_j\}$  is a set of single-particle ortho-normalized wave functions, and  $N = \sum_j n_j$ , with  $j = 0, 1, 2, \dots$ . *Bose-Einstein condensation* can be understood as the situation where one of the single-particle states, take  $\varphi_j$ , is macroscopically occupied, i.e, the corresponding eigenvalue is of order of the total number of particles,  $n_j \approx N$ , and the other eigenvalues are around zero [22]. Usually, we mean the ground-state  $\varphi_0$  with  $n_0 = N_0 \approx N$  when we refer to a Bose-Einstein condensate (BEC), since in practice can be very difficult to build a condensate in an excited state. The functions  $\{\varphi_j\}$  can also be used to write the boson field  $\hat{\psi}$

$$\hat{\psi}(\mathbf{r}) = \sum_j \varphi_j(\mathbf{r}) \hat{a}_j , \quad (2.8)$$

with  $\hat{a}_j$  and  $\hat{a}_j^\dagger$ , which, respectively, annihilate or create a particle in the single-state function  $\varphi_j$ . These operators satisfy the commutation relations

$$[\hat{a}_i, \hat{a}_j^\dagger] = \delta_{ij} , [\hat{a}_i, \hat{a}_j] = [\hat{a}_i^\dagger, \hat{a}_j^\dagger] = 0 , \quad (2.9)$$

where  $\delta_{ij}$  is the usual Kronecker delta. It is convenient to write the field operator as a sum where the lower state is explicit

$$\hat{\psi}(\mathbf{r}) = \varphi_0(\mathbf{r}) \hat{a}_0 + \sum_{j>0} \varphi_j(\mathbf{r}) \hat{a}_j . \quad (2.10)$$

Here, we can begin by assuming that the lower state is macroscopically occupied, indicating that we are dealing with a condensed state. Consequently, it becomes

valuable to introduce the *Bogoliubov prescription* [23], which states that the first term of Eq. (2.10) is a c-number, or a classical field. We can write

$$\hat{a}_0 \hat{a}_0^\dagger - \hat{a}_0^\dagger \hat{a}_0 = 1. \quad (2.11)$$

The occupation number at the state  $j = 0$  is  $N_0 = \langle \hat{a}_0^\dagger \hat{a}_0 \rangle$ , then the operators are of order  $\sqrt{N_0}$ , which are much larger than 1. Therefore, we can state

$$\hat{a}_0 \hat{a}_0^\dagger \approx \hat{a}_0^\dagger \hat{a}_0, \quad (2.12)$$

which means that we can ignore the commutation relations for this state, and consider  $\hat{a}_0 \approx \hat{a}_0^\dagger \approx \sqrt{N_0}$ , then we can define the classical field  $\psi_0 = \sqrt{N_0} \varphi_0$  and the non-condensed components by  $\delta\hat{\psi}$  [9, 23]

$$\hat{\psi}(\mathbf{r}) = \psi_0(\mathbf{r}) + \delta\hat{\psi}(\mathbf{r}). \quad (2.13)$$

## 2.1 Gross-Pitaevskii equation

At very low temperatures, where the particles are mainly condensed in the ground state, the field operator can be well described by the classical field, and we can neglect  $\delta\hat{\psi}$  and set the field as

$$\hat{\psi}(\mathbf{r}) \approx \psi(\mathbf{r}), \quad (2.14)$$

where we omit the index  $j = 0$  of the lower state, since we are assuming the system consisting of all bosons in the ground state. The approximated field  $\psi(\mathbf{r})$  is called *wave function of the condensate*, or sometimes the *order parameter*. The total number of particles  $N$  is assumed to be occupying the ground state, in such a way that the normalization condition is

$$\int d\mathbf{r} |\psi(\mathbf{r})|^2 = N, \quad (2.15)$$

which eventually can be set as 1, if we incorporate the number of atoms in the definition of interaction parameters. Then, in the classical approach, the Schrödinger equation (2.2) becomes

$$i\hbar \frac{\partial}{\partial t} \psi(\mathbf{r}, t) = \left[ -\frac{\hbar^2}{2M} \nabla^2 + V_{trap}(\mathbf{r}, t) + \int d\mathbf{r}' \psi^*(\mathbf{r}', t) V_{int}(\mathbf{r}' - \mathbf{r}) \psi(\mathbf{r}', t) \right] \psi(\mathbf{r}, t). \quad (2.16)$$

We are supposing the system at low temperatures, with all particles in the ground-state. Moreover, we can consider the regime of low-energy scattering in the interactions. Then, the potential goes to zero out of a small range, i.e, we can set  $V_{int}(\mathbf{r}' - \mathbf{r}) \approx V_{int}(\mathbf{r}')$ , and therefore, this is the case of a soft interaction potential, called effective potential  $V_{eff}$ . Within that region, the wave function is weakly affected, which means  $\psi(\mathbf{r}') \approx \psi(\mathbf{r})$ , and we can use the *Born approximation* [24], i.e,

we can perform the interaction term as

$$\begin{aligned} \int d\mathbf{r}' \psi^*(\mathbf{r}', t) V_{int}(\mathbf{r}' - \mathbf{r}) \psi(\mathbf{r}', t) &\approx \int d\mathbf{r}' \psi^*(\mathbf{r}, t) V_{eff}(\mathbf{r}') \psi(\mathbf{r}, t) \\ &\approx |\psi(\mathbf{r}, t)|^2 \int d\mathbf{r}' V_{eff}(\mathbf{r}') , \end{aligned} \quad (2.17)$$

and at low energies, the scattering amplitude can be written in terms of a s-wave scattering length  $a_s$  as [8]

$$g = \frac{4\pi\hbar^2 a_s}{M} = \int d\mathbf{r}' V_{eff}(\mathbf{r}') , \quad (2.18)$$

in which, we define  $g$  the interaction parameter, which can contain the normalization condition in an alternative approach performed along this thesis. Inserting these approximations into Eq. (2.16), we get

$$i\hbar \frac{\partial}{\partial t} \psi(\mathbf{r}, t) = \left[ -\frac{\hbar^2}{2M} \nabla^2 + V_{trap}(\mathbf{r}, t) + g|\psi(\mathbf{r}, t)|^2 \right] \psi(\mathbf{r}, t) . \quad (2.19)$$

This is a mean-field equation that describes the whole condensate by only one orbital, and it is called *Gross-Pitaevskii* (GP) equation [7, 8]. We also can write it as

$$i\hbar \frac{\partial}{\partial t} \psi(\mathbf{r}, t) = \hat{\mathbf{H}}_{GP}[\psi] \psi(\mathbf{r}, t) , \quad (2.20)$$

with the operator

$$\hat{\mathbf{H}}_{GP}[\psi] = -\frac{\hbar^2}{2M} \nabla^2 + V_{trap}(\mathbf{r}, t) + g|\psi(\mathbf{r}, t)|^2 . \quad (2.21)$$

### 2.1.1 Binary condensate mixtures

We can generalize the GP equation for a mixture of two species [7, 8], where we do not take into account that, in practice, different hyperfine states of Bose gas in a mixture require different traps to confine them. In our first approximation, we consider the same trap for both species, since we are supposing spinless particles, and we analyze the miscibility and stability properties driven by the interaction between these gases. Therefore, we extend the GP equation (2.19) to a coupled two-component system

$$i\hbar \frac{\partial \psi_1}{\partial t} = -\frac{\hbar^2}{2M_1} \nabla^2 \psi_1 + V_{trap} \psi_1 + g_{11} |\psi_1|^2 \psi_1 + g_{12} |\psi_2|^2 \psi_1 , \quad (2.22a)$$

$$i\hbar \frac{\partial \psi_2}{\partial t} = -\frac{\hbar^2}{2M_2} \nabla^2 \psi_2 + V_{trap} \psi_2 + g_{22} |\psi_2|^2 \psi_2 + g_{21} |\psi_1|^2 \psi_2 , \quad (2.22b)$$

where the interaction parameters take into account the number of atoms  $N_{j,k}$  of each species by  $g_{jj} = 4\pi\hbar^2 a_{jj} N_j / M_j$  and  $g_{jk} = 2\pi\hbar^2 a_{jk} N_k / M_r$ , with the reduced mass

$M_r$  is given by  $1/M_r = 1/M_j + 1/M_k$  [8], and  $j, k = 1, 2$  with  $k \neq j$ . The scattering lengths  $a_{jj}$  and  $a_{jk}$  correspond to same (intra) and different (inter) species interactions, respectively. For simplicity, we are omitting the  $(\mathbf{r}, t)$  dependency. And at this time, the normalization conditions can be set as

$$\int d\mathbf{r} |\psi_j(\mathbf{r}, t)|^2 = 1, \quad (2.23)$$

where  $j = 1, 2$ . An auxiliary property used to investigate how the species coexist in the same region is the overlap  $\Lambda$ , which follows the expression [25]

$$\Lambda(t) = \frac{\left[ \int d\mathbf{r} |\psi_1(\mathbf{r}, t)|^2 |\psi_2(\mathbf{r}, t)|^2 \right]^2}{\left[ \int d\mathbf{r} |\psi_1(\mathbf{r}, t)|^4 \right] \left[ \int d\mathbf{r} |\psi_2(\mathbf{r}, t)|^4 \right]}, \quad (2.24)$$

where  $0 \leq \Lambda \leq 1$ . When  $\Lambda = 1$  the coupled system can be considered miscible, or mixed. And for  $\Lambda < 1$  the system is considered immiscible, or demixed. Miscibility is a useful property to investigate stability, since for a particular class of problems, that property is straightly related with the dynamic stability.

If the different species are, in fact, distinct hyperfine states of the same atomic gas, it becomes feasible to introduce a coupling mechanism capable of converting one species into another. In this system, we can track the actual population  $P_j$  within each species  $j$  at the time  $t$  by

$$P_j(t) = \frac{\int d\mathbf{r} |\psi_j(\mathbf{r}, t)|^2}{\int d\mathbf{r} \left[ |\psi_1(\mathbf{r}, t)|^2 + |\psi_2(\mathbf{r}, t)|^2 \right]}, \quad (2.25)$$

where in this case the normalization stands for  $N = N_1 + N_2$ .

## 2.2 Bogoliubov-de Gennes theory

As we introduced in section 2.1, the Bose-Einstein condensate of a dilute gas can be well described by GP equation (2.19). Around the equilibrium, the system can have small-amplitude oscillations, they are elementary excitations on the stationary solution  $\psi(\mathbf{r}, t) = \psi(\mathbf{r})e^{-i\mu t}$ , where  $\mu \approx \partial E / \partial N$  is the chemical potential of the system, which stands for the total energy  $E$  variation with the number  $N$  of particles [8]. We can write the order parameter under fluctuations as

$$\psi(\mathbf{r}, t) = [\psi(\mathbf{r}) + \eta(\mathbf{r}, t)] e^{-i\mu t}, \quad (2.26)$$

with  $\eta$  given by a linear combination of all possible modes  $k$

$$\eta(\mathbf{r}, t) = \sum_k \left[ u_k(\mathbf{r}) e^{-i\omega_k t} + v_k^*(\mathbf{r}) e^{+i\omega_k^* t} \right], \quad (2.27)$$

where  $u_k$  and  $v_k$  are amplitudes of elementary excitations corresponding to the frequency  $\omega_k$  from the spectrum around the ground state. Since we insert Eqs. (2.27) and (2.26) into GP equation (2.19), and hold no more than second order amplitude terms, we get a system [8]

$$\hbar\omega_k u_k(\mathbf{r}) = \left[ \hat{\mathbf{H}}_{GP}[\psi] + g|\psi(\mathbf{r})|^2 - \mu \right] u_k(\mathbf{r}) + g\psi^2(\mathbf{r})v_k(\mathbf{r}), \quad (2.28a)$$

$$-\hbar\omega_k v_k(\mathbf{r}) = \left[ \hat{\mathbf{H}}_{GP}[\psi] + g|\psi(\mathbf{r})|^2 - \mu \right] v_k(\mathbf{r}) + g\psi^{*2}(\mathbf{r})u_k(\mathbf{r}), \quad (2.28b)$$

which can be written in the matrix form

$$\mathbf{M}\mathbf{u}_k = \omega\mathbf{u}_k, \quad (2.29)$$

where

$$\mathbf{M} = \begin{pmatrix} \left[ \hat{\mathbf{H}}_{GP}[\psi] + g|\psi(\mathbf{r})|^2 - \mu \right] & g\psi^2(\mathbf{r}) \\ -g\psi^{*2}(\mathbf{r}) & -\left[ \hat{\mathbf{H}}_{GP}[\psi] + g|\psi(\mathbf{r})|^2 - \mu \right] \end{pmatrix}, \quad (2.30)$$

and  $\mathbf{u}_k = [u_k(\mathbf{r}) \ v_k(\mathbf{r})]^T$ , where T stands for the transpose operation over a vector. Here we omit the indexes  $k$ , since all eigenvalues are present when we diagonalize the matrix  $\mathbf{M}$ . This system can be called the *Bogoliubov-de Gennes* (BdG) equations [8]. Once we diagonalize this matrix and find all possible modes  $\omega$ , if it exists at least a frequency  $\omega$  with a nonzero imaginary part, this mode grows exponentially, then we call the system dynamically unstable. That is our criterion to study the stability of Bose-Einstein condensates. We are handling a linear stability theory [26], which provides linear equations of motion to describe the possible independent modes, in such a way we can track the behavior of all of them separately and observe if they are going to drive the initial state to an unstable profile. The concept of *Dynamic Stability* holds a distinct physical meaning from that of *Energetic Stability*. The former one is related to how an initial state can be changed by small amplitude perturbations which can grow and take over the dynamics of the system, while the last one is based on the energy profile of a state. In this context, an unfavorable energy configuration can be transformed into a state of lower energy by small oscillations, particularly when dissipation mechanisms come into play [8].

## 2.3 Floquet theory

We consider a system described by Hamiltonian  $\hat{\mathbf{H}}_0(\mathbf{r})$ , which is supported by a complete set of orthonormal eigenfunctions  $\{\phi_j(\mathbf{r})\}$ . We suppose the system perturbed by an external potential  $\hat{\mathbf{H}}_{ext}(\mathbf{r}, t)$  that is a periodic function in time, i.e.,  $\hat{\mathbf{H}}_{ext}(\mathbf{r}, t + T) = \hat{\mathbf{H}}_{ext}(\mathbf{r}, t)$ , where  $T$  is its period. Therefore the perturbed Hamiltonian  $\hat{\mathbf{H}}_F = \hat{\mathbf{H}}_0 + \hat{\mathbf{H}}_{ext}$  is also a periodic function in time. The dynamics of the

system is driven by the Schrödinger equation

$$i\hbar \frac{\partial}{\partial t} \psi(\mathbf{r}, t) = \hat{\mathbf{H}}_F(\mathbf{r}, t) \psi(\mathbf{r}, t) . \quad (2.31)$$

The Floquet theorem [10–12] predicts solutions which are linear combination of functions  $\tilde{\phi}_j(\mathbf{r}, t)$  periodic in time, called Floquet modes

$$\psi(\mathbf{r}, t) = \sum_j c_j \tilde{\phi}_j(\mathbf{r}, t) \exp(-i\varepsilon_j t/\hbar) , \quad (2.32)$$

where  $\varepsilon_j$  are Floquet exponents, sometimes called quasienergies. These concepts are useful to study the dynamics of a linear Schrödinger equation driven by a Hermitian matrix. This is not the case of the Gross-Pitaevskii equation, which is a nonlinear Schrödinger equation. But the collective modes around the solution of the condensate are led by linear equations. And therefore, the Floquet theory can describe how the amplitudes of the elementary excitations evolve with time once we have a system with periodic dynamics.

We have introduced a general theory to study quantum systems driven by a time-periodic Hamiltonian. From now on, we consider a Bose-Einstein condensate with dynamics led by the Gross-Pitaevskii equation. We restrict our study to time-dependent systems, i.e, condensates with spatial homogeneous solutions  $\psi_0(t) = f(t)e^{-i\alpha(t)}$ , where  $f(t)$  is a periodic function with period  $T$  and  $\alpha$  is a real function of time. We suppose small amplitude oscillations around it as

$$\psi(\mathbf{r}, t) = [f(t) + \zeta(\mathbf{r}, t)] \exp[-i\alpha(t)] , \quad (2.33)$$

with

$$\zeta(\mathbf{r}, t) = \sum_k [\tilde{u}_k(t)\varphi_k(\mathbf{r}) + \tilde{v}_k^*(t)\varphi_k^*(\mathbf{r})] , \quad (2.34)$$

where the amplitudes  $\tilde{u}_j$  and  $\tilde{v}_j$  are periodic functions with the same period  $T$  of the function  $f(t)$  and  $\{\varphi_k(\mathbf{r})\}$  is a set of orthonormal eigenfunctions of the free particle Hamiltonian  $\hat{\mathbf{H}}_0 = -\hbar^2 \nabla^2 / 2M$ . In this way, we have  $\hat{\mathbf{H}}_0 \varphi_k(\mathbf{r}) = \epsilon_k \varphi_k(\mathbf{r})$ , where  $\epsilon_k$  are free particle eigenenergies. We insert the perturbed solution (2.33) into the GP equation (2.20), next we neglect amplitude terms going with second (and higher) order, then we get the equations of motion of the elementary excitations [27, 28]

$$i\hbar \frac{d\tilde{u}_k(t)}{dt} = \left[ H_{GP}[f] + g|f(t)|^2 - \frac{d}{dt}\alpha(t) \right] \tilde{u}_k(t) + gf^2(t)\tilde{v}_k(t) , \quad (2.35a)$$

$$-i\hbar \frac{d\tilde{v}_k(t)}{dt} = \left[ H_{GP}[f] + g|f(t)|^2 - \frac{d}{dt}\alpha(t) \right] \tilde{v}_k(t) + gf^{*2}(t)\tilde{u}_k(t) , \quad (2.35b)$$

with  $H_{GP}[f] = \epsilon_k + g|f|^2$ , and we write this system in the matrix form

$$i\hbar \frac{d}{dt} \tilde{\mathbf{u}}(t) = \tilde{\mathbf{M}}(t) \tilde{\mathbf{u}}(t) , \quad (2.36)$$

with  $\tilde{\mathbf{u}}(t) = [\tilde{u}(t) \tilde{v}(t)]^T$  and

$$\tilde{\mathbf{M}}(t) = \begin{pmatrix} [H_{GP}[f] + g|f(t)|^2 - \frac{d}{dt}\alpha(t)] & gf^2(t) \\ -gf^{*2}(t) & -[H_{GP}[f] + g|f(t)|^2 - \frac{d}{dt}\alpha(t)] \end{pmatrix}. \quad (2.37)$$

The system (2.36) is a linear equation, and since the hermitian matrix  $\tilde{\mathbf{M}}(t)$  evolves with the same period of the density  $|\psi_0(t)|^2$ , and therefore by the Floquet theorem [11], the amplitude vector  $\mathbf{u}(t)$  are expected to be led by a periodic function  $\mathbf{p}(t)$

$$\tilde{\mathbf{u}}(t) = e^{\lambda t/\hbar} \mathbf{p}(t), \quad (2.38)$$

in which, for convenience, we use a complex constant  $\lambda$  as the Floquet exponent instead of quasienergies, which is going to return some information about the stability of the dynamics of  $\tilde{\mathbf{u}}(t)$ . If we consider a complete period  $T$ , the periodic mode has the property  $\mathbf{p}(T) = \mathbf{p}(0)$ . Then, we have

$$\tilde{\mathbf{u}}(T) = e^{\lambda T/\hbar} \mathbf{p}(0), \quad (2.39)$$

where we suppose  $\mathbf{p}(0) = \tilde{\mathbf{u}}(0)$ , and so  $\tilde{\mathbf{M}}(t=0) = \mathbf{1}$ , the unitary matrix. If  $\lambda$  has a nonzero real part, then the system is dynamically unstable, since the amplitudes will exponentially grow in time. Then, the initial homogeneous solution is a dynamically stable system only if we have  $\text{Re}(\lambda) = 0$ . This method is sometimes called time-dependent BdG, and is very useful to study the stability of periodic systems. Our presented approach to Floquet stability analysis is mainly based on the method proposed in [27].



## Chapter 3

### Condensates on the spherical bubble

In 2001, Zobay and Garraway introduced the first realistic ideas on how to confine ultracold gases on the surface of a two-dimensional ellipsoidal closed shell [13]. The authors suggest that shell-shaped ellipsoidal gases can be performed by adiabatically tuning parameters of a radio-frequency (rf) induced potential. However, once we take into account the inherent Earth gravitational force, the atoms are energetically favored to populate the bottom of the trap. The same authors tried to overcome this challenge by considering the use of a dipole optical potential as a gravitational compensation [14]. But actually, the experimental research groups did not follow this approach. It is a hard task to compensate the gravitational force. An alternative experimental set up to mimic weightless atoms is a free fall experiment performed in a tower of 146 meters at the Center of Applied Space Technology and Microgravity (ZARM) in Bremen, Germany [29], see Fig. 3.1a. The Ernst Rasel's group perform an ingenious maneuver that allow a 5- second free fall condition, which also has shown that, in these conditions, the experiment can be handled with trap potentials weaker than in standard experiments. Indeed, this set up accomplished temperatures of 50 picokelvins, the coldest sample ever performed at that time. In this way, to avoid the gravitational effect enables to reach not only low dimensional topologies, but also to achieve colder condensates. Recently, experimental groups shed new light on the pathway suggested by Zobay and Garraway in 2001. But this time, these ideas were performed in a microgravity environment, the NASA cold atom laboratory (CAL) aboard the international space station (ISS) [15, 16, 30, 31] see Fig. 3.1b. In the absence of the gravitational sag, a bubble trap enables to get ultracold gases on an ellipsoidal two-dimensional closed surface. Besides this great achievement, other researchers did not give up to handle bubble condensates on Earth. New alternatives were proposed, the first one explores the immiscible property of a Bose-Bose mixture in order to keep one of the species covering the other as a shell [32]. It was experimentally handled with two immiscible condensate species [33], in such a way that one of the species behaves like a core, and the second one behaves as a shell, see Fig. 3.1c. Then, the core cloud is released without affecting the shell condensate. And therefore, for a short time is obtained a quasi-spherical bubble, which is unsta-

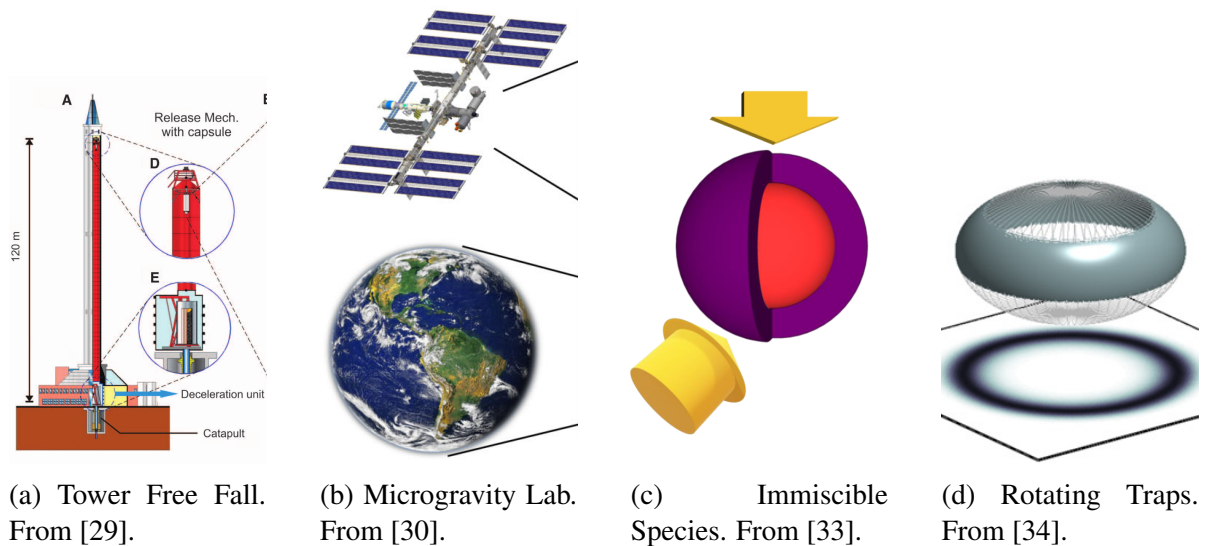


Figure 3.1: Available experimental setups to handle bubble shaped cold gases.

ble and no longer keeps its shape. The second alternative is based on performing fast rotation of the trap. In this case, the condensate is not going to become a spherical- or ellipsoidal-like bubble, but instead it reaches a ring-bubble shape [34], see Fig. 3.1d.

Many groups of the community of cold atom physics are currently interested in the fundamental properties of condensates in microgravity environments, where not only 2D bubbles are investigated, but also matter-wave lensing, metrology and a search for picoKelvin energy scales. We can highlight important experimental and theoretical works in China [33], England-France [13, 14, 34–37], Germany [29, 32, 38–48], Italy [49–53], and USA [15–17, 54–58]. And a next generation of experiments in microgravity environments will be performed by a bilateral project by Germany and USA [31, 48].

At this moment, we have several research groups in Brazil working on cold atom physics in the bubble. Specially in São Paulo state, we have four universities publishing works on this subject. Indeed, in the present year São Paulo was the host of an international workshop focused in low dimensional physics of quantum gases <sup>1</sup>. Among all posters and talks, the physics of Bose-Einstein condensates on the bubble was one of the major topics. In order to acknowledge the main works performed in Brazil in the last four years, we are going to discuss next some achievements. The first study in the context of bubbles was carried out in 2019 at São Carlos Institute of Physics (IFSC) by the group of Vanderlei S. Bagnato [59], where was investigated the condensation critical temperature for traps with spherical symmetry, by observing bubbles described by a spherical box and also a thick shell [59]. In 2020, the group of Francisco E. A. dos Santos at Federal University of São Carlos (UFScar) has started to perform deep analyses of the effect of curved manifolds on the interaction and stability of condensates [60, 61]. Also in 2020, Emanuel A. L. Henn (IFSC)

<sup>1</sup>Please visit <https://www.ictp-saifr.org/ldqg2023>

and Aristeu R. P. Lima from University of International Integration of Afro-Brazilian Lusofonia (UNILAB) have led another branch of research, particularly studying polarized dipolar condensates in bubble traps. In this context, it was possible to investigate the influence of the long-range and anisotropic dipole-dipole interaction on collective excitations in the limit of a thin shell [62]. Since 2021, Mônica Caracanhas (IFSC) has handled classical fluid mechanics approaches to study dynamics of vortices on the surface of the sphere, spheroids and another revolution surfaces [63, 64]. She also has explored vortex-lattices and macro-vortex physics in the context of ring bubbles [65]. At Institute of Physics (IFUSP) and at Institute of Theoretical Physics (IFT), Arnaldo Gammal, Lauro Tomio, and the present Thesis' author, Leonardo Brito, have been investigating the dynamic stability of Bose-Bose mixtures trapped on the surface of sphere [18, 19].

In this chapter, we provide a direct derivation of a quasi-2D model we intend to handle for describing the system of Bose-Einstein condensates confined on the surface of spherical ideal bubbles. In section 3.1, we introduce the trap potential usually performed to confine gases in bubbles. Next, we derive the dimensionally-reduced equations in Sec. 3.2, and finally, in Sec. 3.3, we provide estimations to support the validity of our model, which will be extensively employed along the following chapters.

### 3.1 Ultracold gas trapped on the bubble

In 2001, Zobay and Garraway [13] have introduced an experimental pathway to get an effectively two-dimensional matter-wave bubble starting from a loaded atomic ultracold gas confined by a conventional magnetic trap by performing adiabatic deformation. A few years later, the authors have extended the model to Bose-Einstein condensates [14], where the ultracold gas is well described by the Gross-Pitaevskii equation. Next, we briefly discuss how the condensates can be confined in an effective two-dimensional shell. By employing radio-frequency-induced adiabatic potentials, two or more internal atomic states are coupled by a strong resonant external field, in such a way that the atomic motion is no longer driven by the *bare* potentials, but is better described by *dressed states*.

Consider a condensed atomic gas, for which we have two hyperfine states  $\psi_1$  and  $\psi_2$  available. For example, for  $^{87}\text{Rb}$ , it is possible to handle a mixture of the states  $|1\rangle = |F = 1, m_F = -1\rangle$  and  $|2\rangle = |F = 2, m_F = 1\rangle$  [66]. For simplicity, we consider that both species can be trapped by the same three-dimensional spherical harmonic potential  $V_h(r) = M\omega_0^2 r^2/2$ , where  $r = |\mathbf{r}|$  is the absolute value of the position  $\mathbf{r} = (x, y, z)$ . Then, once we prepare a condensate in the first state  $|1\rangle$ , we can turn on an external field with induced-field coupling of strength  $\Omega_Z(t)$  tuned in such a way that a Zeeman sublevel  $|2\rangle$  can be coupled to the first state. Therefore, we

can write the coupled Gross-Pitaevskii equations in the interaction picture [14] as

$$\begin{aligned} i\hbar \frac{\partial \psi_1}{\partial t} &= \left[ -\frac{\hbar^2}{2M} \nabla^2 + V_t - \frac{1}{2} \Delta(t) \right] \psi_1 + \hbar \Omega_Z(t) \psi_2 \\ &+ \left( g_{11} |\psi_1|^2 + g_{12} |\psi_2|^2 \right) \psi_1, \end{aligned} \quad (3.1a)$$

$$\begin{aligned} i\hbar \frac{\partial \psi_2}{\partial t} &= \left[ -\frac{\hbar^2}{2M} \nabla^2 + V_t + \frac{1}{2} \Delta(t) \right] \psi_2 + \hbar \Omega_Z(t) \psi_1 \\ &+ \left( g_{22} |\psi_2|^2 + g_{21} |\psi_1|^2 \right) \psi_2, \end{aligned} \quad (3.1b)$$

where the external field has a frequency detuning given by  $\Delta(t) = \hbar \omega_f - \Delta E$ , with the frequency of the field given by  $\omega_f$ , and the energy difference between the coupled sublevels  $|1\rangle$  and  $|2\rangle$  given by  $\Delta E$ . The interaction parameters  $g_{ij}$  are given by the standard definition  $g_{ij} = 4\pi \hbar^2 a_{ij} / M$ , where  $a_{ij}$  stands for the s-wave scattering length for intra- and inter-species interactions. The gravitational force is taken into account by observing the total potential

$$V_t(x, y, z) = MGz + V_h(r), \quad (3.2)$$

where  $G$  is the Earth gravitational acceleration. If we handle a transformation  $\psi_j = \phi_j / 4\pi r$ , with  $j = 1, 2$ , we are able to rewrite Eqs. (3.1a) and (3.1b) as

$$\begin{aligned} i\hbar \frac{\partial \phi_1}{\partial t} &= \left[ -\frac{\hbar^2}{2M} \frac{\partial^2}{\partial r^2} + V_t - \frac{1}{2} \Delta(t) \right] \phi_1 + \hbar \Omega_Z(t) \phi_2 \\ &+ \left( g_{11} |\phi_1|^2 + g_{12} |\phi_2|^2 \right) \frac{\phi_1}{r^2}, \end{aligned} \quad (3.3a)$$

$$\begin{aligned} i\hbar \frac{\partial \phi_2}{\partial t} &= \left[ -\frac{\hbar^2}{2M} \frac{\partial^2}{\partial r^2} + V_t + \frac{1}{2} \Delta(t) \right] \phi_2 + \hbar \Omega_Z(t) \phi_1 \\ &+ \left( g_{22} |\phi_2|^2 + g_{21} |\phi_1|^2 \right) \frac{\phi_2}{r^2}, \end{aligned} \quad (3.3b)$$

for which we have the normalization condition  $\int_0^\infty dr \left( |\phi_1|^2 + |\phi_2|^2 \right) = 1$ . If we neglect the the gravitational acceleration, the equations (3.3a) and (3.3b) can be written in a basis that diagonalize the potential and the coupling at each point. At this basis, the eigenstates  $\phi_\pm$  are the *dressed states*. And for a sufficiently strong field, we have the adiabatic potentials

$$V_\pm(r, t) = \pm \frac{1}{2} M \omega_0^2 \sqrt{[r^2 - \Delta(t)]^2 + [2\Omega_Z(t)]^2}, \quad (3.4)$$

which provides a shell trapping potential. We can consider all interactions approximately the same, i.e,  $g_{ij} \approx g$ . At this conditions, we can describe one of the eigenfunctions  $\phi = \phi_+$  by the GP equation

$$i\hbar \frac{\partial \phi}{\partial t} = \left[ -\frac{\hbar^2}{2M} \frac{\partial^2}{\partial r^2} + V_{bubble} + g|\phi|^2 \right] \phi, \quad (3.5)$$

with the effective bubble trap potential

$$V_{bubble}(r, t) = \frac{1}{2}M\omega_0^2\sqrt{[r^2 - \Delta(t)]^2 + [2\Omega_Z(t)]^2}. \quad (3.6)$$

Despite the time-dependence in the bubble trap, we change parameters  $\Omega_Z$  and  $\Delta$  in a much slower time compared to the time of the condensate dynamics. They are adiabatically changed in order to control the width and radius of the shell. The adiabatic expansion is supposed to be sufficiently slow to avoid nonadiabatic excitations, however fast enough to avoid losses from leakage [13]. We can see how the detuning parameter  $\Delta$  can be tuned in order to expand the bubble radius in Fig. 3.2.

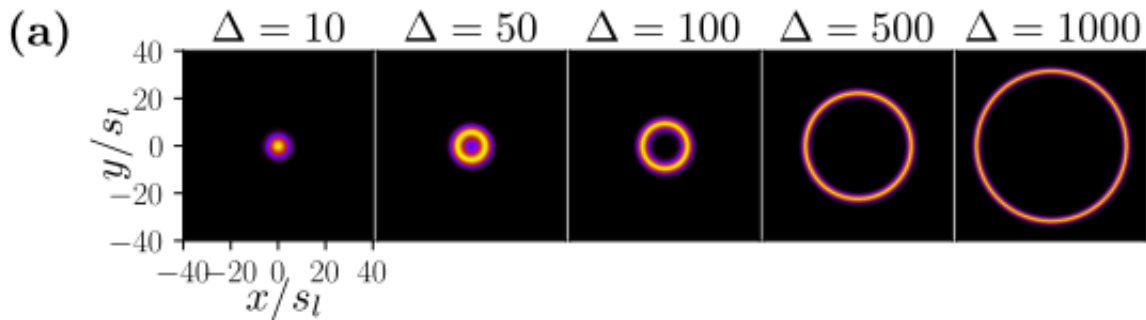


Figure 3.2: Dressed potential and matter-wave shell at microgravity environment. From [58].

In Fig. 3.3, we present how the potential proposed by Zobay and Garraway is affected by the gravity acceleration, by considering the bare potentials, and also the radio-frequency (rf) field- induced dressed potentials. In 2019, bubble trap was fi-

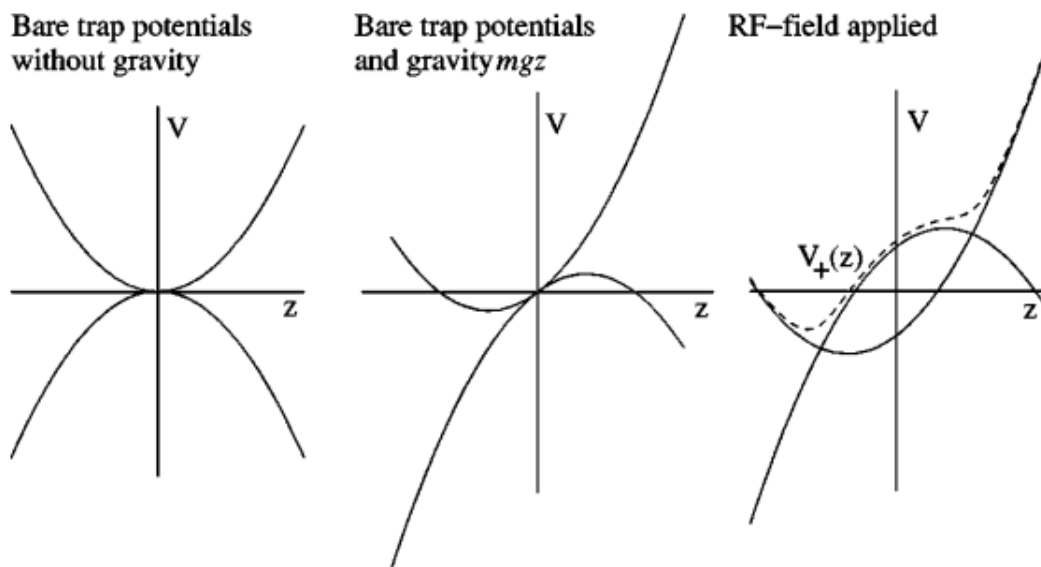


Figure 3.3: Bare and dressed potential under effect of the gravity. From [14].

nally applied in microgravity conditions aboard Cold Atom Laboratory at International Space Station, where the lab is in a continuous free fall, experiencing only a residual force corresponding to an effective gravitational acceleration around  $0.005G$

[17], which does not significantly affect the shell potential. The  $^{87}\text{Rb}$  ultracold atomic gas can be trapped in dressed potential shell as depicted in Fig. 3.4, where the atoms do not pool at the bottom of the trap and form ellipsoidal quasi-homogeneous 2D bubbles, see Fig. 3.5.

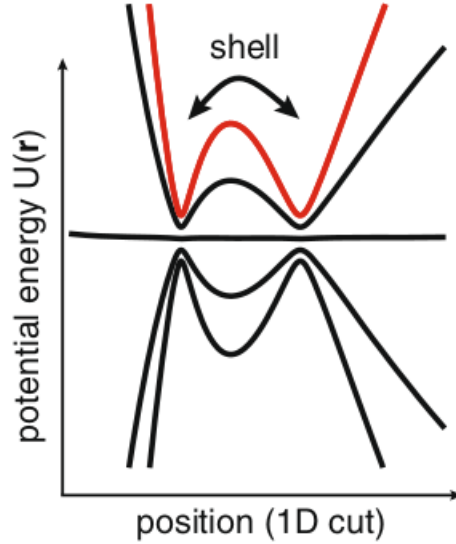


Figure 3.4: Dressed potential and matter-wave shell at microgravity environment. From [16].

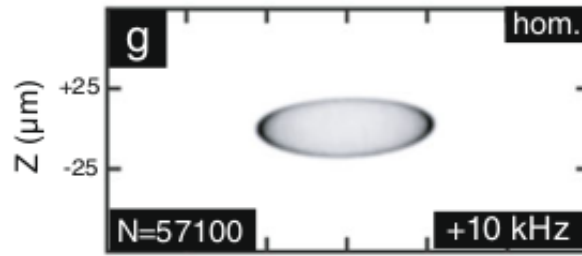


Figure 3.5: Matter-wave bubble. From [16].

From now on, we consider the system already configured in the dressed adiabatic potentials, in such a way the effective GP equation describing the wave function  $\Psi_0$  of a condensed-ultracold gas confined in the bubble trap is

$$i\hbar \frac{\partial \Psi_0}{\partial t} = \left[ -\frac{\hbar^2}{2M} \nabla^2 + V_{bubble} + g|\Psi_0|^2 \right] \Psi_0, \quad (3.7)$$

with the effective bubble trap potential

$$V_{bubble}(r, t) = \frac{1}{2} M \omega_0^2 \sqrt{[r^2 - \Delta]^2 + [2\Omega_Z]^2}. \quad (3.8)$$

In the following sections, we present a dimensional-reduction GP equation in the limit of a very thin shell, and we discuss the validity of this approximation by considering realistic parameters.

### 3.2 Dimensional reduction

In this section, we aim to show that realistic parameters provide enough reasons to believe that an ideal two-dimensional framework is a suitable model to study condensates trapped in bubbles. From now on, we derive a dimensional-reduced model by assuming the bubble-trap (3.8) in the limit of a thin shell.

In a first approximation, we can suppose an ansatz function for the ground state of the system as separable in radial and angular solutions

$$\Psi_0(r, \theta, \phi, t) = f(r)\psi(\theta, \phi, t), \quad (3.9)$$

where the dynamics is supposed to be restricted to angular variables. We assume separate normalization conditions

$$\int_0^\infty dr r^2 |f(r)|^2 = 1, \quad (3.10a)$$

$$\int_0^{2\pi} d\phi \int_0^\pi d\theta \sin \theta |\psi(\theta, \phi, t)|^2 = 1. \quad (3.10b)$$

The GP equation can be rewritten as

$$i\hbar f \frac{\partial \psi}{\partial t} = -\frac{\hbar^2}{2M} \left[ \psi \nabla_r^2 f + \frac{f}{r^2} \nabla_{\theta, \phi}^2 \psi \right] + V_{bubble} f \psi + g |f|^2 |\psi|^2 f \psi, \quad (3.11)$$

where

$$\nabla_r^2 = \frac{1}{r^2} \frac{\partial}{\partial r} \left( r^2 \frac{\partial}{\partial r} \right), \quad (3.12a)$$

$$\nabla_{\theta, \phi}^2 = \frac{1}{\sin^2 \theta} \left[ \sin \theta \frac{\partial}{\partial \theta} \left( \sin \theta \frac{\partial}{\partial \theta} \right) + \frac{\partial^2}{\partial \phi^2} \right]. \quad (3.12b)$$

Multiplying Eq. (3.11) by  $f^*$ , we get

$$i\hbar |f|^2 \frac{\partial \psi}{\partial t} = -\frac{\hbar^2}{2M} \left[ \psi f^* \nabla_r^2 f + \frac{|f|^2}{r^2} \nabla_{\theta, \phi}^2 \psi \right] + V_{bubble} |f|^2 \psi + g |f|^4 |\psi|^2 \psi, \quad (3.13)$$

which we integrate in the  $r$  variable, following a protocol to get a dimensional reduced equation [67]

$$i\hbar I_1 \frac{\partial \psi}{\partial t} = -\frac{\hbar^2}{2M} [I_2 + I_3 \nabla_{\theta, \phi}^2] \psi + I_4 \psi + g I_5 |\psi|^2 \psi, \quad (3.14)$$

or also

$$i\hbar \frac{\partial \psi}{\partial t} = \left( -\frac{\hbar^2 \kappa_1}{2M} \nabla_{\theta, \phi}^2 + \kappa_2 g |\psi|^2 + \kappa_3 \right) \psi, \quad (3.15)$$

where

$$\kappa_1 = \frac{I_3}{I_1}, \kappa_2 = \frac{I_5}{I_1}, \kappa_3 = \frac{1}{I_1} \left( -\frac{\hbar^2}{2M} I_2 + I_4 \right), \quad (3.16)$$

and

$$I_1 = \int_0^\infty dr r^2 |f(r)|^2, \quad (3.17a)$$

$$I_2 = \int_0^\infty dr r^2 f^*(r) \nabla_r^2 f(r), \quad (3.17b)$$

$$I_3 = \int_0^\infty dr |f(r)|^2, \quad (3.17c)$$

$$I_4 = \int_0^\infty dr r^2 V_{bubble}(r) |f(r)|^2, \quad (3.17d)$$

$$I_5 = \int_0^\infty dr r^2 |f(r)|^4. \quad (3.17e)$$

$$(3.17f)$$

By supposing  $\tilde{\psi}(\theta, \phi, t) = \psi(\theta, \phi, t) \exp(i\kappa_3 t/\hbar)$ , we get the transformed two-dimensional GP equation

$$i\hbar \frac{\partial \tilde{\psi}}{\partial t} = \left( -\frac{\hbar^2 \kappa_1}{2M} \nabla_{\theta, \phi}^2 + \kappa_2 g |\tilde{\psi}|^2 \right) \tilde{\psi}, \quad (3.18)$$

which is a suitable model since the values of  $I_j$  ( $j = 1, \dots, 4$ ),  $\kappa_1$ , and  $\kappa_2$  are finite constants. We can assume a trial function for  $f(r)$  [14] as

$$f(r) = \frac{A}{r} \exp \left[ -\frac{(r - R_0)^2}{2\sigma^2} \right], \quad (3.19)$$

and once we have  $f(r) = u(r)/r$ , the density  $|u|^2$  is a Gaussian function centered at  $R_0$  with width  $\sigma$ . It gives us some insight about the thickness  $\delta R$  of the bubble, that is supposed to be around  $\sigma$ . The Gaussian decays significantly toward the center of the trap. Once the solution is zero for  $r < 0$ , as an approximation, we consider the integrals in the interval of  $[-\infty, \infty]$ . Therefore, the normalization condition can be set as

$$|A|^2 \int_{-\infty}^\infty dr e^{-(r-R_0)^2/\sigma^2} = 1, \quad (3.20)$$

and we get  $A = 1/(\sigma^{1/2} \pi^{1/4})$ , once  $\int_{-\infty}^\infty d\tilde{r} \exp(-\tilde{r}^2) = \sqrt{\pi}$ , with  $\tilde{r} = (r - R_0)/\sigma$ . We are able to calculate the integrals and get

$$I_1 = 1, \quad (3.21a)$$

$$I_2 = \frac{3}{2\sigma^2}, \quad (3.21b)$$

$$I_3 = \frac{1}{R_0^2}, \quad (3.21c)$$

$$I_4 = M\omega_0^2 \sqrt{(R_0^2 - \Delta)^2/4 + \Omega_Z^2}, \quad (3.21d)$$

$$I_5 = \frac{1}{\sqrt{2\pi} R_0^2 \sigma}, \quad (3.21e)$$



where we neglect terms going with second or higher order in  $\sigma$ , once it is related to the thickness of the bubble shell. For large  $\Delta$ , we expect  $\sigma \sim 1/\sqrt{\Delta}$ , in order to keep  $\kappa_3$  a finite constant. In conclusion, we get the effective two-dimensional GP equation

$$i\hbar \frac{\partial \tilde{\psi}}{\partial t} = \left( -\frac{\hbar^2}{2MR_0^2} \nabla_{\theta,\phi}^2 + g_{2D} |\tilde{\psi}|^2 \right) \tilde{\psi}, \quad (3.22)$$

where

$$g_{2D} = \frac{g}{\sqrt{2\pi R_0^2 \delta R}}, \quad (3.23)$$

since we consider  $\delta R \approx \sigma$ .

### 3.3 Validity of a two-dimensional approximation

After obtaining the effective GP equation for describing the dynamics of a condensate trapped on the surface of a spherical shell, the next step is to investigate the conditions under which this model is valid. We must establish that the interaction energy is significantly lower than energy required to drive the system from the ground state to the first radial excited state, in such a way the system is confined into the ground state of a radial solution. And therefore, the dynamics can be fully described by the quasi-2D model.

First, we assume the non-interacting system, where the system is described by Schrödinger equation

$$i\hbar \frac{\partial \Psi}{\partial t} = \left[ -\frac{\hbar^2}{2M} \nabla^2 + V_{trap} \right] \Psi. \quad (3.24)$$

We suppose the limit where the gas is confined in a thin shell, and the effective potential can be well described by a spherical box potential  $V_{trap} = V_{box}$  [59]

$$V_{box}(r) = \begin{cases} 0, & r \leq R_0, \\ \infty, & r > R_0, \end{cases}$$

for which we suppose the stationary solutions

$$\psi(\theta, \phi, t) = Y_{\ell,m}(\theta, \phi) e^{-i\epsilon t/\hbar}. \quad (3.25)$$

Inside the box, we have the radial equation

$$\epsilon_{k\ell} f_k = -\frac{\hbar^2}{2M} \left[ \nabla_r^2 + \frac{\ell(\ell+1)}{r^2} \right] f_k, \quad (3.26)$$

or also

$$\epsilon_{k\ell} u_k = -\frac{\hbar^2}{2M} \left[ \frac{d^2}{dr^2} + \frac{\ell(\ell+1)}{r^2} \right] u_k, \quad (3.27)$$

for which we have solutions

$$u_k(r) = r [A j_\ell(kr) + B n_\ell(kr)] , \quad (3.28)$$

where  $j_\ell$  and  $n_\ell$  are the *Bessel* and *Neumann* functions, respectively. By supposing a thick shell with width  $\delta R$  around the radius  $R_0$ , we have to assure

$$u_k \left( R_0 \pm \frac{\delta R}{2} \right) = 0 , \quad (3.29)$$

which can be written as

$$\frac{B}{A} = - \frac{j_\ell [k(R_0 \pm \delta R/2)]}{n_\ell [k(R_0 \pm \delta R/2)]} . \quad (3.30)$$

In the low energy approximation, we can consider only the angular mode  $\ell = 0$ , and once  $j_0(x) = \sin(x)/x$  and  $n_0(x) = -\cos(x)/x$ , we get

$$\tan [k(R_0 - \delta R/2)] = \tan [k(R_0 + \delta R/2)] , \quad (3.31)$$

and once we suppose  $y = k(R_0 - \delta R/2)$ , we have  $\tan(y) = \tan(y + k\delta R)$ . We can relate the period  $\pi$  of tangent function with the parameters as

$$k_n = n \frac{\pi}{\delta R} , \quad (3.32)$$

and the energy  $\epsilon_{k\ell}$  for the mode  $\ell = 0$  can be written as

$$\epsilon_{n0} = \frac{\hbar^2}{2M} k_n^2 , \quad (3.33)$$

and the energy difference between the ground state and first excited state is  $\Delta\epsilon = \epsilon_{20} - \epsilon_{10}$ , or also

$$\Delta\epsilon = \frac{3}{2} \frac{\hbar^2 \pi^2}{M \delta R^2} . \quad (3.34)$$

Now we can investigate the order of the interaction energy by carrying out the approximation of low energy where  $\ell = 0$ . We want to assure that we have a finite solution at  $r = 0$ , and then we impose  $B = 0$ , and in the range  $[R_0 - \delta R/2, R_0 + \delta R/2]$ , we have the normalized solution

$$u_k(r) = \sqrt{\frac{2}{\delta R}} \sin(kr) . \quad (3.35)$$

The ground-state interaction energy is

$$E_{int} = \frac{g}{2} \int_0^{2\pi} d\phi \int_0^\pi d\theta \sin\theta \int_{R_0 - \delta R}^{R_0 + \delta R} dr r^2 \frac{|u_k Y_{00}|^4}{r^4} \approx \frac{3}{16\pi} \frac{g}{R_0^2 \delta R} , \quad (3.36)$$

where we assume  $r \approx R_0 + \mathcal{O}(\delta R^2)$ , with  $R_0 \gg \delta R$ . And therefore, the ratio  $\gamma$  between the energies is

$$\gamma = \frac{E_{int}}{\Delta\epsilon} \approx \frac{1}{8\pi} \frac{Mg\delta R}{\hbar^2 R_0^2}, \quad (3.37)$$

and once  $g = 4\pi\hbar^2 a_s/M$ , we get  $\gamma = a_s\delta R/2R_0^2$ . If we suppose atomic gas of Rubidium  $^{87}\text{Rb}$  that is performed at the NASA spatial laboratory [17], we can consider realistic parameters as scattering length  $a_s \approx 5 \times 10^{-9}$  meters, bubble with radius around  $R_0 \approx 0.5 \times 10^{-3}$  meters, and thickness about 25% of the radius  $\delta R = 0.25R_0$ , we get  $\gamma \approx 10^{-7}$ . this approach ensures that interactions can not induce radial excitations in the condensate, since the energy gap is significantly higher than the interaction energy, and therefore, the bubble can be well described in a 2D model, as we intend to do. Then, from now on we consider the effective GP equation

$$i\hbar \frac{\partial \tilde{\psi}}{\partial t} = \left[ -\frac{\hbar^2}{2MR_0^2} \nabla_{\theta,\phi}^2 + g_{2D} |\tilde{\psi}|^2 \right] \tilde{\psi}, \quad (3.38)$$

with

$$g_{2D} = \frac{\sqrt{8\pi}\hbar^2 a_s}{MR_0^2 \delta R}. \quad (3.39)$$

### 3.4 Dimensionless model

Once we have a 2D-reduced model to describe Bose-Einstein condensates in Eq. (3.38), it is convenient to handle our problems in dimensionless form. For this purpose, we can write length in units of the radius  $R_0$ , energy in units of  $\hbar^2/MR_0^2$ , and time in units of  $MR_0^2/\hbar$ . If we introduce the dimensionless time variable  $\tilde{t} = \hbar t/MR_0^2$ , we get

$$i \frac{\partial \tilde{\psi}}{\partial \tilde{t}} = \left[ -\frac{1}{2} \nabla_{\theta,\phi}^2 + \tilde{g} |\tilde{\psi}|^2 \right] \tilde{\psi}, \quad (3.40)$$

where we have  $\tilde{g} = (MR_0^2/\hbar^2)g_{2D}$ , or also  $\tilde{g} = \sqrt{8\pi}a_s N/\delta R$ . For convenience, we drop the tildes and write the dimensionless GP equation as

$$i \frac{\partial \psi}{\partial t} = \left[ -\frac{1}{2} \nabla_{\theta,\phi}^2 + g |\psi|^2 \right] \psi. \quad (3.41)$$

Yet we aim to explore mixture features, in this thesis we focus only in mixture of different hyperfine states of the same atomic species, i.e, we handle mass-balanced mixtures, so we have to deal with only one atomic mass. Therefore, the GP model for a binary mixture become

$$i \frac{\partial \psi_j}{\partial t} = \left[ -\frac{1}{2} \nabla_{\theta,\phi}^2 + g_{11} |\psi_1|^2 + g_{12} |\psi_2|^2 \right] \psi_1, \quad (3.42a)$$

$$i \frac{\partial \psi_2}{\partial t} = \left[ -\frac{1}{2} \nabla_{\theta,\phi}^2 + g_{22} |\psi_j|^2 + g_{21} |\psi_1|^2 \right] \psi_2, \quad (3.42b)$$

where the indexes  $j = 1, 2$  state for the hyperfine states. This is a standard model for describing a condensate mixture [8], where atoms interact with their own species and with the other one only by the contact interactions, depicted in the interaction parameters  $g_{11}$ ,  $g_{22}$  (intra-species interactions), and  $g_{21} = g_{12}$  (inter-species interactions). This is a simplified model, which we handle in chapter 4. However, in chapter 5, we also take into account that atoms can be transferred from a state to the other by Rabi oscillations. In the latter case we have to handle a GP coupled system with additional terms, which we shall introduce later.

# Chapter 4

## BEC Mixtures Stability

Bose-Einstein condensate mixtures represent an important field of study of cold atoms, where particular properties like interchange of angular momentum and stable currents are found and can be modulated by few parameters like the intra- (between the same species) and inter-species (between different species) interactions. These structures can be set in practice with the same bosonic isotopes in different hyperfine states, or different isotopes, or even different atoms [7]. The mixtures can hold stable persistent currents, and are able to work like a matter-wave circuit, which make them very relevant to atomtronics future applications [68], and therefore here we have a rich framework to explore.

One of the main problems is to study the stability of the mixture on the spherical shell. In practice, such a topology can be performed with bubble traps in laboratories in a space station at low gravity conditions [16]. This is an interesting geometry which can present some features found in annulus geometries, like stable persistent currents. And we also can observe the effects of miscibility and competition of angular modes, which can take over the system. We present new studies, exploring the angular geometry, and carrying out a deep analysis of the interaction role on stability when we have hidden vorticity [18].

Interactions can change the spatial distribution of the species, in such a way that they overlap or not, i.e, the miscibility is related with the interactions and the initial stationary states can be led to very different ones. Another way we can use to track the instability is to observe the unstable modes from the Bogoliubov-de Gennes spectrum [7,8]. Depending on the geometry we are studying, it is possible to observe the modes breaking the condensates into pieces [25, 69].

This chapter is organized as follows. In section 4.1, we extend the mean-field model to take into account mixtures, and particularly, binary mixtures. Next, we employ techniques to study stability and dynamics. In Sec. 4.2, we focus on homogeneous solutions, and we present an analytical study of the BdG spectrum and compare it with the overlap behavior when we find the ground state of the mixture. In sec. 4.3, we observe the *hidden-vorticity* (HV) configurations, where we have vortex- and antivortex- states, with each species achieved with the same vortex

charge, but with different signs. In this system, we have inhomogeneous but miscible initial states for which we perform a variational study of the states and energy in 4.3.1. Next, BdG spectrum can provide the spectrum of the elementary excitations, from which we can predict the stability of the initial state, once the inter-species interactions start to affect the system, see 4.3.2. In 4.3.3, we analyze the dynamics of some systems supposed to be unstable, and confirm that an unstable mode is able to break the atomic clouds into immiscible pieces. Finally, in Sec. 4.4, we summarize the main conclusions our results have provided. Our main results, can be found in the published paper [18].

## 4.1 Model

Recently, some experiments were performed using bubble traps schemes, where the BEC is confined to the surface of an ellipsoidal, or spherical shell in microgravity settings at the Nasa Cold Atom Laboratory (CAL) aboard the international space station [16]. Therefore, it means a new feasible closed geometry, where we can find properties around the persistent currents as observed for annulus geometries. Then, spherical shells provide an opportunity to observe interesting features. In this context, we can study mixtures on the shell and study their stability by observing the angular unstable modes and also the miscibility.

Our main focus is to observe the role of unstable angular modes from the BdG spectrum on the initial stationary states, which can be homogeneous for the non-vorticity regime, or inhomogeneous when we consider hidden vorticity (HV). In both cases, we start with miscible species. But we remark that in the HV case, the miscibility can not be connected with homogeneity as we perform with non-vorticity problems, since the inhomogeneous solution is straightly related with the vorticity, regardless of the immiscibility. The mixture interactions can make the unstable angular modes grow, and once that happens, these modes are able to split the condensate into few pieces [25, 69].

A BEC mixture on the spherical shell can be described in the dimensional-reduced model for GP already developed in Sec. 3.2. Here, in order to follow the notation from our work [18], we change some variables to get a dimensionless problem. Then, each species  $j$  is driven by the GP equation

$$i \frac{\partial \psi_j}{\partial t} = \left[ -\frac{1}{2} \nabla_{\theta, \phi}^2 + \gamma_{jj} |\psi_j|^2 + \gamma_{jk} |\psi_k|^2 \right] \psi_j, \quad (4.1)$$

where  $j, k = 1, 2$ , with  $k \neq j$ , and

$$\nabla_{\theta, \phi}^2 \psi_j \equiv \frac{1}{\sin \theta} \frac{\partial}{\partial \theta} \left( \sin \theta \frac{\partial \psi_j}{\partial \theta} \right) + \frac{1}{\sin^2 \theta} \frac{\partial^2 \psi_j}{\partial \phi^2}. \quad (4.2)$$

The number of atoms  $N_j$  is set into the interaction parameter  $\gamma_{jk} = g_{jk}N_j$  [18], and the normalization conditions are

$$\int d\phi d\theta \sin \theta |\psi_j(\theta, \phi)|^2 = 1, \quad (4.3)$$

with  $0 \leq \theta \leq \pi$ ,  $0 \leq \phi \leq 2\pi$  and  $\psi_j(\theta, 0) = \psi_j(\theta, 2\pi)$ . We can search for stationary solutions where the species carry some angular momentum, then we set the ansatz

$$\psi_j(\theta, \phi, t) = \frac{f_j(\theta)}{\sqrt{2\pi}} \exp [i(s_j\phi - \mu_j t)], \quad (4.4)$$

with  $f$  a real function, normalized to 1/2, and  $s_j$  imposes a vorticity on the solution. We get a one-dimensional time-independent GP

$$\mu_j f_j = -\frac{1}{2} \frac{1}{\sin \theta} \frac{\partial}{\partial \theta} \left( \sin \theta \frac{\partial f_j}{\partial \theta} \right) + \frac{1}{2} \frac{s_j^2 f_j}{\sin^2 \theta} + \frac{\gamma_{jj}}{2\pi} f_j^3 + \frac{\gamma_{jk}}{2\pi} f_k^2 f_j, \quad (4.5)$$

therefore, the chemical potential can be written as

$$\mu_j = \int d\phi d\theta \sin \theta \left[ \frac{1}{2} \left( \left| \frac{\partial f_j}{\partial \theta} \right|^2 + \frac{s_j^2}{\sin^2 \theta} |f_j|^2 \right) \frac{\gamma_{jj}}{2\pi} |f_j|^4 + \frac{\gamma_{jk}}{2\pi} |f_j|^2 |f_k|^2 \right], \quad (4.6)$$

and the total energy

$$E = \int d\phi d\theta \sin \theta \sum_{j,k=1, k \neq j}^2 \left[ \frac{1}{2} \left( \left| \frac{\partial f_j}{\partial \theta} \right|^2 + \frac{s_j^2}{\sin^2 \theta} |f_j|^2 \right) + \frac{\gamma_{jj}}{4\pi} |f_j|^4 + \frac{\gamma_{jk}}{4\pi} |f_j|^2 |f_k|^2 \right]. \quad (4.7)$$

If we have  $s_j = 0$ , then  $f_j(\theta) \neq 0$  at the poles  $\theta = 0, \pi$ . But if we have  $s_j \neq 0$ , so  $f_j(\theta) = 0$  at the poles. With the ansatz in Eq. (4.4) we are able to set a vortex pair localized at the sphere poles. If we set  $s_1 = s$  and  $s_2 = -s$ , where  $s > 0$ , the system presents a *hidden-vorticity* (HV) [25, 69], since the species have opposite vorticity, whereas  $s = 0$  defines a homogeneous system.

When the condensates have vortex charge, they eventually can exchange angular momentum. And therefore it is useful to define the angular momentum operator  $\mathbf{L} = -\hat{z}i \frac{\partial}{\partial \phi}$  for each species

$$\langle L_z \rangle_j = -i \int d\phi d\theta \sin \theta \psi_j^* \frac{\partial \psi_j}{\partial \phi}, \quad (4.8)$$

which is supposed to be a constant  $\langle L_z \rangle_j = s_j$ , if the proposed solutions in Eq. (4.4) are stable.

## 4.2 Homogeneous system

Here we present a semi-analytical analysis for non-charged system, i.e,  $s_1 = s_2 = 0$ , for which the solutions are given by  $\psi_j = f_j/\sqrt{2\pi}$ , see Eq. (4.4). Even simpler solutions can be assumed, where  $f_1 = f_2 = 1/\sqrt{2}$ , which stand for condensates that are miscible and homogeneous, where the solutions in Eq. (4.4) can be written as

$$\psi_j = a_0 \exp(-i\mu_j t), \quad (4.9)$$

with  $a_0 = 1/\sqrt{4\pi}$ . We can perform a stability study and track how long this simple solution is the ground-state of the system.

### 4.2.1 Stability

We consider small amplitude fluctuations around the homogeneous stationary states in Eq. (4.9), and we suppose fluctuations carried out by an angular dependence given by spherical harmonics  $Y_{\ell,m}(\theta, \phi)$  [24]. This assumption is related on the fact that the solutions of the linear problem (no interaction) are eigenvalues of the angular momentum operator. The perturbed functions are

$$\psi_j(\theta, \phi, t) = [a_0 + u_{j,\ell} Y_{\ell,m}(\theta, \phi) e^{-i\omega t} + v_{j,\ell}^* Y_{\ell,m}^*(\theta, \phi) e^{i\omega^* t}] e^{-i\mu_j t}, \quad (4.10)$$

with  $j = 1, 2$ . The BdG matrix (2.30) for the mixture becomes

$$\mathbf{M} = \begin{pmatrix} D_1 & \gamma_{11} a_0^2 & \gamma_{12} a_0^2 & \gamma_{12} a_0^2 \\ -\gamma_{11} a_0^2 & -D_1 & -\gamma_{12} a_0^2 & -\gamma_{12} a_0^2 \\ \gamma_{21} a_0^2 & \gamma_{21} a_0^2 & D_2 & \gamma_{22} a_0^2 \\ -\gamma_{21} a_0^2 & -\gamma_{21} a_0^2 & -\gamma_{22} a_0^2 & -D_2 \end{pmatrix}, \quad (4.11)$$

with

$$D_j = \epsilon_\ell - \mu_j + (2\gamma_{jj} + \gamma_{kj}) a_0^2, \quad (4.12)$$

where  $j, k = 1, 2$  ( $k \neq j$ ) and  $\epsilon_\ell = \ell(\ell + 1)/2$ , since we have the properties  $\nabla_{\theta,\phi}^2 Y_{\ell,m} = \ell(\ell + 1) Y_{\ell,m}$  and  $\mu_j = (\gamma_{jj} + \gamma_{jk}) a_0^2$ . The diagonalization of this matrix returns the eigenvalues

$$\omega_{\ell,\pm}^2 = \epsilon_\ell \left[ \epsilon_\ell + a_0^2 \left( \gamma_{11} + \gamma_{22} \pm \sqrt{(\gamma_{11} - \gamma_{22})^2 + 4\gamma_{12}\gamma_{21}} \right) \right]. \quad (4.13)$$

If we consider  $\gamma_{11} = \gamma_{22}$  and  $\gamma_{21} = \gamma_{12}$ , we get

$$\omega_{\ell,\pm}^2 = \epsilon_\ell \left[ \epsilon_\ell + 2a_0^2 (\gamma_{11} \pm |\gamma_{12}|) \right], \quad (4.14)$$

for which we have complex solutions when  $\omega_{\ell,\pm}^2 < 0$ , i.e, when the inter-species interaction is

$$|\gamma_{12}| > \gamma_{11} + \frac{\epsilon_\ell}{2a_0^2}. \quad (4.15)$$



Then, the spectrum of the system has a nonzero imaginary part, and the system becomes dynamically unstable.

In Fig. 4.1, we present a modes diagram based on the analytical result in Eq. 4.15. We observe that the angular modes grow depending on the interacting parameters. Since the first mode appears, the homogeneous (miscible) solutions are no longer stable, which means that these interaction parameters favor inhomogeneous (immiscible) solutions. But in the unstable region, we can have more than one mode acting on the system. In this figure, we observe the first three  $\ell = 1, 2,$  and  $3$ . A more

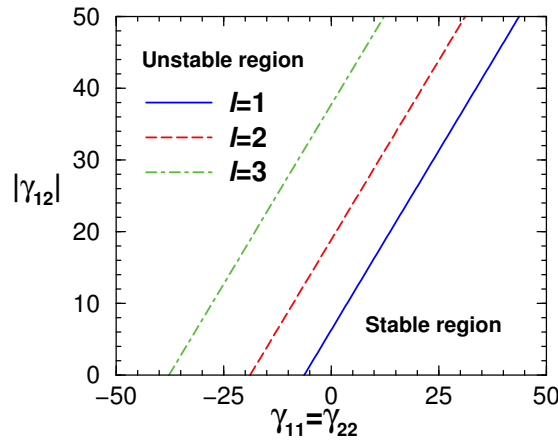


Figure 4.1: Modes diagram for homogeneous ( $s_1 = s_2 = 0$ ) solutions depending on the interactions  $\gamma_{12}$  versus  $\gamma_{11} = \gamma_{22}$ , following the Eq. (4.15). Stable regions stand for parameters for which no mode has imaginary part higher than zero. The lines presents when the unstable modes  $\ell = 1, 2,$  and  $3$  emerge. From [18].

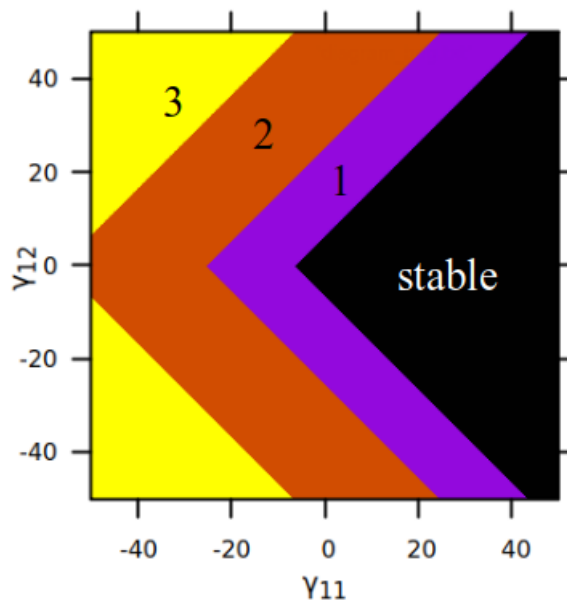


Figure 4.2: Stability diagram for homogeneous solutions as a function of intra- and inters-species  $\gamma_{11}$  and  $\gamma_{12}$ , respectively, see Eq. (4.15). Black spaces stand for stable regions. Violet, orange and yellow places refer to unstable regions where the dominant mode is  $\ell = 1, 2,$  and  $3$ , respectively. From [18].

general diagram can be displayed by observing the modes that exhibit the highest

imaginary spectrum for a specific set of parameters. In Fig. 4.2, we present the dominant unstable modes as a function of the intra- and inter-species interaction. In order to enhance our understanding of how an unstable mode overcome the others, we can see the explicit imaginary spectrum of all of modes. In Fig. 4.3, we present the competition of the unstable angular modes and the critical values of  $\gamma_{12}$  needed to turn on a specific angular mode  $\ell$ . When we have the fixed parameter  $\gamma_{11} = 10$ , the critical values for  $\ell = 1, 2, 3$ , and 4 are  $\gamma_{12} \approx 16.28, 28.85, 47.70$  and  $72.84$ , respectively, as we can see in Eq. (4.15) [18]. These analytical predictions are presented in Fig. 4.2. This can be verified in Eq. (4.14). A fifth mode does not appear because the critical  $g_{12}$  is out of our range, see (4.15). To access the mode  $\ell = 5$  we need an inter-species interaction  $\gamma_{12} \approx 104.25$ .

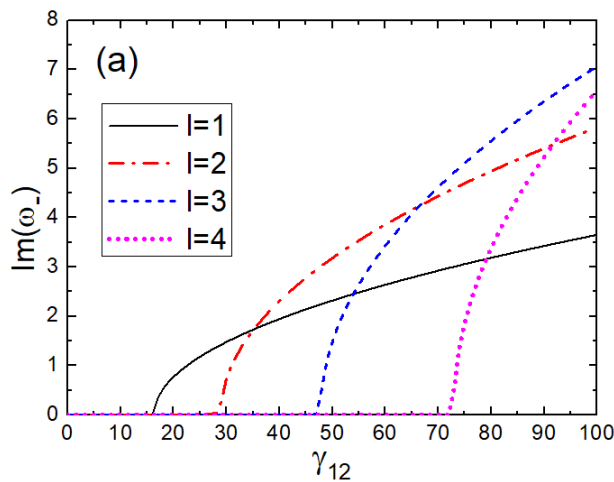


Figure 4.3: Imaginary spectrum of modes  $\ell = 1, 2, 3$ , and 4 as functions of the inter-species interaction  $\gamma_{12}$ , based on analytical unstable frequencies, see Eq.(4.14). The intra-species interactions are fixed in  $\gamma_{11} = \gamma_{22} = 10$ .

The unstable regions pointed out by the angular unstable modes growth are regions where the miscible solutions are not longer favored by the interaction parameters. In Fig. 4.4, we handle an numeric imaginary-time evolution where we let the functions free to find the appropriated solutions, i.e, the ground states, by the setting inhomogeneous ansatz with  $f_1(\theta) \neq f_2(\theta)$  in the GP Eqs. (4.5), in which we consider a spatial grid with  $N_\theta = 201$  points, see the methods appendix sections A.1 and A.3 for more details. We see the densities  $|f_j(\theta)|^2$  of the system going from a miscible homogeneous initial solution, where  $|f_j(\theta)|^2 = 1/2$ , to an immiscible inhomogeneous one, following the predicted pattern found by the analytical and numerical diagonalizations of the BdG matrices. When the inter-species interaction is strongly repulsive the species favor an inhomogeneous solutions with a very low overlap (see Eq. (2.24)) between them. Following the solutions path from homogeneous solutions to inhomogeneous ones, we show in Fig. 4.5 the corresponding density waves  $|\psi_j(\theta, \phi)|^2$ , for the same parameters of Fig. 4.4, where we can see how the species are distributed along the spherical shell. For zero, or low interactions the

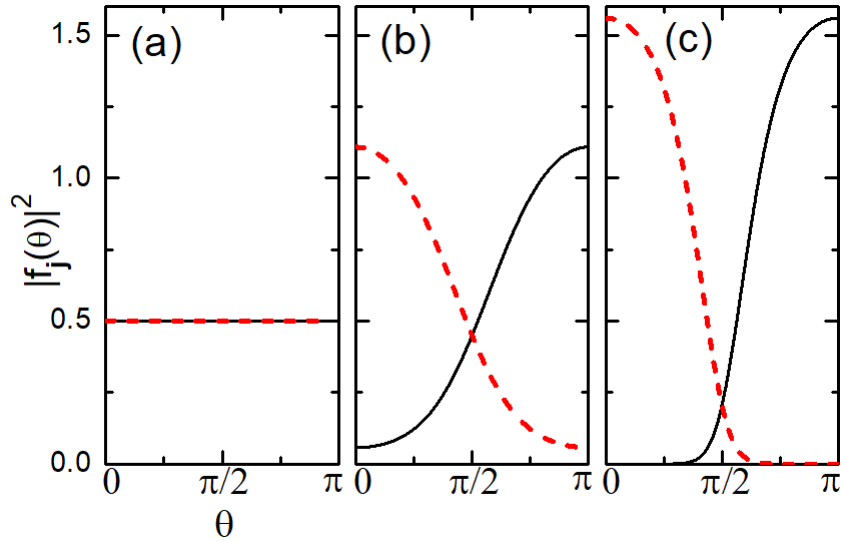


Figure 4.4: Pattern of  $|f_j(\theta)|^2$ ,  $j = 1, 2$  when the system goes from the miscibility to the immiscibility, for fixed  $\gamma_{11} = 10$  when the inter-species interaction increases. (a)  $\gamma_{12} = 10$  and  $\Lambda = 1$ . (b)  $\gamma_{12} = 20$  and  $\Lambda = 0.17$ . (c)  $\gamma_{12} = 100$  and  $\Lambda = 0.00$ . Solid-black line refers to the species 1, and red-dashed line to the species 2. From the author.

species can occupy the whole sphere, and the densities are given by the constant  $|\psi_1|^2 = |\psi_2|^2 = a_0^2 = 1/4\pi$ . When the inter-species interaction is repulsive enough, the species are localized like two bowls. On the other hand, a weak, or intermediary attractive inter-species interaction makes the system remains as a homogeneous solution, but a strong attractive inter-species interaction drives the system to the collapse.

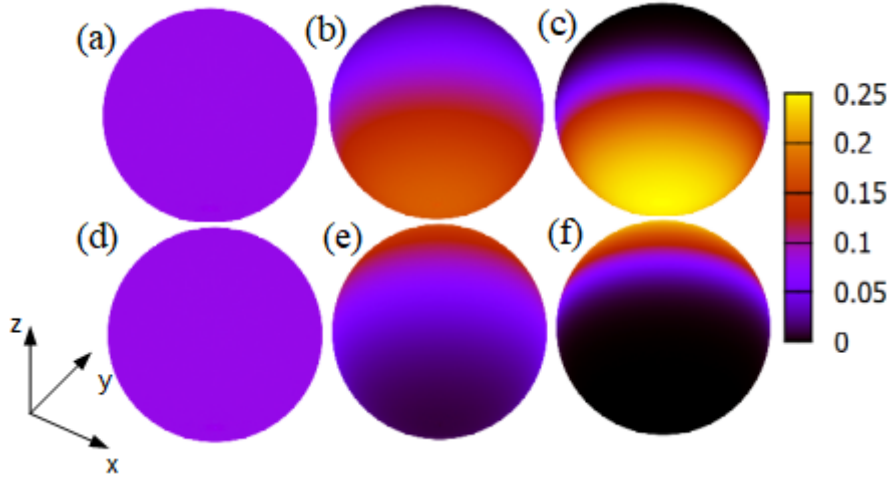


Figure 4.5: Density wave patterns  $|\psi_j(\theta, \phi)|^2$ ,  $j = 1, 2$ , with (a), (b), and (c) following the parameters of (a), (b) and (c) from Fig. 4.4 for species 1. And (d), (e), and (f) corresponding to the species 2. Low density regions are darker and higher density regions are lighter. Note the pole  $\theta = 0$  is localized on the top of the spheres, and  $\theta = \pi$  at the bottom. From the author.

### 4.3 Hidden-vorticity system

Now we consider the more general case where the system has hidden-vorticity, i.e.,  $s > 0$ . On the poles of the spherical shell arise quantized vortices, then the solutions are inhomogeneous, and we can not obtain an analytical prediction for dynamic stability like before.

#### 4.3.1 Variational approximation

A first approach to study the solutions in the HV regime can be a variational treatment. We set  $s_1 = -s_2 = 1$ , which correspond to the  $\ell = 1$  spherical harmonics solutions in the non-interaction problem (linear Schrödinger equation). Then the solutions are proportional to  $\sin \theta$ , and in a preliminary analysis, we can suppose that when the interaction is turned on the solution goes with a power  $\beta$  of  $\sin \theta$ , i.e.,

$$f_v^2(\theta) = \lambda \sin^\beta \theta, \quad (4.16)$$

where  $\beta$  is a variational parameter and  $\lambda$  a normalization constant. We propose initially miscible solutions  $\psi_2 = \psi_1 = f_v/\sqrt{2\pi}$ . When the interaction is turned off, the solution is exact and corresponds to  $\beta = 1$  and  $\lambda = \sqrt{3/4}$ . The normalization condition is

$$\int_0^{2\pi} d\phi \int_0^\pi d\theta \sin \theta \psi_v^2(\theta) = \lambda \int d\theta \sin \theta \sin^\beta \theta = \lambda J(\beta) = 1, \quad (4.17)$$

where we define the integral function  $J(\beta)$ , that obeys the property

$$J(\beta) = \frac{\beta}{\beta + 1} J(\beta - 2), \quad (4.18)$$

which can be written in terms of the *Wallis' integrals*  $W_n$  [70]

$$W_n = \int_0^{\pi/2} d\theta \sin^n \theta, \quad (4.19)$$

for an integer  $n$ . Then, we write  $J(\beta) = 2W_{\beta+1}$ . That function can be rewritten with gamma functions  $\Gamma(n) = (n-1)!$  [71], and it is extended to real arguments  $\beta$

$$J(\beta) = 2W_{\beta+1} = \frac{\sqrt{\pi} \Gamma(\frac{\beta+2}{2})}{\Gamma(\frac{\beta+1}{2} + 1)}. \quad (4.20)$$

Therefore, with the variational solution we are able to approximate the energy (4.7)

$$E(\gamma, \beta) = \frac{(\beta + 2)^2}{8\beta} + \frac{\gamma}{8\pi} \frac{(\beta + 1)^2}{\Gamma(2\beta + 2)} \left[ \frac{\Gamma(\beta + 1)}{\Gamma(\frac{\beta}{2} + 1)} \right]^2, \quad (4.21)$$

where we define  $\gamma = \gamma_{11} + \gamma_{12}$ , and effectively, we have a single species problem. We find the variational parameter  $\beta$  that minimizes the energy functional  $E(\gamma, \beta)$ . We get the variational energy  $E_{var}(\beta)$ , and the corresponding variational chemical potential

$$\mu_{var}(\beta) = 2E_{var}(\beta) - \frac{(\beta + 2)^2}{8\beta}. \quad (4.22)$$

When the interactions are negative ( $\gamma < 0$ ), the parameter  $\beta$  grows, then in the regime of  $\beta \gg 1$ , i.e, a strong negative interaction, we can use the *Stirling's formula*  $\Gamma(z + 1) \approx \sqrt{2\pi z}(z/e)^z$  [71], this is an asymptotic limit, where the energy is

$$E_{asy}(\gamma, \beta) \approx \frac{\beta}{8} - \frac{|\gamma|}{8\pi} \sqrt{\frac{\beta}{\pi}}, \quad (4.23)$$

which can be minimized, thus we get the variational parameter  $\beta_{min} = |\gamma|^2/(4\pi^3)$ , and the energy goes asymptotically with  $-\beta_{min}/8$ . We can write the variational energy and chemical potential in terms of  $\gamma$

$$E_{asy,var}(\gamma) \approx -\frac{|\gamma|^2}{32\pi^3}, \quad \mu_{asy,var}(\gamma) \approx -\frac{3|\gamma|^2}{32\pi^3}, \quad (4.24)$$

with the variational density going to a Dirac-delta function localized at  $\pi/2$  when  $\beta \rightarrow \infty$ . In Fig. 4.6a, we present the comparison between the parameter  $\beta$  found by variational and variational-asymptotic  $\beta_{min}$  approximations. While in Fig. 4.6b, we see the numerical chemical potential given by Eq. (4.6) and energy of Eq. (4.7). In the attractive regime, the comparison with the variational and asymptotic-variational energies found by Eqs. (4.21), (4.22), and (4.24). For strongly attractive interac-

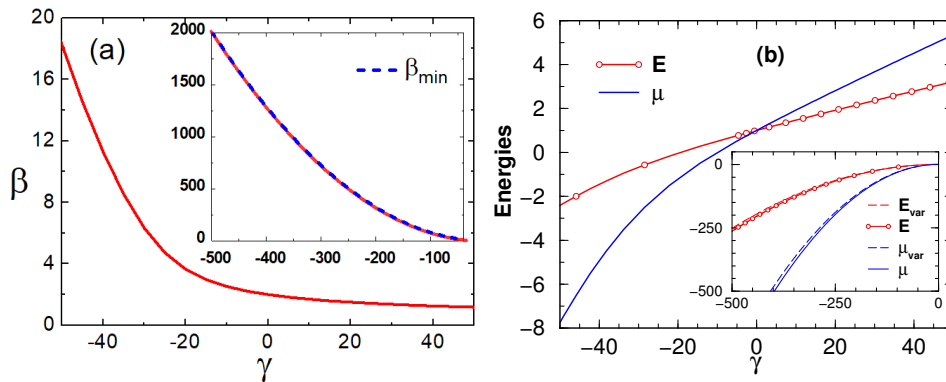


Figure 4.6: Variational quantities in terms of the interaction parameter  $\gamma$ . (a) Minimization variational parameter  $\beta$  where the solid-red line is the variational parameter and the blue-dashed line is the asymptotic approximation. (b) Comparison between variational and exact-numerical results for the energies and chemical potentials. Solid-red line with circles and the blue-solid line are the numerical energy and chemical potential, respectively. The dashed-red and dashed-blue lines are the corresponding quantities by variational approximation. From [18].

tions, the variational and asymptotic approaches are in good agreement with the numerical results. In this regime, the parameter  $\beta$  increases to a high value, but for

repulsive interactions  $\beta \rightarrow 0$ , since effectively we have a single species problem, thus high interactions lead to a quasi-homogeneous system. The boundary conditions prevent the fully homogeneous distribution because the solution goes to zero at the boundaries (poles), the region where the vortices are localized. The Fig. 4.7a shows the numerical and variational pattern of  $|f(\theta)|^2$  as a function of the interaction parameters, making clear how the repulsive interactions lead the system to a quasi-homogeneous solution, and attractive interaction leads to a Dirac-delta function localized at  $\theta = \pi/2$ , the equator of the sphere. The variational approximation captures the behavior of the function, but it does not return a good agreement with numerical results, as the variational energy does. In Fig. 4.7b, we see the maximum density as a response to the interaction parameter, and again the variational approach is a good approximation to predict the general behavior of the function, but not its absolute values. And that is the limitation of the variational tool.

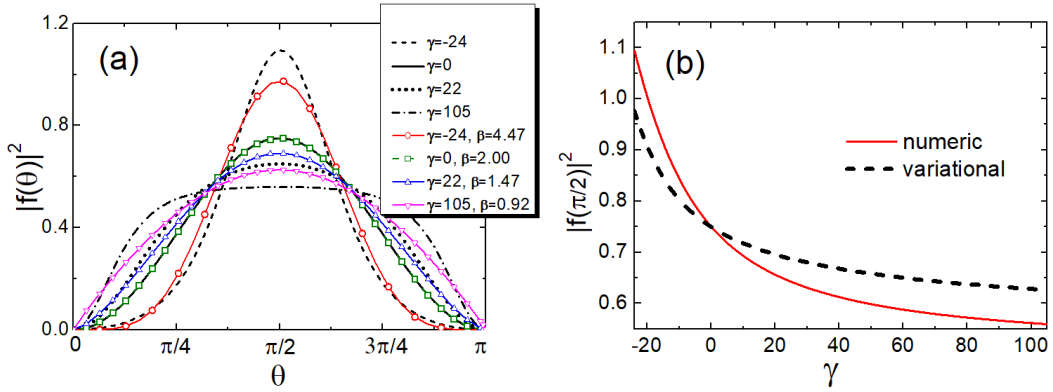


Figure 4.7: Numerical and Variational results (with  $\beta$  indicated) for  $|f|^2$ . (a) The quantity is shown as a function of  $\theta$ . (b) Is presented the maximum values ( $\theta = \pi/2$ ) as function of  $\gamma$ . From [18].

### 4.3.2 Stability

We consider the fluctuations around the stationary input states. We can write the small amplitude oscillations in an angular basis, with an explicit azimuthal  $\phi$  - dependence regarding a phase with quantum number  $m$

$$u_{j,m} = u_{j,m}(\theta)e^{im\phi}, \quad v_{j,m} = v_{j,m}(\theta)e^{im\phi}, \quad (4.25)$$

and we get

$$\psi_j(\theta, \phi, t) = \left[ \frac{f_j(\theta)}{\sqrt{2\pi}} + u_{j,m}(\theta)e^{im\phi}e^{-i\omega t} + v_{j,m}^*(\theta)e^{-im\phi}e^{i\omega^* t} \right] e^{i(s_j\phi - \mu_j t)}, \quad (4.26)$$

with  $j = 1, 2$ . The BdG matrix, as Eq. (2.30) is

$$\mathbf{M} = \begin{pmatrix} \hat{D}_1^+ & \tilde{\gamma}_{11}f_1^2 & \tilde{\gamma}_{12}f_1f_2 & \tilde{\gamma}_{12}f_1f_2 \\ -\tilde{\gamma}_{11}f_1^2 & -\hat{D}_1^- & -\tilde{\gamma}_{12}f_1f_2 & -\tilde{\gamma}_{12}f_1f_2 \\ \tilde{\gamma}_{21}f_1f_2 & \tilde{\gamma}_{21}f_1f_2 & \hat{D}_2^+ & \tilde{\gamma}_{22}f_2^2 \\ -\tilde{\gamma}_{21}f_1f_2 & -\tilde{\gamma}_{21}f_1f_2 & -\tilde{\gamma}_{22}f_2^2 & -\hat{D}_2^- \end{pmatrix}, \quad (4.27)$$

with  $\tilde{\gamma}_{jk} = \gamma_{jk}/2\pi$ ,  $j, k = 1, 2$ , and

$$D_j^\pm = -\frac{1}{2} \frac{1}{\sin \theta} \frac{\partial}{\partial \theta} \left( \sin \theta \frac{\partial}{\partial \theta} \right) + \frac{1}{2} \frac{1}{\sin^2 \theta} (m \pm s_j)^2 + \frac{1}{2\pi} (2\gamma_{jj} f_j^2 + \gamma_{jk} f_k^2) - \mu_j, \quad (4.28)$$

or

$$D_j^\pm = -\frac{1}{2} \frac{\partial^2}{\partial \theta^2} - \frac{1}{2} \cot \theta \frac{\partial}{\partial \theta} + \frac{1}{2} \frac{1}{\sin^2 \theta} (m \pm s_j)^2 + \frac{1}{2\pi} (2\gamma_{jj} f_j^2 + \gamma_{jk} f_k^2) - \mu_j, \quad (4.29)$$

where  $j, k = 1, 2$  and  $k \neq j$ .

We focus on the study of how unstable angular modes influence the system once we set an initial miscible system with  $f_1(\theta) = f_2(\theta) = f(\theta)$ , where both states have unitary vortex charge, with  $s_1 = -s_2 = 1$ . The vortex imposes an inhomogeneous solution for which we can not afford an analytical solution. We found the ground state by performing an imaginary-time evolution described in the appendix sections A.1 and A.3, write the matrix (4.27) by finite differences method described in the appendix section A.4. We numerically diagonalize the matrix by the routine ZGEEV from Lapack library available in the compiler of Intel Fortran. For this task we use a spatial grid of  $N_\theta = 201$  points. The spectrum we get provides information about the dynamic stability even in regions where the mixture are miscible. We highlight that for repulsive interactions, the unstable modes are related on the immiscible phase solutions. However, for attractive interactions the solutions are always miscible, but can be unstable anyway. In Fig. 4.8, we present a stability diagram as a function of the interaction parameters  $\gamma_{11} = \gamma_{22}$  and  $\gamma_{12} = \gamma_{21}$ . We see a stable region indexed by 's', and unstable ones labeled by the number of the dominant angular mode  $m$  at this region. Once we get the BdG spectrum of the system, we are able to figure out which mode is the largest one in a particular region. The stable region is more likely in the repulsive region ( $\gamma_{11} + \gamma_{12} \geq 0$ ), but we have a small region of stability in the overall attractive region, which is not expected by a naive assumption that the stability is always guaranteed when miscibility is present. While the attractive region is exhibits miscibility, it's remarkable that the number of unstable modes grows in proportion to the magnitude of the interaction. On the other hand, the repulsive region seems to show a correspondence with miscibility properties.

In Fig. 4.9, we present the competition of the angular modes for specific cases into the previous diagram in Fig. 4.8. We set a fixed intra-species interaction  $\gamma_{11} = 10$  and observe the spectrum as a function of the inter-species interaction  $\gamma_{12}$  in Fig. 4.9a. And in Fig. 4.9b, we observe the case of no interaction between different species ( $\gamma_{12} = 0$ ), and we see that the attractive region is likely to be unstable even without the influence of the other species.

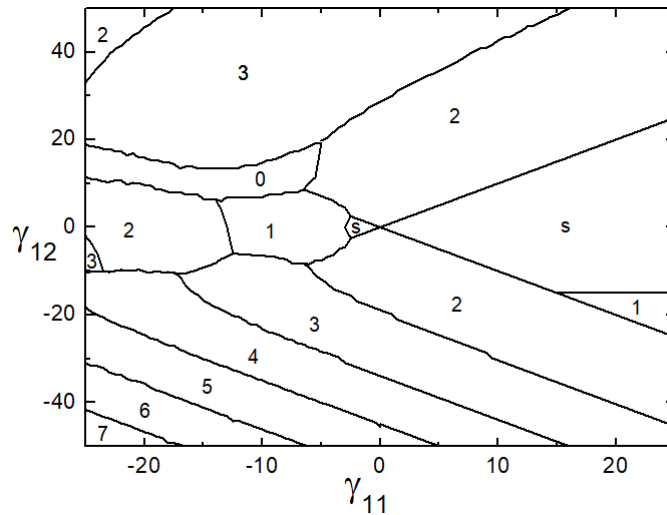


Figure 4.8: Stability diagram for hidden vorticity solutions ( $s_1 = -s_2 = 1$ ) displayed as a function of the interactions parameters  $\gamma_{12}$  versus  $\gamma_{11} = \gamma_{22}$ , obtained by the diagonalization of Eq. (4.27). The index 's' refers to the stable region and the numbers present the modes  $m = 0, \dots, 7$ , which are dominant in that unstable regions. From the author.

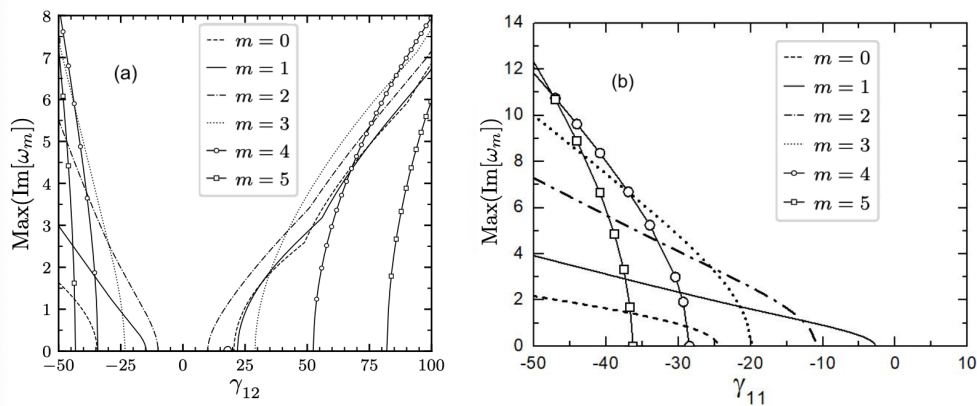


Figure 4.9: Maximum imaginary BdG spectrum  $\text{Im}(\omega)$  returned by diagonalization of (4.27) as a function of the interaction parameters, driven by the excitation modes  $m = 0, \dots, 5$ . (a) Spectrum when  $\gamma_{11} = 10$  is fixed. (b) Spectrum when  $\gamma_{12} = 0$  is fixed. From [18].

### 4.3.3 Dynamics

We set initial conditions where the wave functions are given by  $\psi_j = f(\theta)e^{is_j\phi}/\sqrt{2\pi}$ , and carry out a time-dependent evolution of the 2D GP equation (4.1) with the full Laplacian  $\nabla_{\theta,\phi}^2$  (4.2), and no additional approximations. We perform the numeric calculations with a spatial grid where  $N_\theta = 201$  and  $N_\phi = 401$ , with spatial steps  $d\theta = \pi/N_\theta$  and  $d\phi = 2\pi/N_\phi$ . The dynamics is observed with a time-step  $dt = 0.0005$ . We choose an initial state for which the interaction parameters are  $\gamma_{11} = 10$  and  $\gamma_{12} = 12$ , we can have better picture of this state in the Fig. 4.10. As higher the interactions are, more the vortex core becomes smaller and the cloud around it homogeneous. For this same initial states, we show in Fig. 4.11, how evolve the angular momentum in the direction  $z$  and the overlap between the species. For which we have BdG semi-analytical predictions in Fig. 4.8 and Fig. 4.9a, which



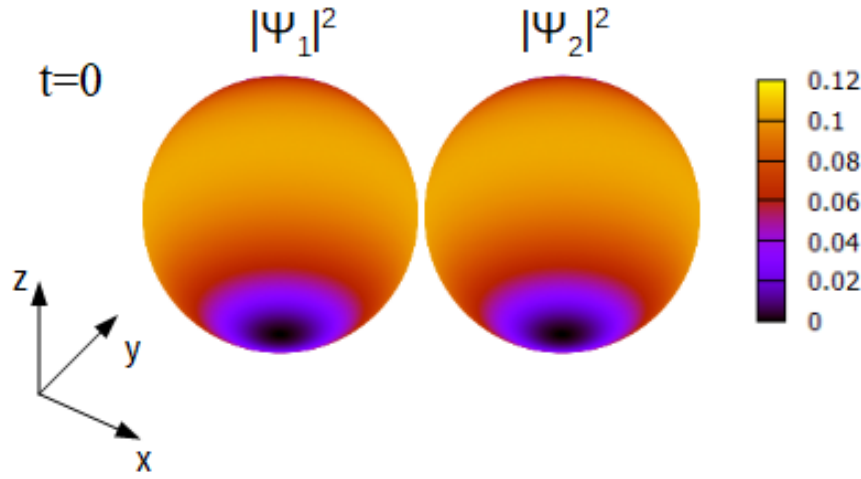


Figure 4.10: Ansatz for both species at the time  $t = 0$  when we have the parameters  $\gamma_{11} = 10$  and  $\gamma_{12} = 12$ , and vortex charges  $s_1 = -s_2 = 1$ , see Eq. (4.4). Note that each species has a vortex-antivortex pair. At this perspective, we only can see the bottom vortices, but also have the top ones. Unfortunately, we can not see all vortex in only one 2D picture. From the author.

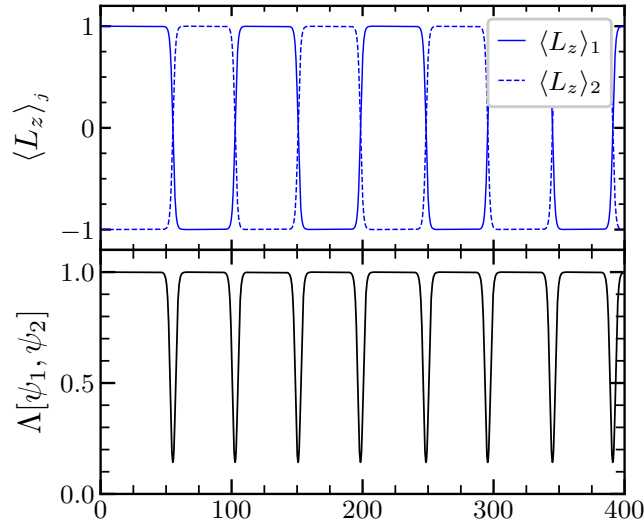


Figure 4.11: Properties dynamics of the unstable case where parameters are  $\gamma_{11} = 10$  and  $\gamma_{12} = 12$ . (a) Average angular momentum  $\langle L_z \rangle_j$ , see Eq.(4.8). (b) Overlap  $\Lambda(t)$  evolution in time, see Eq.(2.24). From [18].

have shown that the at this chosen parameters, the system is unstable and driven by the dominant angular mode  $\ell = 2$ . Indeed, we note that by the time  $t = 48$ , the species are no longer miscible. And particularly, the species enter a regime where they exchange angular momentum between each other every time they collapse and revive in such a way the current persist. For this special case, we can see a periodic behavior which is not what happens for every choice of parameters. Another way to see how the unstable mode take over the dynamics is to observe the density clouds for both species, as we display in Fig. 4.12. The previous theory is confirmed, since Fig. 4.12 shows the densities are broken into 2 pieces, as an inherent behavior of states led by the unstable mode  $\ell = 2$ . This dynamic periodic phenomenon is found in several examples in our work [18]. When the angular unstable mode is not destructive enough, it drives the system to a periodic regime where it breaks into  $\ell$  pieces and later returns to the same initial pattern. However, we point out that, if we

have several unstable modes simultaneously driving the dynamics, the interfere with each other and the system can not afford a periodic behavior.

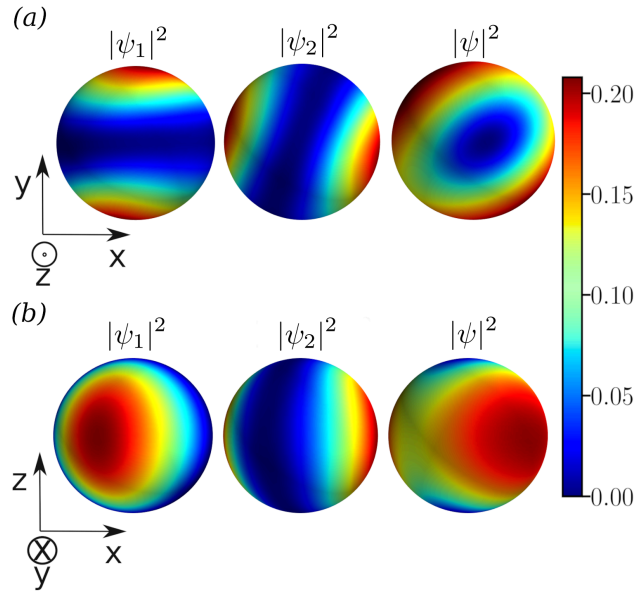


Figure 4.12: Densities of species 1, 2 and the sum them (from left to right) at the time  $t = 55$  when  $\gamma_{11} = 10$  and  $\gamma_{12} = 12$ , same case of Fig. 4.11. Row (a) presents the spheres with z-direction pointing outwards the page. And row (b) presents the spheres with y-direction pointing inwards the page. From [18].

## 4.4 Conclusions

With our results, we have shown that the mixture on the spherical shell provides a rich scenario to study the stability. The particular geometry of a sphere provide a very special framework with a discrete spectrum, where we can track which of the modes are actually taking over the dynamics of the system. We have performed accurate predictions about the stability behavior of the system with a one-dimensional BdG model, and confirmed our predictions by carrying out a dynamics simulation.

The main result of our model is to reveal that vortex states can be dynamically stable on the surface of a sphere, which was an open question, once in the literature we have solid evidences that vortices are energetically unstable [57]. Here we have presented results that support that these states can be stable once the condensate do not interact with a thermal cloud. We have observed that the spherical geometry, like the annulus ones, is able to afford persistent currents. A mixture can achieve a very interesting behavior of collapse and revival, already observed in the context of gases confined in optical lattices [72]. But here, we have presented another context were this phenomenon can be observed in future experiments.

In this work, we had overcome the challenges related to very coordinate system. When we handle numerical calculations in spherical coordinates, we have to deal with several trick problems related to singularities. Furthermore, we observed that,

in these coordinates, conventional finite differences methods often yield unreliable results. Therefore, we have developed a novel pseudo-spectral method, which, to the best of our knowledge was not already available in literature. With our methods, we set our research group a step ahead another theoretical groups currently handling problem of condensates in the bubble.

## Chapter 5

# Faraday Waves on Mixtures Driven by Rabi Coupling

We can observe spatial pattern formations in several branches of physics [73], it was first reported by Michael Faraday in his famous experiments in 1831 [74], at that time regarding spatial patterns on liquids inside a vibrating receptacle. Currently, we call *Faraday waves* the surface excitations that emerge over a flat surface of a fluid. These phenomena are also important in nonlinear waves, out-of-equilibrium fluid mechanics, and nonlinear optics. In the last three decades, the advance in cooling and trapping techniques has enabled the feasibility of Bose-Einstein condensates in ultracold gases. In this context, it is possible to control the particle s-wave interactions and shape of the condensate, even in low dimensions. This environment has opened new ways to explore and investigate how classical mechanics fluid phenomena can be observed in quantum fluids. In atomic gases, spatial patterns can be performed by parametric modulations in the scattering length or trap potential. Regarding this subject, some ways to experimentally and theoretically observe the emergence of Faraday waves have been reported [75–79]. Time-dependent modulations in the trap potential or the scattering length are able to drive systems to target excited states [20], induce time-crystal formation [80], and manipulate the population dynamics [81, 82]. A novel approach to induce Faraday waves without the need for parameter modulation within the trap or interactions is by performing Rabi coupling between a mixture of condensates [27, 83]. In this method, the effective time-dependent interaction energy plays an important role in driving the dynamics. In addition, there is already evidence that an effective time-dependent interaction also can be performed by Raman-induced spin-orbit coupling [28]. It suggests that we have some advantages if we deal with condensate mixtures for triggering of parametric resonance. Moreover, not only the spatial pattern can be induced, but also new features can be observed, once intra- and inter-species interactions are able to drive the system to phase separation. Currently, condensate mixtures can be performed with the same atomic species initially set into different hyperfine states [84], but also can be handled with different atomic species [85]. It is possible to observe

how the elementary excitations can grow and induce phase separation depending on the interaction parameters [18, 69]. An open question is how Faraday waves can be achieved in closed geometries, where we have a discrete spectrum, and we need very especial conditions to accomplish parametric resonance. The recent experiments performed with ultracold gases aboard the International Space Station as well as the Earth-based experiment with mixtures [32, 33], make us very confident that our results are relevant for cold atom physics. Our findings will be available in a preprint version soon [19].

In this chapter, we aim to study the stability of spatially-homogeneous time-periodic states in Bose-Einstein binary mixtures confined on the surface of a spherical bubble, inspired by the recent work [27], where homogeneous mixtures are handled into Rabi oscillations in order to give rise to Faraday waves. The authors observed that spatial patterns coexist with the immiscible separation phase of the mixture. We manage a similar study, but in our environment the spherically closed geometry provides a discrete spectrum, in such a way that we have to tune different parameters of the system to give rise to parametric resonance. Since this kind of setup presents a novelty in promoting Faraday waves without any external modulation in the interactions or the trap, we can highlight that another interesting feature of this system is the possibility of triggering Faraday waves without energy injection. The Faraday waves are excited just by tuning the Rabi oscillation frequency in resonance with the small-amplitude fluctuations around the periodic state. Here we observe that the same unstable angular modes which break the condensate into pieces, as observed in the previous chapter 4, are also able to induce Faraday-patterns excitations. We study the dynamics stability by carrying out linearized GP equations for the fluctuations, based on Bogoliubov-de Gennes method for stationary states, and also a suitable stability method for periodic states provided by the Floquet theory. For small interactions we can figure out the resonance conditions and its relation with the Floquet spectrum. We perform full GP simulations to check the stability predictions, and we find pretty good agreement between Floquet diagrams and the full dynamics simulations. Our results are relevant to the recent development of condensates in microgravity environments, once we bring up how the Rabi coupling can drive the stability of boson-boson mixtures performed with different hyperfine states of the same atomic gas, where conversion between the states is likely to happen.

The remainder of this chapter is organized as follows. In section 5.1, we present a model for gases driven by fields that promote Rabi oscillations. Next, in Sec. 5.2, we introduce the Gross-Pitaevskii model to study both contact-noninteracting and -interacting condensed mixtures in the dynamic periodic regime. In Sec. 5.3, we handle a BdG stationary model to study stability of our system, which is followed by a suitable model depicted in Sec. 5.4, which is based on Floquet theory to correctly analyze dynamic stability of periodic states. The Sec. 5.5 stands for simulations

of the dynamics by considering the 2D GP equations with all terms, and observe in which way the initial states are affected by unstable modes. In Sec. 5.6, all methods regarding stability predictions and the full GP calculations are compared in such a way we can have a better picture of the regimes where analytical predictions are valid, and which of the methods provide reliable results. Finally, in the conclusion Sec. 5.7, we provide our main results and major insights supported by the results of this work.

## 5.1 Mixtures driven by Rabi oscillations

We consider a mass-balanced mixture of two atomic hyperfine states confined by different potentials  $V_1$  and  $V_2$ . The achieved states have a hyperfine splitting  $V_{hf}$  in the absence of interactions. The coupling drive can be characterized by an oscillating radiofrequency (rf) field tuned with frequency  $\omega_{rf}$ , for which the physics of interest can be described in a pair of GP equations [66]

$$\begin{aligned} i\frac{\partial\psi_1}{\partial t} &= \left[ -\frac{1}{2}\nabla^2 + V_1 + g_{11}|\psi_1|^2 + g_{12}|\psi_2|^2 \right] \psi_1 \\ &+ \Omega e^{i\omega_{rf}t} \psi_2, \end{aligned} \quad (5.1a)$$

$$\begin{aligned} i\frac{\partial\psi_2}{\partial t} &= \left[ -\frac{1}{2}\nabla^2 + V_2 + V_{hf} + g_{22}|\psi_2|^2 + g_{21}|\psi_1|^2 \right] \psi_2 \\ &+ \Omega^* e^{-i\omega_{rf}t} \psi_1, \end{aligned} \quad (5.1b)$$

where in general we have a Rabi frequency  $\Omega(t)$ , which can be turned on or turned off, which for simplicity, we consider the situation where the coupling is controlled to be working during all the time of the experiment as a constant term in the GP equations. Hereafter, we consider the Rabi-coupling constant as a real and positive value. We can handle unitary transformations  $\psi_1 = e^{i(\omega_{rf}t/2+\pi/4)}\tilde{\psi}_1$  and  $\psi_2 = e^{-i(\omega_{rf}t/2+\pi/4)}\tilde{\psi}_2$  [8], in order to get a simplified form for GP equations. Once we consider a rf-tuning of  $\omega_{rf}$  equivalent to the hyperfine splitting  $V_{hf} = \hbar\omega_{rf}$  between the states, we get

$$i\frac{\partial\tilde{\psi}_1}{\partial t} = \left[ -\frac{1}{2}\nabla^2 + V + g_{11}|\tilde{\psi}_1|^2 + g_{12}|\tilde{\psi}_2|^2 \right] \tilde{\psi}_1 - i\Omega\tilde{\psi}_2, \quad (5.2a)$$

$$i\frac{\partial\tilde{\psi}_2}{\partial t} = \left[ -\frac{1}{2}\nabla^2 + V + g_{22}|\tilde{\psi}_2|^2 + g_{21}|\tilde{\psi}_1|^2 \right] \tilde{\psi}_2 + i\Omega\tilde{\psi}_1, \quad (5.2b)$$

in which we also have considered both species trapped about the same potential, apart from the hyperfine splitting, i.e,  $V_2 \approx V_1 \approx V$ . From now on, we drop the tildes for convenience.

## 5.2 Model

We assume a mixture managed in such a way the atomic population can oscillate between both condensed states, where the dynamics is drive by the GP equations (5.2a) and (5.2b). We suppose condensates confined by the bubble trap ( $V = V_{trap}$ ), for which we already have derived a dimensional-reduced form in Sec. 3.2. Therefore, our model is described by the two-dimensional GP equations

$$i\frac{\partial\psi_1}{\partial t} = \left[ -\frac{1}{2}\nabla_{\theta,\phi}^2 + g_{11}|\psi_1|^2 + g_{12}|\psi_2|^2 \right] \psi_1 - i\Omega\psi_2, \quad (5.3a)$$

$$i\frac{\partial\psi_2}{\partial t} = \left[ -\frac{1}{2}\nabla_{\theta,\phi}^2 + g_{22}|\psi_2|^2 + g_{21}|\psi_1|^2 \right] \psi_2 + i\Omega\psi_1, \quad (5.3b)$$

for which we are assuming a ideal 2D spherical shell, where the condensates are initially set into a miscible homogeneous configuration. Next, we are going to study how this initial state evolve in time in several kind of particular regimes, where our main goal is to predict the dynamic stability profile.

### 5.2.1 Non-interacting system

We consider a uniform system with no interaction ( $g_{ij} = 0$ ), i.e, we neglect the Laplacian and all interaction in the Eqs. (5.3a) and (5.3b), in such a way we get

$$i\frac{\partial\psi_1}{\partial t} = -i\Omega\psi_2, \quad (5.4a)$$

$$i\frac{\partial\psi_2}{\partial t} = i\Omega\psi_1, \quad (5.4b)$$

which can be written in the matrix form

$$i\frac{\partial}{\partial t} \begin{pmatrix} \psi_1 \\ \psi_2 \end{pmatrix} = \begin{pmatrix} 0 & -i\Omega \\ i\Omega & 0 \end{pmatrix} \begin{pmatrix} \psi_1 \\ \psi_2 \end{pmatrix}, \quad (5.5)$$

or equivalently

$$i\frac{\partial\hat{\psi}}{\partial t} = \Omega\sigma_y\hat{\psi}, \quad (5.6)$$

where  $\sigma_y$  is a Pauli matrix [24] and  $\hat{\psi}$  stand for the species solutions column vector given by

$$\sigma_y = \begin{pmatrix} 0 & -i \\ i & 0 \end{pmatrix}, \quad \hat{\psi} = \begin{pmatrix} \psi_1 \\ \psi_2 \end{pmatrix}. \quad (5.7)$$

The solution of the system (5.6) is

$$\hat{\psi} = \mathbf{R}\hat{\psi}, \quad (5.8)$$

with the evolution operator  $\mathbf{R}(\Omega t)$  given by  $\mathbf{R}(\Omega t) = \exp(-i\Omega\sigma_y t)$ , which can be written as  $\mathbf{R}(\Omega t) = \mathbf{1} \cos(\Omega t) - i\sigma_y \sin(\Omega t)$  [86], where  $\mathbf{1}$  is the identity matrix. Therefore, the column vector  $\hat{\psi}$  evolves like a spin state under a rotation operator through an angle  $\Omega t$ .

$$\begin{pmatrix} \psi_1 \\ \psi_2 \end{pmatrix} = \begin{pmatrix} \cos(\Omega t) & -\sin(\Omega t) \\ \sin(\Omega t) & \cos(\Omega t) \end{pmatrix} \begin{pmatrix} \psi_1 \\ \psi_2 \end{pmatrix}. \quad (5.9)$$

For initial conditions  $\psi_1(t=0) = \psi_2(t=0) = 1/\sqrt{8\pi}$ , where we have half of the total population in each state. From (5.9), the states evolve in time with

$$\psi_1(t) = \frac{\cos(\Omega t) - \sin(\Omega t)}{\sqrt{8\pi}}, \quad (5.10a)$$

$$\psi_2(t) = \frac{\cos(\Omega t) + \sin(\Omega t)}{\sqrt{8\pi}}, \quad (5.10b)$$

which can be written as

$$\psi_1(t) = \frac{1}{\sqrt{4\pi}} \cos(\Omega t + \pi/4), \quad (5.11a)$$

$$\psi_2(t) = \frac{1}{\sqrt{4\pi}} \sin(\Omega t + \pi/4). \quad (5.11b)$$

## 5.2.2 Interacting system

When both interactions and Rabi coupling are important to the system we can have some special kinds of homogeneous solutions: Stationary ones as well as periodic ones. We assume spatial homogeneous solution which are driven by the system of equations

$$i\frac{\partial\psi_1}{\partial t} = \left[ g_{11}|\psi_1|^2 + g_{12}|\psi_2|^2 \right] \psi_1 - i\Omega\psi_2, \quad (5.12a)$$

$$i\frac{\partial\psi_2}{\partial t} = \left[ g_{22}|\psi_2|^2 + g_{21}|\psi_1|^2 \right] \psi_2 + i\Omega\psi_1, \quad (5.12b)$$

for which we can observe the particular solutions. The stationary solution can be written as

$$\psi_1 = \psi_2 = \frac{1}{\sqrt{8\pi}} \exp(-i\mu t), \quad (5.13)$$

with the chemical potential given by  $\mu = (g + g_{12})/(8\pi)$ , for  $g_{21} = g_{12}$  and  $g_{11} = g_{22} = g$ . In the case of periodic solutions, we can have an analytical sinusoidal solution for equal interaction parameters  $g_{12} = g$

$$\psi_1(t) = \frac{1}{\sqrt{4\pi}} \cos(\Omega t + \pi/4) \exp(-i\mu t), \quad (5.14a)$$

$$\psi_2(t) = \frac{1}{\sqrt{4\pi}} \sin(\Omega t + \pi/4) \exp(-i\mu t), \quad (5.14b)$$



with  $\mu = g/(4\pi)$ . A more general solution in the regime  $g_{12} \neq g$  can not be written by means of sinusoidal functions, and actually we have to solve the GP equations numerically. With no loss of generality we can write these solutions as

$$\psi_j(t) = f_j(t)\exp(-i\gamma_j t), \quad (5.15)$$

with  $j = 1, 2$ , where  $f_j$  are complex periodic functions and  $\gamma_j$  are constant real values, in general, different from the chemical potentials. We have  $f_2 \neq f_1$ , but in other hand the constants are about the same  $\gamma_2 = \gamma_1 = \gamma$ .

By considering the more general homogeneous solution (5.15), it can be shown that the period decreases as  $|g - g_{12}|$  increases, with the maximum period occurring when the inter- and intra-species parameters are the same ( $g = g_{12}$ ) [27]. This dependence of the period on the interaction parameters and Rabi frequency was verified numerically and plotted in Fig. 5.1, where it was also verified how the oscillation period decreases as the Rabi coupling increases. To illustrate the density behavior, when considering different Rabi couplings and interactions, we also present two panels in Fig. 5.2. Panel (a) shows the behavior of the densities for the particular cases with  $g_{12} = g$ , when the two components follow the simple analytical expressions (5.14a) and (5.14b). By contrast, panel (b) illustrates the behavior of a more general case with  $g_{12} \neq g$ , according to Eq. (5.15), when the solutions are deviating from the sinusoidal form. For a given Rabi parameter  $\Omega$ , as the differences between the interactions ( $|g - g_{12}|$ ) increase, the number of particles being exchanged (represented by the corresponding amplitudes) decreases, oscillating within a smaller interval.

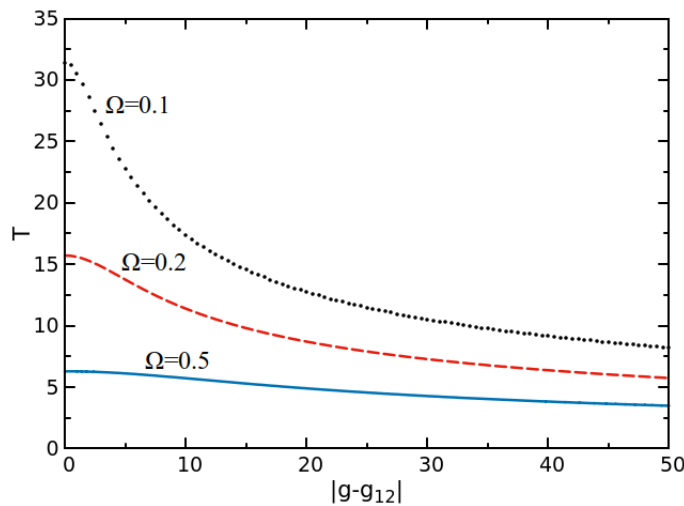


Figure 5.1: (Color online) Density oscillating period  $T$  as a function of the absolute difference of the interaction parameters  $|g - g_{12}|$ . The results stand for different Rabi couplings  $\Omega$ , as indicated. From [19]

With respect to the Rabi frequency  $\Omega$  (larger periods implying lower values of  $\Omega$ ), more time is needed for an oscillating solution to complete each periodic cycle with lower values of  $\Omega$  than for higher ones (shorter period). As pointed out in Fig. 5.2 for the initial time interval, lower frequencies provide almost linear behaviors (increasing or decreasing) with time when compared with the corresponding behavior

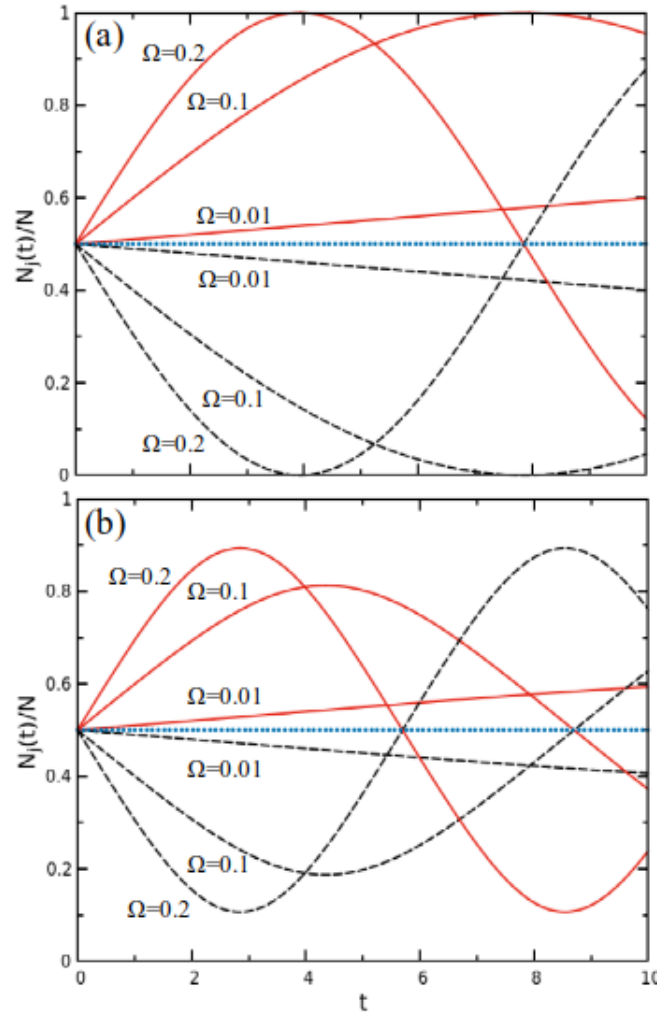


Figure 5.2: (Color online) Time-evolution of the atom-number ratio (normalized densities),  $N_j(t)/N \equiv 4\pi n_j = 4\pi|\psi_j(t)|^2$ , with initial condition  $n_j(0) = 1/2$ , for constant Rabi couplings  $\Omega = 0.01, 0.1$ , and  $0.2$ , where the absolute difference between the interaction parameters are given by  $|g - g_{12}| = 0$  (a) and  $|g - g_{12}| = 10$  (b). In both panels, the black dashed lines refer to species 1 and the red solid lines to species 2, where the horizontal blue dotted line stands for  $\Omega = 0$ .

obtained with higher frequencies. Therefore, at short times, when the Rabi coupling constant is weak ( $\Omega \rightarrow 0$ ), stationary solutions and oscillating ones are likely to be the same. Conversely, this is no longer true when the coupling becomes stronger.

### 5.3 Stability of stationary solutions

The role of the Rabi coupling  $\Omega$  on stationary solutions (5.13) is studied in this section by performing a dynamic stability analysis, using the BdG method [8], see Sec. 2.2. Within this approach, small amplitude oscillations are considered around the uniform stationary solution (5.13). With the perturbations being eigenfunctions of the kinetic energy operator, we can express the perturbed wave functions by  $\ell$ -angular-mode oscillations, in terms of the usual spherical harmonics  $Y_{\ell,m}(\theta, \phi)$ ,

as

$$\psi_{j,\ell}(\theta, \phi, t) = \left[ \frac{1}{\sqrt{8\pi}} + \eta_{j,\ell}(\theta, \phi, t) \right] \exp(-i\mu t), \quad (5.16)$$

where  $\eta_{j,\ell}$  are the angular distribution modes, being expressed in terms of the spherical harmonics  $Y_{\ell,m}(\theta, \phi)$ ,

$$\eta_{j,\ell}(\theta, \phi, t) = u_{j,\ell} Y_{\ell,m}(\theta, \phi) e^{-i\omega_\ell t} + v_{j,\ell}^* Y_{\ell,m}^*(\theta, \phi) e^{i\omega_\ell^* t}, \quad (5.17)$$

where  $u_{j,\ell}$  and  $v_{j,\ell}$  are complex parameters to be determined. The spectral solutions are given by  $\omega_\ell$ , with  $\ell$  being specific angular mode oscillations. Therefore, all the perturbation terms of Eq. (5.16) are exact solutions of the linear part of Eqs. (5.3a) and (5.3b) (apart from the Rabi-coupling term), with eigenvalues  $\epsilon_\ell \equiv \ell(\ell + 1)/2$ . The particular simplified symmetric form of Eq. (5.17) allows us to assume perturbations with no dependence on the azimuthal mode excitation, given by  $m$  (an integer running from  $-\ell$  to  $\ell$ ), which can be arbitrarily chosen. Therefore, in the exponential factors of Eq. (5.17), the frequency parameters  $\omega_\ell$  are excitation modes that carry only the angular momentum index  $\ell$ . They are in general complex numbers, with non-zero imaginary parts when the system becomes dynamically unstable. By initially assuming they are real numbers, we are considering parameters such that the system is in a stable configuration. As we vary these parameters, for some specific modes of oscillation the system becomes unstable, acquiring non-zero imaginary parts.

We insert the perturbed solutions (5.16) into GP Eqs. (5.3a) and (5.3b), and by neglecting the second and higher-order amplitude terms, we obtain the corresponding BdG matrix equation,

$$\mathbf{M}\mathbf{u}_\ell = \omega_\ell \mathbf{u}_\ell, \quad (5.18)$$

where

$$\mathbf{M} = \begin{pmatrix} \epsilon_\ell + \frac{g}{8\pi} & \frac{g}{8\pi} & \frac{g_{12}}{8\pi} - i\Omega & \frac{g_{12}}{8\pi} \\ \frac{g}{8\pi} & \epsilon_\ell + \frac{g}{8\pi} & \frac{g_{12}}{8\pi} & \frac{g_{12}}{8\pi} + i\Omega \\ \frac{g_{12}}{8\pi} + i\Omega & \frac{g_{12}}{8\pi} & \epsilon_\ell + \frac{g}{8\pi} & \frac{g}{8\pi} \\ \frac{g_{12}}{8\pi} & \frac{g_{12}}{8\pi} - i\Omega & \frac{g}{8\pi} & \epsilon_\ell + \frac{g}{8\pi} \end{pmatrix}, \quad (5.19)$$

and  $\mathbf{u}_\ell$  is the column vector that contains the amplitude terms of the two coupled components  $\mathbf{u}_\ell = [u_{1,\ell} \ v_{1,\ell} \ u_{2,\ell} \ v_{2,\ell}]^T$ . We have four possible solutions for each mode  $\ell$  of the frequencies  $\omega_\ell$  given by

$$\omega_{\ell,\pm}^2 = \left( \epsilon_\ell^2 + \frac{\epsilon_\ell g}{4\pi} \right) + \Omega^2 \pm 2\sqrt{\left( \epsilon_\ell^2 + \frac{\epsilon_\ell g}{4\pi} \right) \Omega^2 + \frac{\epsilon_\ell^2 g_{12}^2}{(8\pi)^2}}. \quad (5.20)$$

However, two of them with opposite overall signs are redundant as they correspond to exchanging signals in the original definitions. The system is said to be *dynamically stable* if these frequencies are real:  $\text{Im}(\omega_{\ell,\pm}) = 0$ ; becoming *dynamically*

*unstable* when some of the solutions turns out to be complex:  $\text{Im}(\omega_{\ell,\pm}) \neq 0$ . In Fig. 5.3, we present a BdG stability diagram, which depicts how large is the stable region, when the interactions change. By comparing the panels 5.3a and 5.3b, we are verifying that the strength of the Rabi coupling has an important role in the rise of new regions of stability. To verify how the system is driven for weak and strong coupling regimes, the BdG spectrum is discussed in the next sections 5.3.1 and 5.3.2, by considering extreme regime approximations, with the weak and strong coupling cases given, respectively, by  $\Omega \rightarrow 0$  and  $\Omega \rightarrow \infty$ .

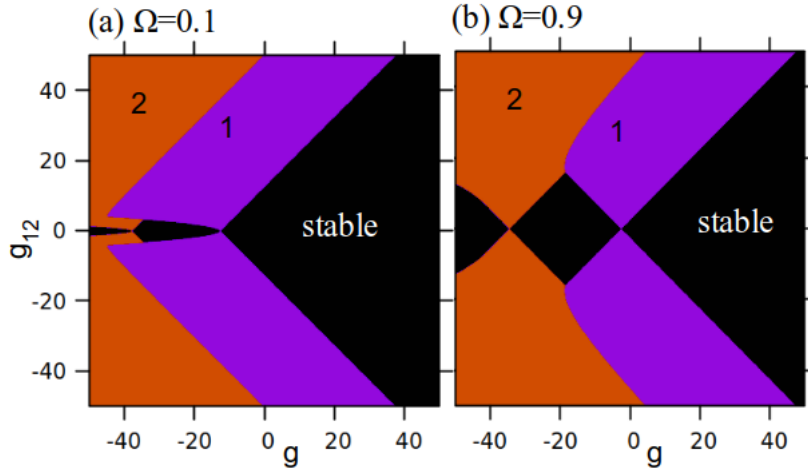


Figure 5.3: (Color on-line) BdG stability diagrams, as given by Eq. (5.20). Black places are stable regions ( $\text{Im}(\omega_{\ell,\pm}) = 0$ ) and the colors provide the dominant unstable angular modes ( $\text{Im}(\omega_{\ell,\pm}) \neq 0$ ). Violet places stand for the unstable angular mode  $\ell = 1$  and orange for  $\ell = 2$ . (a) Rabi coupling constant  $\Omega = 0.1$ . (b)  $\Omega = 0.9$ . From [19].

### 5.3.1 Zero coupling

By considering a zero Rabi coupling constant ( $\Omega = 0$ ), the BdG spectrum (5.20) provides substantially simpler excitation frequencies

$$\omega_{\ell,\pm}^2 = \epsilon_\ell \left[ \epsilon_\ell + \frac{1}{4\pi}(g \pm g_{12}) \right], \quad (5.21)$$

which are supposed to be a good approximation for cases where  $\Omega \ll 1$ , and the system has a period too large ( $T \rightarrow \infty$ ) that the effective system is almost stationary.

### 5.3.2 Strong coupling

We consider the case where the Rabi coupling  $\Omega$  is much larger than any other frequency scales in the system. In this way, there are two time scales in the system, the dynamics driven by interactions and confinement potential, and also the faster dynamics of Rabi oscillations of the internal hyperfine states. We can study the system in the rotating frame, where the slower system dynamics is almost stationary. We

can rewrite our GP equations in the matrix form

$$i \frac{\partial \hat{\psi}}{\partial t} = \hat{H} \hat{\psi}, \quad (5.22)$$

where  $\hat{H} = \hat{H}_{GP} + \Omega \sigma_y$ , with

$$\hat{H}_{GP} = \begin{pmatrix} -\frac{1}{2} \nabla^2 + g |\psi_1|^2 + g_{12} |\psi_2|^2 & 0 \\ 0 & -\frac{1}{2} \nabla^2 + g |\psi_2|^2 + g_{12} |\psi_1|^2 \end{pmatrix}, \quad (5.23)$$

and

$$\hat{\psi} = \begin{pmatrix} \psi_1 \\ \psi_2 \end{pmatrix}. \quad (5.24)$$

Consider the unitary transformation

$$\hat{W}(t) = e^{i\Omega \sigma_y t}, \quad (5.25)$$

with the property  $\hat{W} \hat{W}^\dagger = \mathbf{1}$ . We are able to rewrite  $\hat{\psi} = \hat{W} \hat{W}^\dagger \hat{\psi}'$  and  $\hat{H} = \hat{W} \hat{W}^\dagger \hat{H}'$ , and the GP equation 5.22 as

$$i \frac{\partial}{\partial t} (\hat{W} \hat{\psi}') = \hat{W} \hat{H}' \hat{\psi}', \quad (5.26)$$

which can be set in another way

$$i \frac{\partial \hat{\psi}'}{\partial t} = \hat{H}' \hat{\psi}', \quad (5.27)$$

where  $\hat{\psi}' = \hat{W}^\dagger \hat{\psi}$  and  $\hat{H}' = \hat{W}^\dagger \hat{H} \hat{W}$ . With some algebraic steps, we get the GP equations in the rotating frame in terms of dressed states  $\psi_\pm = (\psi_1 \pm i\psi_2)/\sqrt{2}$ , in such a way a dressed GP equation becomes

$$i \frac{\partial \hat{\psi}_D}{\partial t} = \hat{H}_D \hat{\psi}_D, \quad (5.28)$$

with

$$\hat{H}_D = \begin{pmatrix} -\frac{1}{2} \nabla^2 + g_{++} |\psi_+|^2 + g_{+-} |\psi_-|^2 & 0 \\ 0 & -\frac{1}{2} \nabla^2 + g_{--} |\psi_-|^2 + g_{+-} |\psi_+|^2 \end{pmatrix}, \quad (5.29)$$

and  $\hat{\psi}_D = [\psi_+ \ \psi_-]^\text{T}$ , with the dressed interaction parameters given by  $g_{++} = g_{--} = (g_{11} + g_{22} + 2g_{12})/4$  and  $g_{+-} = (g_{11} + g_{22})/2$ . In this transformed variables, we can get the BdG spectrum

$$\begin{aligned} \omega_{\ell, \pm}^2 &= \epsilon_\ell \left[ \epsilon_\ell + \frac{1}{8\pi} (g_{++} + g_{--}) \right] \\ &\pm \frac{\epsilon_\ell}{8\pi} \sqrt{(g_{++} - g_{--})^2 + 4g_{+-}^2}, \end{aligned} \quad (5.30)$$

or written with the old variables

$$\omega_{\ell+}^2 = \epsilon_{\ell} \left[ \epsilon_{\ell} + \frac{1}{8\pi} (g_{12} + 3g) \right], \quad (5.31a)$$

$$\omega_{\ell-}^2 = \epsilon_{\ell} \left[ \epsilon_{\ell} + \frac{1}{8\pi} (g_{12} - g) \right], \quad (5.31b)$$

where we are assuming  $g_{11} = g_{22} = g$ . The stability diagram of the extreme regimes approximation is displayed in Fig. 5.4, where we can see in the panel 5.4a, the good approximation in the regime of weak coupling, by comparison with the panel 5.3a, but a very different behavior in the strong coupling limit, when we compare the panels 5.4b and 5.3b, which makes the stationary BdG approximation no longer reliable when the Rabi coupling is increased.

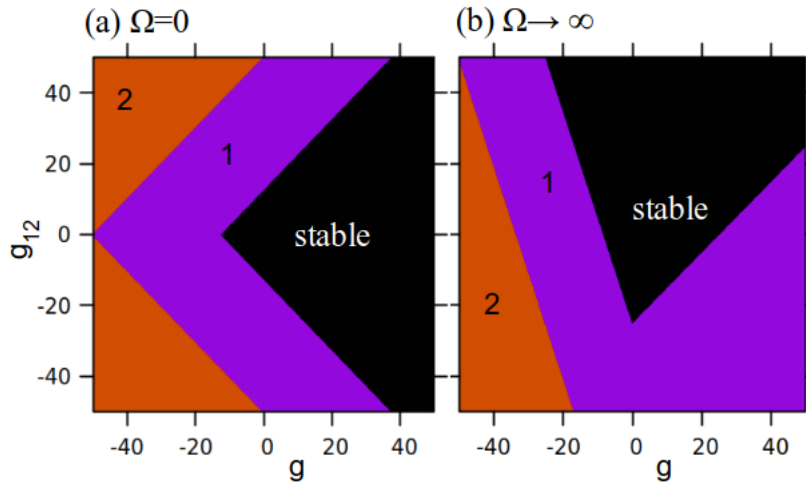


Figure 5.4: (Color on-line) BdG stability diagrams regarding the extreme regimes. Black places are stable regions ( $\text{Im}(\omega_{\ell,\pm}) = 0$ ) and the colors provide the dominant unstable angular modes ( $\text{Im}(\omega_{\ell,\pm}) \neq 0$ ). Violet places stand for the unstable angular mode  $\ell = 1$  and orange for  $\ell = 2$ . (a) Zero Rabi coupling regime, see Eq. (5.21). (b) Strong Rabi coupling regime, see Eqs. (5.31a) and (5.31b).

## 5.4 Stability of periodic solutions

Now we consider the evolution of the system given by the homogeneous oscillating solutions (5.15), in order to better take into account the role of Rabi coupling in the dynamics. Those solutions can be studied dynamically by the time-dependent Floquet method, as in Refs. [27, 28]. If we suppose small amplitude oscillations around them

$$\psi_j(\theta, \phi, t) = e^{-i\gamma t} [f_j(t) + \zeta_{j,\ell}(\theta, \phi, t)], \quad (5.32)$$

with

$$\zeta_{j,\ell}(\theta, \phi, t) = \tilde{u}_{j,\ell}(t)Y_{\ell,m}(\theta, \phi) + \tilde{v}_{j,\ell}^*(t)Y_{\ell,m}(\theta, \phi), \quad (5.33)$$

where the amplitudes  $\tilde{u}_{j,\ell}$  and  $\tilde{v}_{j,\ell}$  are periodic functions with the same period of the densities. When inserting (5.32) into the GP equations (5.3a) and (5.3b), we neglect

the second and higher order terms of the amplitude. Then, we get the following matrix equation [27]:

$$i \frac{d}{dt} \tilde{\mathbf{u}}_\ell = \tilde{\mathbf{M}} \tilde{\mathbf{u}}_\ell, \quad (5.34)$$

where  $\tilde{\mathbf{u}}_\ell(t) \equiv [\tilde{u}_{1,\ell}(t) \tilde{v}_{1,\ell}(t) \tilde{u}_{2,\ell}(t) \tilde{v}_{2,\ell}(t)]^T$  and

$$\tilde{\mathbf{M}} = \begin{pmatrix} D_1 & g f_1^2 & G_{12} - i\Omega & g_{12} f_1 f_2 \\ -g f_1^{*2} & -D_1 & -g_{12} f_1^* f_2^* & -G_{12}^* - i\Omega \\ G_{12}^* + i\Omega & g_{12} f_1 f_2 & D_2 & g f_2^2 \\ -g_{12} f_1^* f_2^* & -G_{12} + i\Omega & -g f_2^{*2} & -D_2 \end{pmatrix}, \quad (5.35)$$

with  $D_j \equiv (\epsilon_\ell - \gamma) + 2g|f_j|^2 + g_{12}|f_{3-j}|^2$  and  $G_{12} \equiv g_{12} f_1 f_2^*$ . When the system is driven by a periodic time-dependent Hamiltonian, the Floquet theorem [11] predicts that the solutions  $\tilde{\mathbf{u}}_\ell(t)$  can be written as

$$\tilde{\mathbf{u}}_\ell(t) = \exp(\lambda_\ell t) \mathbf{p}_\ell(t), \quad (5.36)$$

where  $\mathbf{p}_\ell$  are periodic functions, which in our case satisfy the same periodicity of the densities. The factor  $\lambda_\ell$  stands for the Floquet exponent. From its periodic property at the time  $t = T$ ,  $\mathbf{p}_\ell(T) = \mathbf{p}_\ell(0)$ , we get

$$\tilde{\mathbf{u}}_\ell(T) = \exp(\lambda_\ell T) \mathbf{p}_\ell(0). \quad (5.37)$$

We carry out these calculations performing the method presented in the Ref. [27], *i.e.*, we integrate the Floquet Eq. (5.34) by a fourth-order Runge-Kutta method (RK4) from  $t = 0$  to  $t = T$  (a complete period), supposing four different initial conditions for the amplitudes, which are  $\tilde{\mathbf{u}}_\ell(t = 0) = [1 \ 0 \ 0 \ 0]^T$ ,  $[0 \ 1 \ 0 \ 0]^T$ ,  $[0 \ 0 \ 1 \ 0]^T$ , and  $[0 \ 0 \ 0 \ 1]^T$ . For each initial vector we get a different vector at the time  $t = T$ , then we write these four final vectors as a column matrix  $\mathbf{F} = [\tilde{\mathbf{u}}_\ell^{(1)} \ \tilde{\mathbf{u}}_\ell^{(2)} \ \tilde{\mathbf{u}}_\ell^{(3)} \ \tilde{\mathbf{u}}_\ell^{(4)}]$ . That matrix represents  $e^{\lambda_\ell T}$ . If we suppose the eigenvalues of  $\mathbf{F}$  are  $\tilde{\lambda}_\ell$ , then we are able to get the exponent  $\lambda_\ell$  by the natural logarithm  $\lambda_\ell = \log(\tilde{\lambda}_\ell/T)$ . If the system evolves to the time  $t = T$  with a nonzero real part in the full spectrum ( $\text{Re}(\lambda_\ell) > 0$ ), it means that the solution  $\tilde{\mathbf{u}}$  is growing exponentially with  $t$ , and it is no longer stable, in other words, the uniform oscillating system is dynamically unstable by excitations from the orbital angular mode  $\ell$ . In this approach, we are able to study how long the BdG approach for stationary solution returns correct results. In Fig. 5.5, we present a stability diagram obtained from the oscillating functions  $f_j$  for a complete period  $T$ . In panel 5.5a, we see a good agreement with the stationary result in the panel 5.3a, but a very different result from its panel 5.3b. Then we conclude that as soon as the Rabi coupling is turned on, the better way to study the stability of the system is to carry out the Floquet method. Some set of parameters in these Floquet diagrams can be observed separately in Fig. 5.6, where the spectrum of unstable modes clarifies the meaning of very faint lines in the diagrams. The Floquet spectrum is able to predict resonance regions and in the next section 5.4.1, we compare it with a semi-analytic model in the regime where  $|g_{12} - g| \ll \Omega$ .

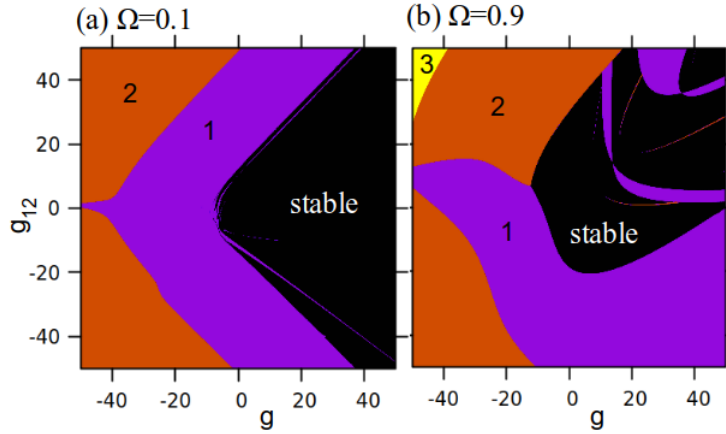


Figure 5.5: (Color on-line) Floquet stability diagrams based on  $\text{Max}[\text{Re}(\lambda_\ell)]$ , see Eq. (5.34). Black places are stable regions ( $\text{Max}[\text{Re}(\lambda_\ell)] \leq 0$ ) and the colors provide the dominant angular unstable modes ( $\text{Max}[\text{Re}(\lambda_\ell)] > 0$ ), violet places stand for the unstable angular mode  $\ell = 1$ , orange for  $\ell = 2$  and yellow for  $\ell = 3$ . (a) Rabi coupling constant  $\Omega = 0.1$ . (b)  $\Omega = 0.9$ . From [19].

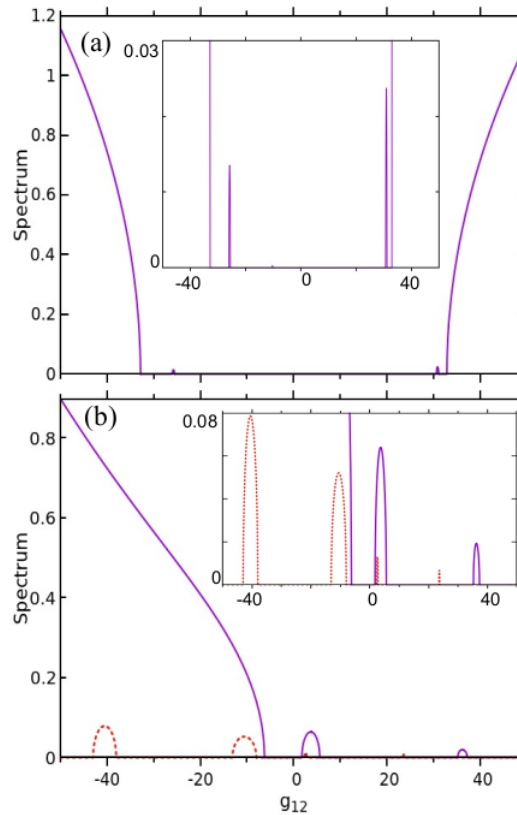


Figure 5.6: (Color on-line) Floquet spectrum  $\text{Max}[\text{Re}(\lambda_\ell)]$  as a function of inter-species interaction, see Eq. (5.34). Violet solid lines stand for the unstable angular mode  $\ell = 1$ , and red dashed lines refer to  $\ell = 2$ . Intra-species interaction and Rabi coupling constant are given by  $(g, \Omega) = (20, 0.1)$  and  $(40, 0.9)$ . Which are displayed in panels (a) and (b), respectively. Inset panels show the lower peaks in the main panel. From [19].

### 5.4.1 Resonance conditions

We suppose the regime where  $\xi \ll \Omega$ , with  $\xi = g_{12} - g$ . In a  $\xi$ -first order approach, the solutions are slightly perturbations of Eqs. (5.14a) and (5.14b), when  $g_{12} = g$ .



As proposed in [27], we can write them as

$$\psi_1(t) = \phi_1(t)e^{-i(\mu+\delta\mu)t}, \quad (5.38a)$$

$$\psi_2(t) = \phi_2(t)e^{-i(\mu+\delta\mu)t}, \quad (5.38b)$$

where

$$\phi_1(t) = \frac{1}{\sqrt{4\pi}}\cos(\Omega t + \pi/4)[1 + i\Delta(t)], \quad (5.39a)$$

$$\phi_2(t) = \frac{1}{\sqrt{4\pi}}\sin(\Omega t + \pi/4)[1 - i\Delta(t)], \quad (5.39b)$$

and  $\Delta(t) = (\xi/32\pi\Omega)\cos(2\Omega t)$ , with the chemical potential  $\mu = (2g + \xi)/8\pi$ , and a phase correction  $\delta\mu = -\xi/16\pi$ . If we consider small amplitude fluctuations around the solutions in Eqs. (5.38a) and (5.38b), we get

$$\psi_1(\theta, \phi, t) = [\phi_1(t) + \delta\phi_1(\theta, \phi, t)], \quad (5.40a)$$

$$\psi_2(\theta, \phi, t) = [\phi_2(t) + \delta\phi_2(\theta, \phi, t)]. \quad (5.40b)$$

We can manage a useful transformation [28]

$$\delta\phi_d = \phi_1^*\delta\phi_1 + \phi_2^*\delta\phi_2, \quad (5.41a)$$

$$\delta\phi_s = \phi_1\delta\phi_2 - \phi_2\delta\phi_1, \quad (5.41b)$$

for which we have the inverse transformation (neglecting second and higher order terms with  $\xi$ )

$$\delta\phi_1 = 4\pi[\phi_1\delta\phi_d - \phi_2^*\delta\phi_s], \quad (5.42a)$$

$$\delta\phi_2 = 4\pi[\phi_2\delta\phi_d + \phi_1^*\delta\phi_s]. \quad (5.42b)$$

In this way, by inserting the perturbed functions into the GP equation, and neglecting second and higher order terms with  $\xi$ ,  $\delta\phi_d$ , and  $\delta\phi_s$ , we get the equations of motion of the excitations

$$\begin{aligned} i\frac{\partial\delta\phi_d}{\partial t} &= \left\{ -\frac{1}{2}\nabla_{\theta,\phi}^2 + \frac{g}{4\pi} + \frac{\xi}{16\pi}[1 + 2\cos(4\Omega t)] \right\} \delta\phi_d \\ &+ \left\{ \frac{g}{4\pi} + \frac{\xi}{16\pi}[1 + \cos(4\Omega t)] \right\} \delta\phi_d^* \\ &+ \left\{ -\frac{g}{4\pi}\sin(4\Omega t) + \frac{\xi}{8\pi}\sin(4\Omega t) \right\} \delta\phi_s \\ &+ \left\{ -\frac{3g}{16\pi}\sin(4\Omega t) - \frac{\xi}{16\pi}\sin(4\Omega t) \right\} \delta\phi_s^*, \end{aligned} \quad (5.43)$$

and

$$\begin{aligned} i\frac{\partial\delta\phi_s}{\partial t} &= -\left\{ \frac{\xi}{8\pi}\sin(4\Omega t) \right\} \delta\phi_d - \left\{ \frac{\xi}{16\pi}\sin(4\Omega t) \right\} \delta\phi_d^* \\ &+ \left\{ -\frac{1}{2}\nabla_{\theta,\phi}^2 + \frac{\xi}{16\pi}[1 - 2\cos(4\Omega t)] \right\} \delta\phi_s \\ &- \left\{ \frac{\xi}{16\pi}[1 + \cos(4\Omega t)] \right\} \delta\phi_s^*. \end{aligned} \quad (5.44)$$

We can assume that the dynamics of the excitations evolve in time in a much slower scale than the sinusoidal functions  $\sin(4\Omega t)$  and  $\cos(4\Omega t)$ , in such a way that is convenient take the average of Eqs. (5.43) and (5.44) in time, i.e, given a time-dependent function  $J(t)$ , the average in the period  $T' = 2\pi/(4\Omega)$  of the sinusoidal functions is

$$\langle J \rangle_{T'} = \frac{1}{T'} \int_0^{T'} dt J(t), \quad (5.45)$$

then the time-averaged equations of motion can be written in the form of the Floquet equation

$$i \frac{\partial \delta \phi}{\partial t} = \mathbf{Z} \delta \phi, \quad (5.46)$$

where we have  $\delta \phi = [\delta \phi_d \ \delta \phi_d^* \ \delta \phi_s \ \delta \phi_s^*]^T$  (the symbol T stands for the transpose of a vector) and the Floquet matrix is given by

$$\mathbf{Z} = \begin{pmatrix} -\frac{1}{2} \nabla_{\theta, \phi}^2 + \frac{g}{4\pi} + \frac{\xi}{8\pi} & \frac{g}{4\pi} + \frac{\xi}{16\pi} & 0 & 0 \\ -\frac{g}{4\pi} - \frac{\xi}{16\pi} & \frac{1}{2} \nabla_{\theta, \phi}^2 - \frac{g}{4\pi} - \frac{\xi}{16\pi} & 0 & 0 \\ 0 & 0 & -\frac{1}{2} \nabla_{\theta, \phi}^2 + \frac{\xi}{16\pi} & -\frac{\xi}{16\pi} \\ 0 & 0 & \frac{\xi}{16\pi} & \frac{1}{2} \nabla_{\theta, \phi}^2 - \frac{\xi}{16\pi} \end{pmatrix}. \quad (5.47)$$

Note that, the sinusoidal functions are zero in the average, but  $\delta \phi(t)$  and time-independent terms are about the same as they were before the average calculation. We can suppose the fluctuations amplitudes as stationary functions which go with the spherical harmonics  $\delta \phi(\theta, \phi, t) = \delta \phi_0 Y_{\ell, m}(\theta, \phi) e^{-i\omega_\ell t}$ , where we can consider  $\delta \phi_0$  as a vector of constants. In this way we get a BdG matrix system

$$\omega_\ell \delta \phi_0 = \tilde{\mathbf{Z}} \delta \phi_0, \quad (5.48)$$

with

$$\tilde{\mathbf{Z}} = \begin{pmatrix} \epsilon_\ell + \frac{g}{4\pi} + \frac{\xi}{8\pi} & \frac{g}{4\pi} + \frac{\xi}{16\pi} & 0 & 0 \\ -\frac{g}{4\pi} - \frac{\xi}{16\pi} & -\epsilon_\ell - \frac{g}{4\pi} - \frac{\xi}{16\pi} & 0 & 0 \\ 0 & 0 & \epsilon_\ell + \frac{\xi}{16\pi} & -\frac{\xi}{16\pi} \\ 0 & 0 & \frac{\xi}{16\pi} & -\epsilon_\ell - \frac{\xi}{16\pi} \end{pmatrix}, \quad (5.49)$$

for which we have the spectrum in the  $\xi$ -first order approach

$$\omega_{\ell, \pm}^{(d)} = \pm \left[ \sqrt{\epsilon_\ell(\epsilon_\ell + g/2\pi)} + \frac{\epsilon_\ell \xi}{16\pi \sqrt{\epsilon_\ell(\epsilon_\ell + g/2\pi)}} \right], \quad (5.50a)$$

$$\omega_{\ell, \pm}^{(s)} = \pm \left( \epsilon_\ell + \frac{\xi}{16\pi} \right). \quad (5.50b)$$

They are natural frequencies of excitation of the system regardless of Rabi oscillation. The parametric resonance conditions for an external potential is achieved when

its frequency goes with about twice of the natural frequencies [87]. Once the Rabi coupling potential drives the excitations with  $\cos(4\Omega t)$  and  $\sin(4\Omega t)$  in Eqs. (5.43) and (5.44), the three critical Rabi coupling frequencies for which we have parametric resonance are

$$4\Omega_\ell^{(d)} = 2\omega_{\ell,+}^{(d)}, \quad (5.51a)$$

$$4\Omega_\ell^{(s)} = 2\omega_{\ell,+}^{(s)}, \quad (5.51b)$$

$$4\Omega_\ell^{(ds)} = \omega_{\ell,+}^{(d)} + \omega_{\ell,+}^{(s)}, \quad (5.51c)$$

which stand for density-density, spin-spin and density-spin resonances, respectively.

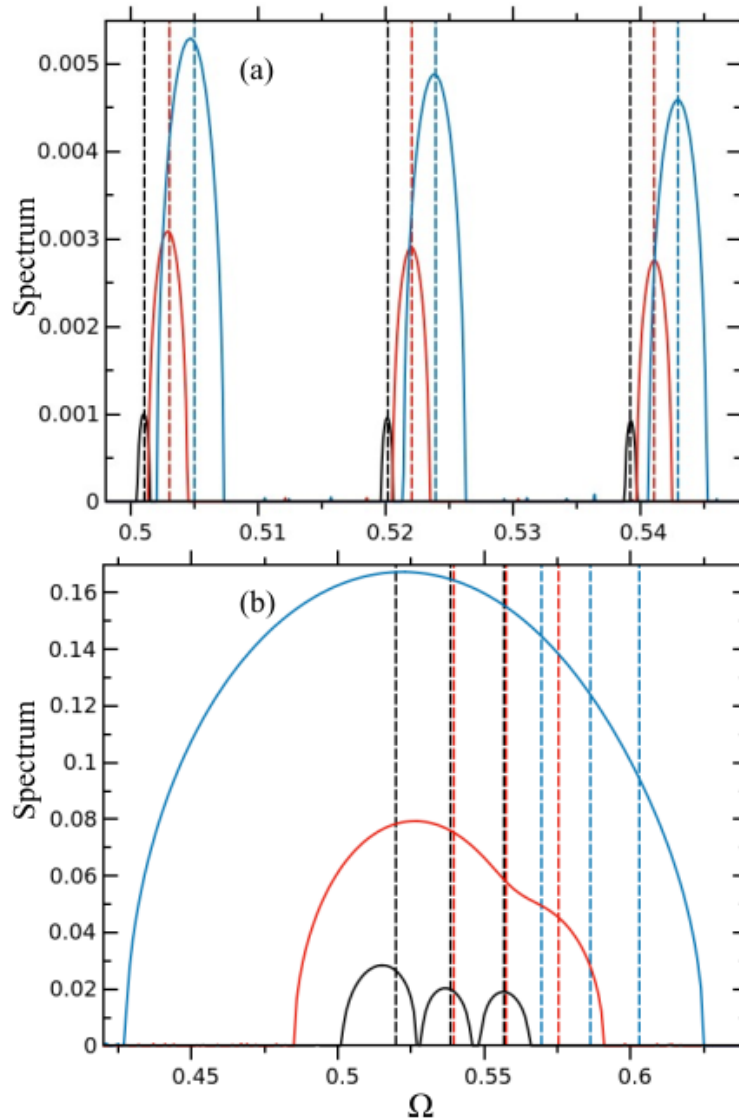


Figure 5.7: (Color online) Resonance couplings and unstable Floquet spectrum as functions of the Rabi coupling  $\Omega$ . The vertical dashed lines stand for the three predicted resonance critical couplings (5.51a), (5.51b) and (5.51c) for  $g = 1$ , while the peaks are provided by the unstable Floquet spectrum ( $\text{Max}[\text{Re}(\lambda_\ell)]$ ), see Eq. (5.34). Only the unstable angular mode  $\ell = 1$  is actually important for the chosen parameters. (a) Cases where the inter-species interactions are  $g_{12} = 1.1, 1.3$ , and  $1.5$ , on black/bottom, red/middle and blue/top set of peaks, respectively. (b) Cases where  $g_{12} = 3.0, 5.0$ , and  $8.0$ , on black/bottom, red/middle and blue/top peaks, respectively. From [19].

Note we have considered just the plus-sign (+) branches, since we are considering

the Rabi coupling parameter  $\Omega$  as a positive real constant. The critical frequencies  $\Omega_\ell$  can be observed in the Floquet spectrum in the regime of  $g_{12} \approx g$ . When  $g_{12}$  becomes higher, the three peaks continuously merge into only one peak. In Fig. 5.7, we compare the Floquet spectrum with the approximations (5.51a), (5.51b), and (5.51c) for the resonance couplings. The spectrum shows us that once we increase the inter-species interaction  $g_{12}$ , the resonance peaks soon go away from the predicted ones, they also become closer and higher. Then we no longer can distinguish the peaks from each other, they become only one peak.

## 5.5 Dynamics

We investigate the dynamics of the system by performing the full numeric calculations of the coupled GP Eqs. (5.3a) and (5.3b), carrying out the spectral method introduced in [18]. We perform the calculations with a spatial grid in  $\theta$  and  $\phi$  directions of size  $256 \times 256$ , with step sizes  $d\theta = \pi/256 \approx 0.013$  and  $d\phi = 2\pi/256 \approx 0.025$ , and time step  $dt = 10^{-5}$ . The GP equations are solved starting from homogeneous solutions, where each species has half of the total population, i.e.,  $\psi_1 = \psi_2 = 1/\sqrt{8\pi}$ , as in Eq. (5.13), with a 5% random noise added to each point in the mesh grid. We are able to compare how long the homogeneous periodic solutions (5.15) solved by RK4 method provide a good model to describe the evolution of the populations. We track the stability behavior of homogeneous miscible initial states by displaying their overlap evolution, population dynamics, and density pattern when unstable modes are present. In order to estimate the miscibility of the system, we consider the overlap

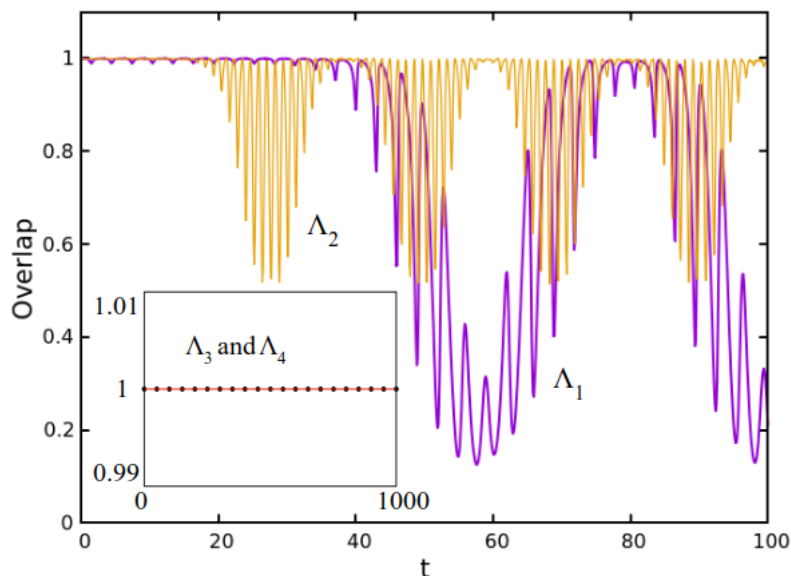


Figure 5.8: Overlap  $\Lambda(t)$  (see Eq. (2.24)) between the species for cases 1 to 4, depicted in  $\Lambda_1$  to  $\Lambda_4$ , where the corresponding values are calculated for the set of parameters intra- and inter-species interaction, and Rabi coupling constant  $(g, g_{12}, \Omega) = (1, 8, 0.50)$ ,  $(40, -10, 0.94)$ ,  $(1, 10, 0.10)$ , and  $(1, 25, 0.99)$ , respectively. Cases 1 and 2 are presented in the main panel on violet and orange solid lines, respectively. Cases 3 and 4 are displayed in the inset panel on the red-solid and black-dotted lines, respectively. From [19].

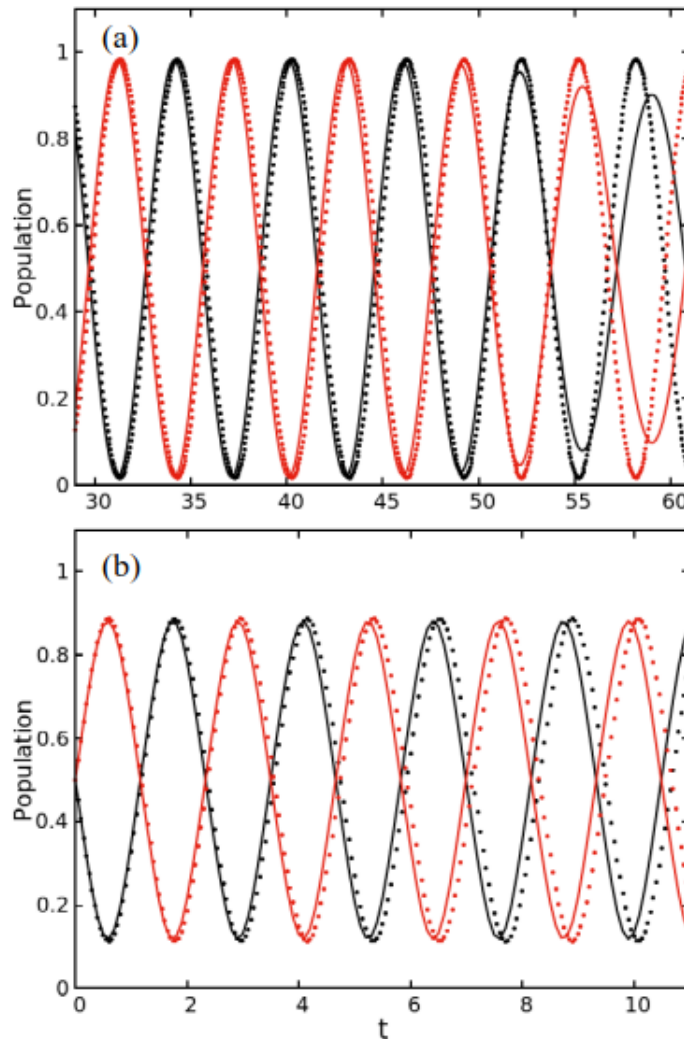


Figure 5.9: (Color on-line) Population dynamics  $P_j(t)$  (see Eq. (2.25)) of the species for the cases 1 and 2, with intra- and inter-species, and Rabi coupling constant given by  $(g, g_{12}, \Omega) = (1, 8, 0.50)$ ,  $(40, -10, 0.94)$ , respectively. The cases are displayed in panels (a) and (b), respectively. Solid lines stand for the full GP calculation of the system given by Eqs. (5.3a) and (5.3b), taking into account spatial-time-dependent wave functions and the dotted ones are homogeneous only time-dependent solutions (5.15). Black lines are species 1 and the red ones are species 2.

function  $\Lambda$  given in Eq. (2.24). Once the initial overlap decreases, it means that the initial miscible set up is no longer stable. In Fig. 5.8, we show the overlap dynamics of four different cases, where the set of parameters including intra- and inter-species interaction, and Rabi coupling constant are given by  $(g, g_{12}, \Omega) = (1, 8, 0.50)$ ,  $(40, -10, 0.94)$ ,  $(1, 10, 0.10)$ , and  $(1, 25, 0.99)$ , for which the stability predictions can be localized in Figs. 5.14b, 5.15, 5.5a and 5.14c, respectively. A complementary analysis can be made by observing the population dynamics of the previous cases. We already defined the population  $P_j$  of each species in (2.25). Fig. 5.9 shows us how the population oscillation is affected for unstable cases 1 and 2. The population behavior is closely related to the overlap, since both properties are changed when the miscible homogeneous functions Eq. 5.14a and (5.14b) are no longer the true solutions of the system. It is important to note that the overlap dynamics for unstable cases is driven by two different frequencies. The slow frequency is a periodic be-

havior of the miscibility, which was first observed in our previous work [18], and it happens only for specific choices for interaction parameters. Moreover, in this work, we observe a second frequency in the overlap dynamics, which is faster than the first one, and it is driven by the population dynamics frequency. In Fig. 5.10, we present two different cases where both frequencies are actually leading the overlap behavior. In panel 5.10a, we set the parameters of the case 2, which are  $(g, g_{12}, \Omega) = (40, -10, 0.94)$ , where we clearly see that the faster kind of overlap oscillation has the same frequency of the population dynamics. Another case, which we call case 5, is depicted in panel 5.10b. This case has the parameters  $(g, g_{12}, \Omega) = (-10, 20, 0.90)$ , for which we have the stability prediction in Fig. 5.5b. Here is not easy to observe some periodic behavior with two distinguished frequencies as before. This is an example where the slower kind of modulation is not a periodic oscillation. In this way, the periodic oscillation caused by the Rabi coupling can be expected for all choices of parameters, but the same statement it is not true for the slower kind of modulation. It may exhibit periodic behavior under certain conditions while being non-periodic under others, as already observed in [18]. The dynamics process of an unstable mode driving the behavior of the system can be more clearly seen in Fig. 5.11, where we observe how the densities of both species evolve in time for the parameters of the case 1, given by  $(g, g_{12}, \Omega) = (1.00, 8.00, 0.50)$ , which is suppose to be unstable by the angular mode  $\ell = 1$  in the panel 5.14b. By observing the density dynamics, we are able to see that after some time, a density pattern emerges in both species, and soon the species evolve to an immiscible setup. When the condensates become localized small clouds, where Faraday waves become difficult to be seen. Actually, in the last picture, it seems that the system is able to get rid of these waves. But in this case, the miscibility is periodic and the Faraday waves can survive for a long time. However, once the clouds grow again, this waves are going to be higher. Here we observe that both species are going to break into only one piece. This phenomenon confirms that the system is driven by the unstable mode  $\ell = 1$ , as predicted by the Floquet spectrum. We previously observed in [18], that unstable angular modes  $\ell$  are able to break the condensate into a corresponding number  $\ell$  of pieces, but here we also point out that these angular modes are also able to trigger Faraday waves, once the Rabi oscillations effectively drive time-dependent interaction energy [83], as a parametric modulation does. Then, as predicted in another geometry [27], Faraday waves can also coexist with the immiscible phase on the spherical bubble surface.

A similar calculation is performed in Fig. 5.12, where we present how the densities evolve for the unstable cases 2, and 5, with parameters  $(g, g_{12}, \Omega) = (40, -10, 0.94)$ , and  $(-10, 20, 0.9)$ , respectively. The first row of the figure shows us the Faraday patterns arise, and species going to an immiscible-phase state, breaking into one piece. In the second row of the figure, we see that both condensates soon break into two pieces, where also Faraday patterns emerge. The stability of cases 2, and 5

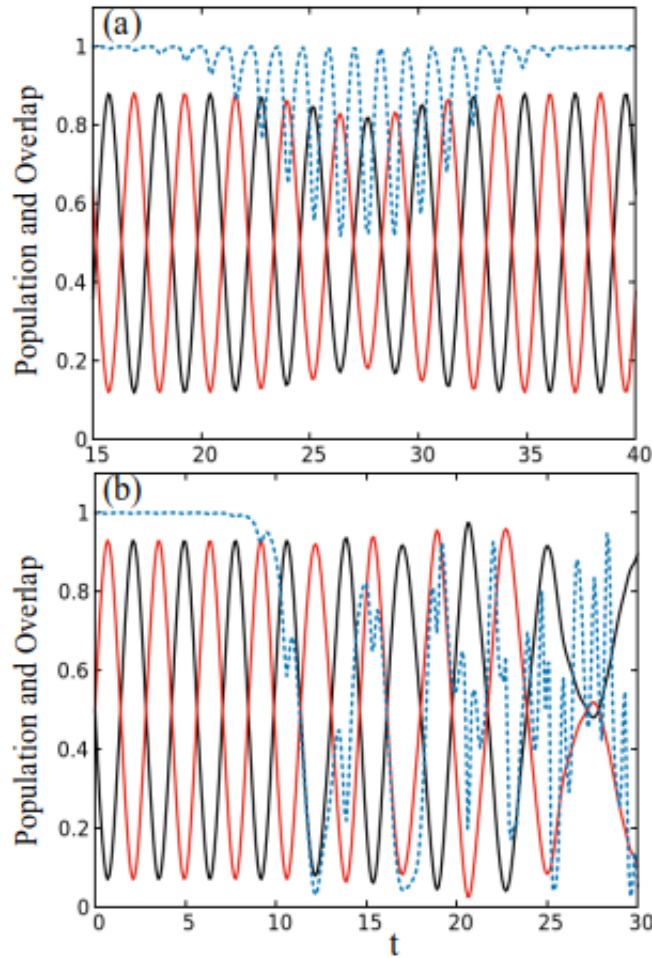


Figure 5.10: (Color on-line) Population  $P_j(t)$  and Overlap  $\Lambda(t)$  dynamics, see Eqs. (2.25) and (2.24), respectively. Black and red solid lines are populations of species 1 and 2, respectively. The overlap between the species is displayed in the dashed blue line. (a) Case 2, with intra- and inter-species interaction, and Rabi coupling constant given by  $(g, g_{12}, \Omega) = (40, -10, 0.94)$ . (b) Case 5, with parameters  $(-10, 20, 0.90)$ .

can be checked by the Floquet spectrum in the panels 5.15 and 5.5a), respectively. Which predict that cases 2 and 5 are unstable, and driven by the modes  $\ell = 1$  and  $\ell = 2$ , respectively. The simulations of the dynamics confirm these predictions, and in each case the condensates are likely to break into one and two pieces, respectively. Therefore, the Floquet spectrum correctly predicts the stability behavior observed in the dynamics. In the next section 5.6, we compare all methods with the dynamics results, and observe that Floquet method provides the most suitable analysis as soon as  $\Omega > 0$ . However, BdG spectrum can return about the same results for small coupling constant  $\Omega \ll 1$ . In summary, the density dynamics simulation of the unstable cases 1, 2 and 5 displayed on the figures 5.11 and 5.12, show us the phase separation is going to happen in a higher order of density than the Faraday patterns, and if the condensates quickly break into localized small clouds, the Faraday waves effect is not likely to be seen.

In Fig. 5.13, we quantify the effect of the unstable modes on the dynamics by the square modulus of the coupling  $|c_{\ell,m}|^2$ , where the coefficients  $c_{\ell,m}$  are defined in



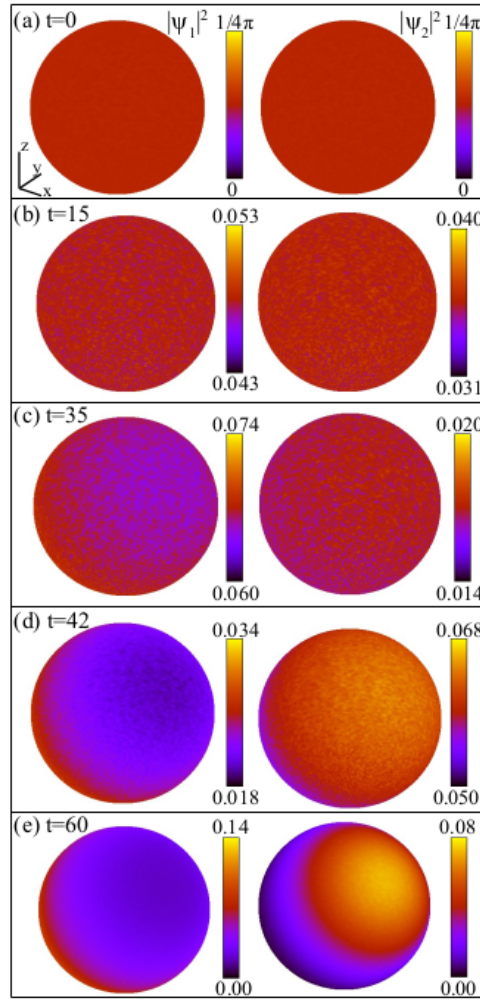


Figure 5.11: (Color online) Density dynamics  $|\psi_j|^2$  of the case 1 with intra- and inter-species interaction, and Rabi coupling constant given by  $(g, g_{12}, \Omega) = (1, 8, 0.50)$ . Species one is displayed on the left, and species two on the right. Panels (a)-(e) refer to time  $t = 0, 15, 35, 42,$  and  $60,$  respectively. Species 1 is displayed on the left, and species 2 on the right.

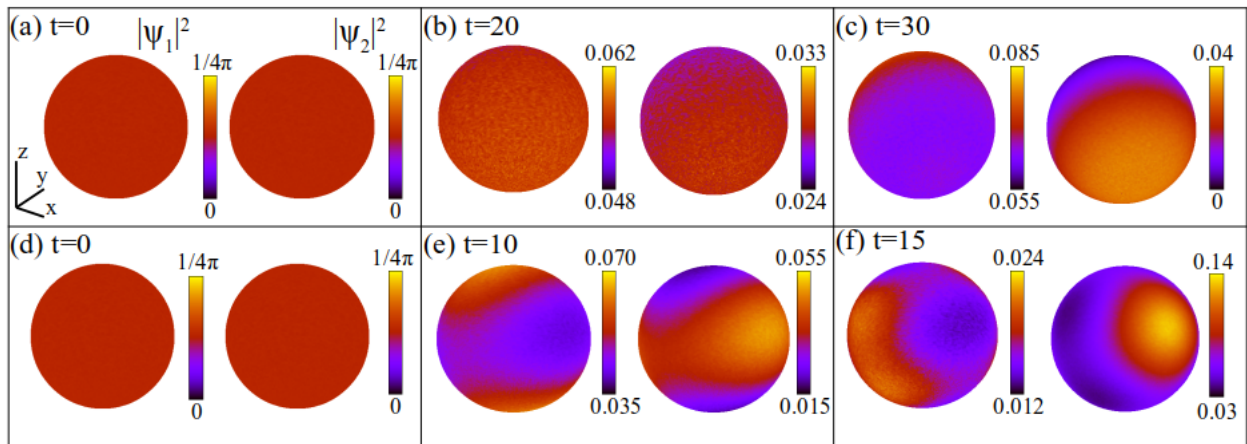


Figure 5.12: (Color online) Density dynamics  $|\psi_j|^2$  of the cases 2, and 5 with intra- and inter-species interaction, and Rabi coupling constant given by  $(g, g_{12}, \Omega) = (40, -10, 0.94),$  and  $(-10, 20, 0.90),$  respectively. Species one is displayed on the left, and species two on the right. The first row displays case 2 on panels (a)-(c) for time  $t = 0, 20,$  and  $30,$  respectively. The second row presents the case 5 on the panels (d)-(f) for  $t = 0, 10,$  and  $15,$  respectively.



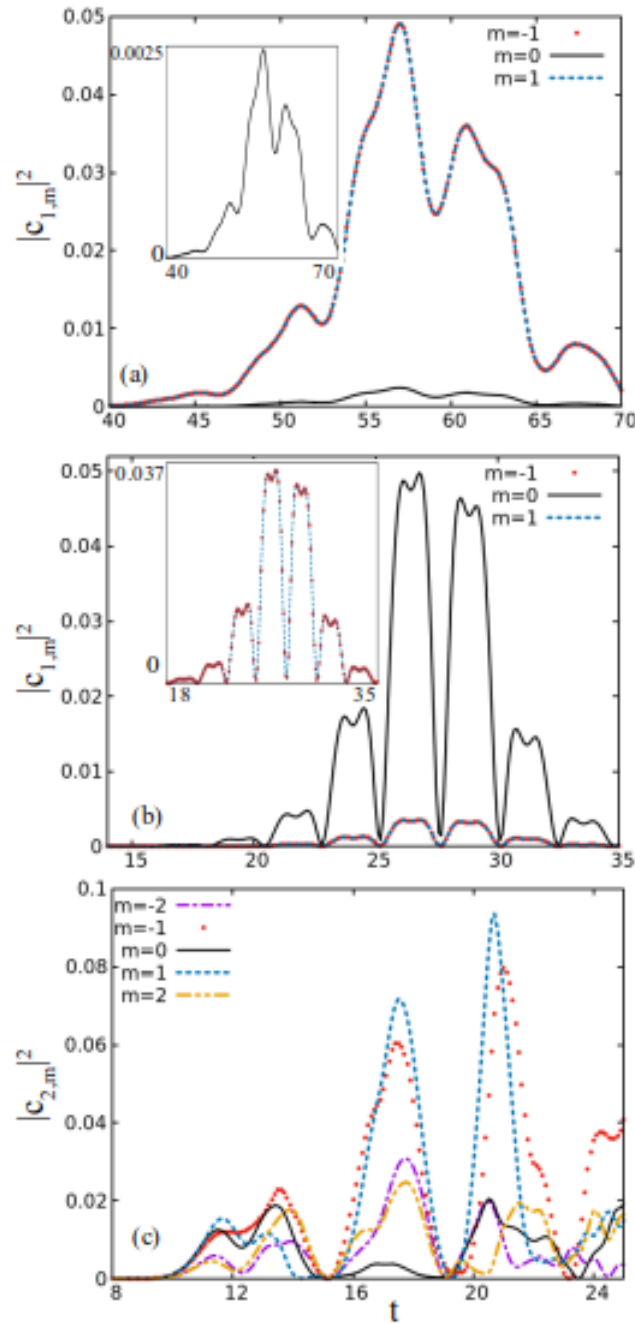


Figure 5.13: (Color online) Coupling parameters  $|c_{\ell,m}(t)|^2$  of species 1 as functions of time  $t$  [Eq. (5.52)]. Cases 1, 2, and 5 are depicted in (a), (b), and (c), with intra- and inter-species interaction, and Rabi coupling constant given by  $(g, g_{12}, \Omega) = (1, 8, 0.50)$ ,  $(40, -10, 0.94)$ , and  $(-10, 20, 0.90)$ , respectively. The insets in panels (a) and (b) stand for the lower lines of the main panels.

(5.52)

$$c_{\ell,m}(t) = \langle Y_{\ell,m} | \psi_j \rangle = \int dS Y_{\ell,m}^*(S) \psi_j(S, t). \quad (5.52)$$

We calculate the coupling for the species 1 wave function coupled with the spherical harmonics  $Y_{\ell,m}(S) = Y_{\ell,m}(\theta, \phi)$ . We observe the three unstable cases 1, 2, and 5. Once an angular mode  $\ell$  is unstable, the amplitudes of the couplings regarding each degenerate mode  $m = -\ell, \dots, \ell$  are arbitrary. Note that in case 5, depicted on the panel 5.13c, we show only the coupling with degenerate modes associated with

$\ell = 2$ , since they are the dominant ones, and the early modes to drive the dynamics. Modes regarding  $\ell = 1$  also can be important for longer times. For cases with  $\ell = 1$ , the coupling with the modes  $m = -1, 0, 1$  has the same behavior, but the mode  $m = 0$  has a different amplitude of the modes  $m = \pm 1$ . When  $\ell > 1$ , this symmetric behavior between the modes  $m$  is no longer observed.

## 5.6 Methods comparison

We already have stressed out in section 5.2 how the true solutions can be different from stationary ones, when the Rabi coupling is leading the dynamics. The condensate wave functions go with periodic functions in time, and therefore the associate spectrum can be very distinct from the spectrum of stationary solutions. In this section, we compare the BdG and Floquet spectrum, which are actually suitable for stationary and periodic functions in time, respectively. Once the Rabi coupling constant is increased, and the oscillating period of population dynamics becomes short, the methods are more likely to disagree from each other. In Fig. 5.14, we set together all stability approximations previously discussed in order to observe more deeply how they are related to each other. In panels 5.14a, 5.14b and 5.14c we display three different regimes of Rabi coupling. In the weak region  $\Omega = 0.01$ , we see the complete BdG spectrum, the zero limit  $\Omega = 0$ , and the Floquet scheme returning the same spectrum as we already expected, based on the very similar behavior of the stationary and oscillating solutions in this regime, see the case  $\Omega = 0.01$  in Fig. 5.2. Conversely, when the Rabi coupling constant is increased, the spectrum of the approximations become very different from each other, and once the coupling grows ( $\Omega \rightarrow 1$ ), even the stationary dressed states ( $\Omega \rightarrow \infty$ ) return bad results compared with the Floquet spectrum. An even deeper analysis is provided in Fig. 5.16, which displays simultaneously the different role of the Rabi coupling depending on the inter-species interaction, where it is very clear that the coupling is able to open a large region of stability, which makes the unstable behavior to be postponed. But in some situations it can make the system unstable, even when the BdG spectrum provides no clue of instability. This phenomenon is also depicted for fixed parameters in Fig. 5.15. We display the two different set of interaction parameters  $(g, g_{12}) = (1, 15)$  and  $(40, -10)$ , the first one is driven from an unstable to a stable solution by the increasing of the Rabi coupling, and the second one is led from a stable regime to an unstable one when the coupling becomes higher.

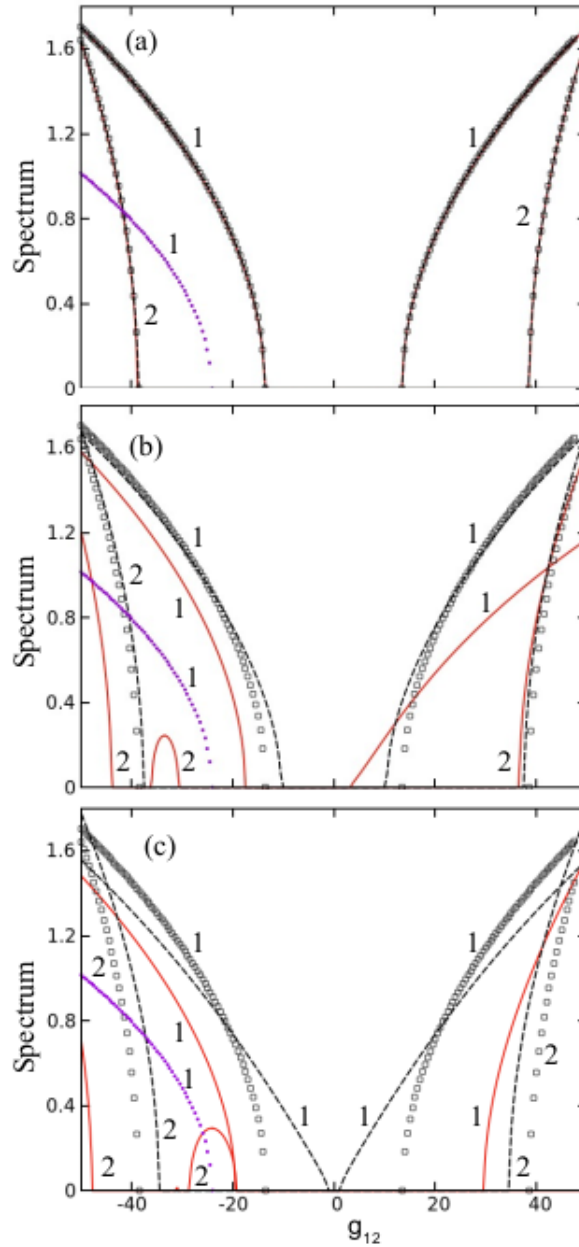


Figure 5.14: (Color on-line) Maximum unstable spectrum for each unstable angular mode  $\ell$  as function of the inter-species interaction  $g_{12}$  and Rabi coupling constant  $\Omega$ , with fixed intra-species interaction  $g = 1$ . BdG unstable spectrum is given by  $\text{Max}[\text{Im}(\omega_{\ell,\pm})]$  and Floquet unstable spectrum is provided by  $\text{Max}[\text{Re}(\lambda_{\ell})]$ . The numbers stand for the corresponding angular mode  $\ell$ . dashed lines refer to BdG spectrum, see Eq. (5.20). Empty squares present the BdG regime  $\Omega = 0$ , see Eq. (5.21). Violet dots show the strong BdG regime  $\Omega \rightarrow \infty$ , see Eqs. (5.31a) and (5.31b). Red solid lines display the Floquet spectrum, see Eq. (5.34). (a)  $\Omega = 0.01$ . (b)  $\Omega = 0.50$ . (c)  $\Omega = 0.99$ .

In table 5.1, we compare the predictions of BdG and Floquet methods with the full dynamics calculations for five cases mostly discussed in the text. We can check that the Floquet spectrum agrees with the dynamics simulations for all cases, then it is more suitable for our system than BdG method.

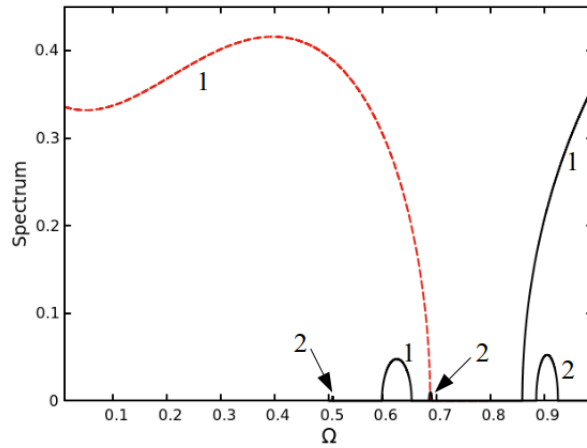


Figure 5.15: (Color on-line) Floquet maximum spectrum ( $\text{Max}[\text{Re}(\lambda_\ell)]$ ) of each unstable angular mode  $\ell$  as a function of the Rabi coupling  $\Omega$ , see Eq. (5.34). Cases  $(g, g_{12}) = (1, 15)$  and  $(40, -10)$  are displayed on red dashed lines and black solid lines, respectively. The numbers stand for the corresponding unstable angular mode  $\ell$ .

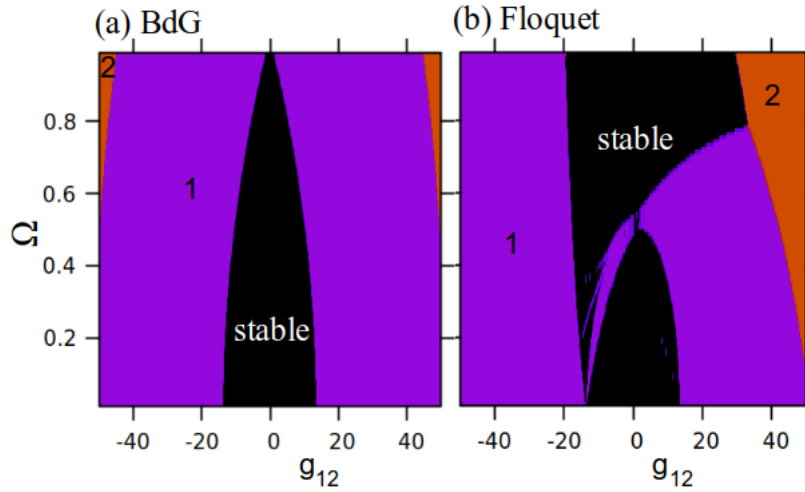


Figure 5.16: (Color on-line) Stability diagram as a function of inter-species interaction and Rabi coupling, with fixed intra-species interaction  $g = 1$ . Black places are stable regions and the colors provide the dominant unstable angular modes  $\ell$ . Violet places stand for  $\ell = 1$  and the orange ones for  $\ell = 2$ . (a) BdG, see Eq. (5.20). (b) Floquet, see Eq. (5.37).

Table 5.1: Stability status given by the three methods, given the parameter of intra- and inter-species interaction, and Rabi coupling constant  $\Omega, g, g_{12}$ . Unstable cases are displayed with the dominant unstable mode  $\ell$ . The reference figures where the results can be checked are set in parentheses.

Case	$g$	$g_{12}$	$\Omega$	BdG	Floquet	Dynamics
1	1	8	0.50	stable (5.14b)	$\ell = 1$ (5.14b)	$\ell = 1$ (5.8, 5.9a, 5.11)
2	40	-10	0.94	stable (5.3b)	$\ell = 1$ (5.15)	$\ell = 1$ (5.8, 5.9b, 5.10a, 5.12a-c)
3	1	10	0.10	stable (5.3a)	stable (5.5a)	stable (5.8)
4	1	25	0.99	$\ell = 1$ (5.14c)	stable (5.14c)	stable (5.8)
5	-10	20	0.90	$\ell = 1$ (5.3b)	$\ell = 2$ (5.5b)	$\ell = 2$ (5.10b, 5.12e-f)

## 5.7 Conclusions

We have investigated the dynamics and stability of homogeneous binary BEC mixtures trapped on a spherical bubble with populations oscillation achieved by Rabi coupling. As observed, the Rabi oscillations are able to drive the system to different stability profiles, once an effective time-oscillating interaction energy is achieved. In the two-dimensional spherical topology, discrete unstable orbital angular modes can rise and lead the BEC mixture to an immiscible phase separation, in which the condensate can break into a discrete corresponding number of pieces. Given the presence of effective interaction modulation, the unstable degenerate azimuthal angular modes can give rise to Faraday waves, which coexist with the separate phase.

We also show that for some range of parameters, the system can enter a periodic regime, where the miscibility of the species are going to change in time. The main feature regarding the spherical bubble topology where only discrete modes are possible, is that a phase separation where the condensates breaks into localized fixed number clouds, has a density order much higher than the Faraday waves patterns, and eventually the last phenomenon can be hidden when the former one is too much faster. Another interesting feature is that all discrete degenerate unstable modes have some role on the dynamics. Our findings are available in a preprint version at ArXiv [19]. We expect they impact the future experimental investigations which are been performed aboard the International Space Station [15–17, 31]. The presented model is very suitable for a coherently coupled BEC mixture of different hyperfine states trapped on a bubble shell.

# Chapter 6

## Conclusions

In this Thesis, we have focused on the emergent problems of Bose-Einstein condensates trapped on the bubble. Our main interest is to accomplish reliable mean-field studies about stability of condensed mass-balanced spinless mixtures confined on the surface of an ideal two-dimensional spherical shell. In the first work, we study stationary states, homogeneous or vortex-charged ones. In the second work, we investigate periodic states, observing the regimes where parametric resonance and Faraday Waves emerge.

In the first work, we set binary mixtures coupled only by the contact interactions. We study the stability of miscible stationary states. Among them, we consider homogeneous or inhomogeneous states. The last class of problems are related to vortex-states. In our set up, both species have a unitary vortex charge, however each species has opposite vortex sign to the other, in such a way the system has a zero net charge. For the first class of states, i.e, the homogeneous ones, we handle a analytical linearization of the GP equations by the BdG model, from which we can predict which modes are going to make the system unstable. In the regime where interactions are repulsive, we can observe a straightforward relationship between stability and miscibility. When a unstable angular mode rises, the species are no longer miscible, and therefore, the system finds a suitable solution where the overlap of the species goes to zero. In the second class of problems, the vortex-states, the miscibility-stability relationship is more complicated than the first case. The vortex-states are inherently inhomogeneous. We suppose initial miscible states, and we perform a numerical study of the BdG spectrum by assuming azimuthal symmetry and actually supposing a one-dimensional approximation. We develop a stability diagram for a large range of interaction parameters and or predictions succeed, once two-dimensional GP dynamics simulations confirm the predictions of the BdG model. We provide consistent results to support that Bose-Einstein condensate mixtures achieved in homogeneous or vortex-states can be dynamically stable on the surface of a spherical ideal hard sphere. Moreover, we have observed an interesting periodic regime of collapse and revival achieved by a dominant unstable mode, when it does not interfere with another modes. Our main results can be seen in the published paper available at the

physics journal *Phys. Rev. A* **104**, 033318 (2021) [18].

In the second work, we consider a binary mixture of condensates coupled by both interactions and Rabi coupling. In this system, the species can be converted to the other, and the population dynamics has a periodic behavior in time. We study the stability of spatial-homogeneous time-periodic states. In this kind of system, we have a very particular framework, where we can achieve parametric resonance and Faraday waves, without energy injection by external fields related to modulations in the interactions or the trap potential. We handle a stability analysis, performing a small amplitude linearization of the GP equations by BdG and Floquet methods. When we observe the full dynamics of the GP simulations, we note that when we have a time-dependent effective Hamiltonian, the Floquet method is the most suitable tool for prediction of the stability profile of the initial states, which performs much better than BdG method, even the approximation for strong modulated dressed states. Stability methods designed for stationary can not capture all the physics of periodic states. We have observed parametric resonance achieved by tuning the frequency of the Rabi oscillation. Once a unstable angular mode becomes important, it gives rise to Faraday waves and simultaneously to phase separations phase. Therefore, we can observe that both phenomena coexist when the initial state is unstable. And different from the first study of this thesis, here we observe a collapse and revival driven by two frequencies, the frequency of the periodic collapse, and also by the frequency of the Rabi oscillation, and like the first work, there is a very limited range of parameters for which the modes do not interfere and the system enter this periodic regime. Our findings are available in a preprint version at arXiv [19], which is expected to be published in an international physics journal in the next few months.

We are looking forward our results become the main references for the future experiments with mixture of condensates confined in a same bubble surface.

## 6.1 Perspectives

We have provided deep studies on dynamic stability of Bose-Einstein condensate mixtures trapped on the surface of spherical shells, which are reliable benchmarks for the present-day problem of ultracold gases confined on bubbles in microgravity environments. The cold atom community is very interested in physics of condensates in low dimensions, indeed in March of the present year, São Paulo city was the host of Workshop mostly devoted to this topic [88]. A bilateral collaboration between NASA (USA) and DLR (Germany) is launching a Laboratory BECCAL as successor of the CAL [31, 48]. Therefore, all community of Bose-Einstein condensates is expecting fruitful years of discoveries and important achievements coming in next generation of experiments handled on Laboratories aboard the International Space Station. is expected to lead in the next years. This Ph. D. Thesis and our published

works are supposed to be one of the main references for studies of stability of mixtures in bubbles. Beyond our findings, we expect that our numerical methods foster fundamental tools to handle future studies in curved geometries.



# Bibliography

- [1] S. N. Bose. Plancks Gesetz und Lichtquantenhypothese. *Z. Phys.*, 26:178–181, 1924.
- [2] A. Einstein. Quatentheorie des einatomigen idealen gases. *Sitzungber. Kgl. Preuss. Akad. Wiss.*, pages 261–267, 1924.
- [3] A. Einstein. Quatentheorie des einatomigen idealen gases. 2. *Sitzungber. Kgl. Preuss. Akad. Wiss.*, pages 3–14, 1925.
- [4] M. H. Anderson, J. R. Ensher, M. R. Matthews, C. E. Wieman, and E. A. Cornell. Observation of Bose-Einstein condensation in a dilute atomic vapor. *Science*, 269(5221):198–201, 1995.
- [5] K. B. Davis, M. O. Mewes, M. R. Andrews, N. J. van Druten, D. S. Durfee, D. M. Kurn, and W. Ketterle. Bose-Einstein condensation in a gas of sodium atoms. *Phys. Rev. Lett.*, 75:3969–3973, Nov 1995.
- [6] C. C. Bradley, C. A. Sackett, and R. G. Hulet. Bose-Einstein condensation of lithium: Observation of limited condensate number. *Phys. Rev. Lett.*, 78:985–989, Feb 1997.
- [7] C. J. Pethick and H. Smith. *Bose–Einstein Condensation in Dilute Gases*. Cambridge University Press, 2 edition, 2008.
- [8] Lev Pitaevskii and Sandro Stringari. *Bose-Einstein Condensation and Superfluidity*. International Series of Monographs on Physics. Oxford University Press, Oxford, 2016.
- [9] Alexander L. Fetter. Nonuniform states of an imperfect Bose gas. *Annals of Physics*, 70(1):67–101, 1972.
- [10] Jon H. Shirley. Solution of the Schrödinger equation with a Hamiltonian periodic in time. *Phys. Rev.*, 138:B979–B987, May 1965.
- [11] Mile na Grifoni and Peter Hänggi. Driven quantum tunneling. *Physics Reports*, 304(5):229–354, 1998.

- [12] Andreas Buchleitner, Dominique Delande, and Jakub Zakrzewski. Non-dispersive wave packets in periodically driven quantum systems. *Physics Reports*, 368(5):409–547, 2002.
- [13] O. Zobay and B. M. Garraway. Two-dimensional atom trapping in field-induced adiabatic potentials. *Phys. Rev. Lett.*, 86:1195–1198, Feb 2001.
- [14] O. Zobay and B. M. Garraway. Atom trapping and two-dimensional Bose-Einstein condensates in field-induced adiabatic potentials. *Phys. Rev. A*, 69:023605, Feb 2004.
- [15] D.C. Aveline, J.R. Williams, E.R. Elliott, and et al. Observation of Bose–Einstein condensates in an Earth-orbiting research lab. *Nature*, 582:193–197, Jun 2020.
- [16] N. Lundblad, R.A. Carollo, C. Lannert, and et al. Shell potentials for microgravity Bose-Einstein condensates. *npj Microgravity*, 5:30, Dec 2019.
- [17] R. A. Carollo, D. C. Aveline, B. Rhyno, S. Vishveshwara, J. D. Murphree C. Lannert, E. R. Elliott, J. R. Williams, R. J. Thompson, and N. Lundblad. Observation of ultracold atomic bubbles in orbital microgravity. *Nature*, 606:281–286, May 2022.
- [18] Alex Andriati, Leonardo Brito, Lauro Tomio, and Arnaldo Gammal. Stability of a Bose-condensed mixture on a bubble trap. *Phys. Rev. A*, 104:033318, Sep 2021.
- [19] Leonardo Brito, Lauro Tomio, and Arnaldo Gammal. Faraday waves on a bubble Bose-Einstein condensed binary mixture. *e-print arXiv:2309.14878*, 2023.
- [20] Leonardo Brito da Silva and Emanuel Fernandes de Lima. Coherent control of nonlinear mode transitions in Bose–Einstein condensates. *Journal of Physics B: Atomic, Molecular and Optical Physics*, 53(12):125302, may 2020.
- [21] Leonardo Brito, Alex Andriati, Lauro Tomio, and Arnaldo Gammal. Breakup of rotating asymmetric quartic-quadratic trapped condensates. *Phys. Rev. A*, 102:063330, Dec 2020.
- [22] Oliver Penrose and Lars Onsager. Bose-Einstein condensation and liquid helium. *Phys. Rev.*, 104:576–584, Nov 1956.
- [23] N. N. Bogoliubov. On the theory of superfluidity. *J. Phys. USSR*, 11:23, 1947.
- [24] David J. Griffiths and Darrell F. Schroeter. *Introduction to Quantum Mechanics*. Cambridge University Press, 3 edition, 2018.

- [25] Zhaopin Chen, Yongyao Li, Nikolaos P Proukakis, and Boris A Malomed. Immiscible and miscible states in binary condensates in the ring geometry. *New Journal of Physics*, 21(7):073058, jul 2019.
- [26] S. Chandrasekhar. *Hydrodynamic and Hydromagnetic Stability*. Oxford University Press, London, 1961.
- [27] Terun Chen, Kosuke Shibata, Yujiro Eto, Takuya Hirano, and Hiroki Saito. Faraday patterns generated by Rabi oscillation in a binary Bose-Einstein condensate. *Phys. Rev. A*, 100:063610, Dec 2019.
- [28] Huan Zhang, Sheng Liu, and Yong-Sheng Zhang. Faraday patterns in spin-orbit-coupled Bose-Einstein condensates. *Phys. Rev. A*, 105:063319, Jun 2022.
- [29] T. van Zoest et al. Bose-Einstein condensation in microgravity. *Science*, 328(5985):1540–1543, 2010.
- [30] K. Frye, S. Abend, W. Bartosch, and et al. The Bose-Einstein condensate and Cold Atom Laboratory. *EPJ Quantum Technol*, 8:1, Jan 2021.
- [31] N. Lundblad et al. Perspective on quantum bubbles in microgravity. *Quantum Sci. Technol.*, 8, Feb 2023.
- [32] A. Wolf, P. Boegel, M. Meister, A. Balaž, N. Gaaloul, and M. A. Efremov. Shell-shaped Bose-Einstein condensates based on dual-species mixtures. *Phys. Rev. A*, 106:013309, Jul 2022.
- [33] F. Jia et al. Expansion dynamics of a shell-shaped Bose-Einstein condensate. *Phys. Rev. Lett.*, 129:243402, Dec 2022.
- [34] Yanliang Guo, Emmanuel Mercado Gutierrez, David Rey, Thomas Badr, Aurélien Perrin, Laurent Longchambon, Vanderlei Salvador Bagnato, H el ene Perrin, and Romain Dubessy. Expansion of a quantum gas in a shell trap. *New Journal of Physics*, 24(9):093040, oct 2022.
- [35] Y. Colombe, E. Knyazchyan, O. Morizot, B. Mercier, V. Lorent, and H. Perrin. Ultracold atoms confined in rf-induced two-dimensional trapping potentials. *Europhysics Letters*, 67(4):593, aug 2004.
- [36] Barry M Garraway and H el ene Perrin. Recent developments in trapping and manipulation of atoms with adiabatic potentials. *Journal of Physics B: Atomic, Molecular and Optical Physics*, 49(17):172001, aug 2016.
- [37] H el ene Perrin and Barry M. Garraway. Advances in atomic, molecular, and optical physics. In Ennio Arimondo, Chun C. Lin, and Susanne F. Yelin, editors, *Chapter Four - Trapping Atoms With Radio Frequency Adiabatic Potentials*,

volume 66 of *Advances In Atomic, Molecular, and Optical Physics*, pages 181–262. Academic Press, 2017.

- [38] H. Müntinga et al. Interferometry with Bose-Einstein condensates in microgravity. *Phys. Rev. Lett.*, 110:093602, Feb 2013.
- [39] D. Schlippert, J. Hartwig, H. Albers, L. L. Richardson, C. Schubert, A. Roura, W. P. Schleich, W. Ertmer, and E. M. Rasel. Quantum test of the universality of free fall. *Phys. Rev. Lett.*, 112:203002, May 2014.
- [40] Jan Rudolph et al. A high-flux bec source for mobile atom interferometers. *New Journal of Physics*, 17:065001, jun 2015.
- [41] D. Becker et al. Space-borne Bose–Einstein condensation for precision interferometry. *Nature*, 562:391–395, Oct 2018.
- [42] G. Condon, M. Rabault, B. Barrett, L. Chichet, R. Arguel, H. Eneriz-Imaz, D. Naik, A. Bertoldi, B. Battelier, P. Bouyer, and A. Landragin. All-optical Bose-Einstein condensates in microgravity. *Phys. Rev. Lett.*, 123:240402, Dec 2019.
- [43] Christian Vogt, Marian Woltmann, Sven Herrmann, Claus Lämmerzahl, Henning Albers, Dennis Schlippert, and Ernst M. Rasel. Evaporative cooling from an optical dipole trap in microgravity. *Phys. Rev. A*, 101:013634, Jan 2020.
- [44] Maïke D. Lachmann and Ernst M. Rasel. Quantum matter orbits Earth. *Nature*, 582:186–187, Jun 2020.
- [45] Christian Deppner et al. Collective-mode enhanced matter-wave optics. *Phys. Rev. Lett.*, 127:100401, Aug 2021.
- [46] M.D. Lachmann et al. Ultracold atom interferometry in space. *Nat Commun*, 12:1317, Feb 2021.
- [47] Naceur Gaalouol et al. A space-based quantum gas laboratory at picokelvin energy scales. *Nat Commun*, 13:7889, Dec 2022.
- [48] R. J. Thompson et al. Exploring the quantum world with a third generation ultra-cold atom facility. *Quantum Science and Technology*, 8(1):014007, dec 2022.
- [49] A. Tononi and L. Salasnich. Bose-Einstein condensation on the surface of a sphere. *Phys. Rev. Lett.*, 123:160403, Oct 2019.
- [50] A. Tononi, F. Cinti, and L. Salasnich. Quantum bubbles in microgravity. *Phys. Rev. Lett.*, 125:010402, Jun 2020.

- [51] A. Tononi. Scattering theory and equation of state of a spherical two-dimensional Bose gas. *Phys. Rev. A*, 105:023324, Feb 2022.
- [52] Andrea Tononi, Axel Pelster, and Luca Salasnich. Topological superfluid transition in bubble-trapped condensates. *Phys. Rev. Res.*, 4:013122, Feb 2022.
- [53] A. Tononi and L. Salasnich. Low-dimensional quantum gases in curved geometries. *Nat Rev Phys*, 5:398–406, Jul 2023.
- [54] C. Lannert, T.-C. Wei, and S. Vishveshwara. Dynamics of condensate shells: Collective modes and expansion. *Phys. Rev. A*, 75:013611, Jan 2007.
- [55] Kuei Sun, Karmela Padavić, Frances Yang, Smitha Vishveshwara, and Courtney Lannert. Static and dynamic properties of shell-shaped condensates. *Phys. Rev. A*, 98:013609, Jul 2018.
- [56] Karmela Padavić, Kuei Sun, Courtney Lannert, and Smitha Vishveshwara. Physics of hollow Bose-Einstein condensates. *Europhysics Letters*, 120(2):20004, jan 2018.
- [57] Karmela Padavić, Kuei Sun, Courtney Lannert, and Smitha Vishveshwara. Vortex-antivortex physics in shell-shaped Bose-Einstein condensates. *Phys. Rev. A*, 102:043305, Oct 2020.
- [58] Brendan Rhyno, Nathan Lundblad, David C. Aveline, Courtney Lannert, and Smitha Vishveshwara. Thermodynamics in expanding shell-shaped Bose-Einstein condensates. *Phys. Rev. A*, 104:063310, Dec 2021.
- [59] Sálvio Jacob Bereta, Lucas Madeira, Vanderlei S. Bagnato, and Mônica A. Caracanhas. Bose–Einstein condensation in spherically symmetric traps. *American Journal of Physics*, 87(11):924–934, 2019.
- [60] Natália S Móller, F Ednilson A dos Santos, Vanderlei S Bagnato, and Axel Pelster. Bose–Einstein condensation on curved manifolds. *New Journal of Physics*, 22(6):063059, jun 2020.
- [61] Elias J. P. Biral, Natália S. Móller, Axel Pelster, and F. Ednilson A. dos Santos. Bose-Einstein condensates and the thin-shell limit in anisotropic bubble traps, 2022.
- [62] P.C. Diniz, E.A.B. Oliveira, A.R.P. Lima, and et al. Ground state and collective excitations of a dipolar Bose-Einstein condensate in a bubble trap. *Sci Rep*, 10:4831, Mar 2020.
- [63] Sálvio J. Bereta, Mônica A. Caracanhas, and Alexander L. Fetter. Superfluid vortex dynamics on a spherical film. *Phys. Rev. A*, 103:053306, May 2021.

- [64] Mônica A. Caracanhas, Pietro Massignan, and Alexander L. Fetter. Superfluid vortex dynamics on an ellipsoid and other surfaces of revolution. *Phys. Rev. A*, 105:023307, Feb 2022.
- [65] Guilherme Tomishiyo, Lucas Madeira, and Mônica A. Caracanhas. Superfluid excitations in a rotating two-dimensional bubble trap, 2022.
- [66] D. S. Hall, M. R. Matthews, C. E. Wieman, and E. A. Cornell. Measurements of relative phase in two-component Bose-Einstein condensates. *Phys. Rev. Lett.*, 81:1543–1546, Aug 1998.
- [67] Víctor M. Pérez-García, Humberto Michinel, and Henar Herrero. Bose-Einstein solitons in highly asymmetric traps. *Phys. Rev. A*, 57:3837–3842, May 1998.
- [68] L. Amico et al. Roadmap on atomtronics: State of the art and perspective. *e-print arXiv:2008.04439*, 2021.
- [69] Marijana Brtko, Arnaldo Gammal, and Boris A. Malomed. Hidden vorticity in binary Bose-Einstein condensates. *Phys. Rev. A*, 82:053610, Nov 2010.
- [70] M. Abramowitz and I. A. Stegun. *Handbook of Mathematical Functions with Formulas, Graphs, and Mathematical Tables*. Dover, New York, 9 edition, 1972.
- [71] George B. Arfken, Hans J. Weber, and Frank E. Harris. *Mathematical Methods for Physicists*. Academic Press, Boston, 7 edition, 2012.
- [72] M. Greiner, O. Mandel, T. Hänsch, and et al. Collapse and revival of the matter wave field of a Bose–Einstein condensate. *Nature*, 419, Apr 2002.
- [73] M. C. Cross and P. C. Hohenberg. Pattern formation outside of equilibrium. *Rev. Mod. Phys.*, 65:851–1112, Jul 1993.
- [74] XVII M. Faraday. On a peculiar class of acoustical figures; and on certain forms assumed by groups of particles upon vibrating elastic surfaces. *Phil. Trans. R. Soc.*, 121:299–340, Jan 1831.
- [75] P. Engels, C. Atherton, and M. A. Hofer. Observation of Faraday waves in a Bose-Einstein condensate. *Phys. Rev. Lett.*, 98:095301, Feb 2007.
- [76] J. Smits, L. Liao, H. T. C. Stoof, and P. van der Straten. Observation of a space-time crystal in a superfluid quantum gas. *Phys. Rev. Lett.*, 121:185301, Oct 2018.

- [77] J. H. V. Nguyen, M. C. Tsatsos, D. Luo, A. U. J. Lode, G. D. Telles, V. S. Bagnato, and R. G. Hulet. Parametric excitation of a Bose-Einstein condensate: From Faraday waves to granulation. *Phys. Rev. X*, 9:011052, Mar 2019.
- [78] Z. Zhang, KX. Yao, L. Feng, and et al. Pattern formation in a driven Bose-Einstein condensate. *Nat. Phys.*, 16:652–656, Oct 2018.
- [79] R. Cominotti, A. Berti, A. Farolfi, A. Zenesini, G. Lamporesi, I. Carusotto, A. Recati, and G. Ferrari. Observation of massless and massive collective excitations with Faraday patterns in a two-component superfluid. *Phys. Rev. Lett.*, 128:210401, May 2022.
- [80] Chen-Xi Zhu, Wei Yi, Guang-Can Guo, and Zheng-Wei Zhou. Parametric resonance of a Bose-Einstein condensate in a ring trap with periodically driven interactions. *Phys. Rev. A*, 99:023619, Feb 2019.
- [81] Stewart D. Jenkins and T. A. Brian Kennedy. Spin squeezing in a driven Bose-Einstein condensate. *Phys. Rev. A*, 66:043621, Oct 2002.
- [82] Stewart D. Jenkins and T. A. B. Kennedy. Dynamic stability of dressed condensate mixtures. *Phys. Rev. A*, 68:053607, Nov 2003.
- [83] Kosuke Shibata, Aki Torii, Hitoshi Shibayama, Yujiro Eto, Hiroki Saito, and Takuya Hirano. Interaction modulation in a long-lived Bose-Einstein condensate by rf coupling. *Phys. Rev. A*, 99:013622, Jan 2019.
- [84] C. J. Myatt, E. A. Burt, R. W. Ghrist, E. A. Cornell, and C. E. Wieman. Production of two overlapping Bose-Einstein condensates by sympathetic cooling. *Phys. Rev. Lett.*, 78:586–589, Jan 1997.
- [85] G. Modugno, M. Modugno, F. Riboli, G. Roati, and M. Inguscio. Two atomic species superfluid. *Phys. Rev. Lett.*, 89:190404, Oct 2002.
- [86] B. Diu C. Cohen-Tannoudji and F. Laloe. *Quantum Mechanics*. John Wiley & Sons, New York, 1977.
- [87] L. D. Landau and E. M. Lifshitz. *Mechanics*. Elsevier Butterworth-Heinemann, 3 edition, 1976.
- [88] A. Gammal and A. Pelster. Workshop. In *Workshop on Low Dimensional Quantum Gases*, Principia Institute, São Paulo, 2023. ICTP-SAIFR.
- [89] D. Quinney. *An Introduction to the Numerical Solution of Differential Equations*. Applied and engineering mathematics series. Research Studies Press, Letchworth, Hertfordshire, England, 1987.

- [90] Paul L. DeVries. *A first course in computational physics*. John Wiley & Sons, Inc., United States of America, 1994.
- [91] William H. Press et al. *Numerical Recipes in Fortran The Art of Scientific Computing*. Cambridge University Press, United States of America, 1992.
- [92] W. F. Ames. *Numerical Methods for Partial Differential Equations*. Academic Press, New York, 3 edition, 1992.
- [93] P. Muruganandam and S.K. Adhikari. Fortran programs for the time-dependent Gross–Pitaevskii equation in a fully anisotropic trap. *Computer Physics Communications*, 180(10):1888 – 1912, 2009.
- [94] J. J. Sakurai and Jim Napolitano. *Modern Quantum Mechanics*. Cambridge University Press, 2 edition, 2017.



# Appendix A

## Methods

Here we present some of the methods to solve the mean-field problems in the closed geometries of an ideal spherical shell. All methods are mainly based on finite differences (FD) schemes [89] adapted to spherical coordinates. We also introduce a new kind of pseudo-spectral method [90] developed in [18], which is a tricky combination of FD approach and Fast Fourier Transform (FFT) [91] method. In the next sections, the interaction parameters are mainly denoted by  $g$  or  $g_{jk}$ ,  $j, k = 1, 2$  for binary mixtures, while in the main text, these symbols can be eventually changed depending on the problem, in order to keep most of the symbols used in the published papers. We already have written our problems in dimensionless form in the main text, but we can also stress out that for equations not discussed before, we consider the unit for masses and Planck constant (divided by  $2\pi$ )  $M = M_1 = M_2 = \hbar = 1$ .

This chapter is organized as follows. In Sec. A.1, we present the split step method, describing how we separate the derivative from nonderivative part of the problem and solve them by different methods. In Sec. A.2, we introduce our original method to handle the 2D angular problem, by combining spectral and finite differences methods. We present in Sec. A.3, how we solve 1D equation in the polar-angular part of the Hamiltonian when we assume azimuthal symmetry. For one-dimensional problem, we depict in Sec. A.4, how we perform the BdG approach to study stability of the solutions. In Sec. A.5, we show how to solve the problem of spatial-homogeneous time-periodic solutions by 4th order Runge-Kutta method. And finally, in Sec. A.6, we present the Floquet method to study the stability of homogeneous periodic solutions.

### A.1 Split-Step method

The Nonlinear Schrödinger equation (NLSE) provided by the mean-field approach to describe a BEC can be solved by dividing the problem into two parts, which are the derivative part and the nonderivative one. Actually, we solve them by different methods [92, 93]. For convenience, we formulate the problem for a binary BEC mixture, but it can be easily extended to a single species system, just setting the

extra terms as zero. Once we have each species  $j$  ( $j = 1, 2$ ) driven by NLSE

$$i \frac{\partial \psi_j}{\partial t}(\mathbf{r}, t) = \mathbf{H}^{(j)} \psi_j(\mathbf{r}, t), \quad (\text{A.1})$$

if the Hamiltonian  $\mathbf{H}^{(j)}$  has two parts, the derivative  $\mathbf{H}_d^{(j)}$  and nonderivative  $\mathbf{H}_{nd}^{(j)}$

$$\mathbf{H}^{(j)} = \mathbf{H}_d^{(j)} + \mathbf{H}_{nd}^{(j)}, \quad (\text{A.2})$$

then the GP equations has two steps

$$i \frac{\partial \psi_j}{\partial t}(\mathbf{r}, t) = \mathbf{H}_d^{(j)} \psi_j(\mathbf{r}, t), \quad (\text{A.3a})$$

$$i \frac{\partial \psi_j}{\partial t}(\mathbf{r}, t) = \mathbf{H}_{nd}^{(j)} \psi_j(\mathbf{r}, t). \quad (\text{A.3b})$$

We operate on the wave functions by two different evolution operators  $\mathbf{U}_d$  and  $\mathbf{U}_{nd}$ , derivative and nonderivative, respectively. The wave functions  $\psi_{1,2}$  evolve in time from  $t_0$  to  $t = t_0 + dt$  by two nonderivative time half-steps  $dt/2$  and one derivative time step  $dt$

$$\psi_j(\mathbf{r}, t) = \mathbf{U}_{nd}^{(j)}(dt/2) \mathbf{U}_d^{(j)}(dt) \mathbf{U}_{nd}^{(j)}(dt/2) \psi_j(\mathbf{r}, t_0). \quad (\text{A.4})$$

The nonderivative terms  $\mathbf{H}_{nd}^{(j)}$  include the trap potential  $V_{trap}$ , interaction potential  $\mathbf{H}_{int}^{(j)}$ , and also the Rabi Coupling  $\mathbf{H}_R^{(j)}$

$$\mathbf{H}_{nd}^{(j)} = V_{trap} + \mathbf{H}_{int}^{(j)} + \mathbf{H}_R^{(j)}, \quad (\text{A.5})$$

where

$$\mathbf{H}_{int}^{(j)}(\mathbf{r}, t) = \sum_{k=1,2} g_{jk}(t) |\psi_k(\mathbf{r}, t)|^2, \quad (\text{A.6})$$

and

$$\mathbf{H}_R^{(j)}(\mathbf{r}, t) = -(-1)^{3-j} i \Omega \psi_{3-j}(\mathbf{r}, t). \quad (\text{A.7})$$

For small time steps ( $dt \ll 1$ ), the evolution interaction operator is approximately the exponential operator of the time-independent Hamiltonian case [94], and we can merge the trap and interaction terms in a single operator  $\mathbf{H}_{trap+int}^{(j)} = V_{trap} + \mathbf{H}_{int}^{(j)}$

$$\mathbf{U}_{trap+int}^{(j)}(dt) = \exp\left(-idt \mathbf{H}_{trap+int}^{(j)}\right), \quad (\text{A.8})$$

we can not explicitly write the Rabi evolution operator  $\mathbf{U}_R^{(j)}$  for each species  $j$ , but we can write down how it operates on each wave function

$$\mathbf{U}_R^{(j)}(dt) \psi_j(t) = \cos(\Omega dt) \psi_j(\mathbf{r}, t) + (-1)^j \sin(\Omega dt) \psi_{3-j}(\mathbf{r}, t). \quad (\text{A.9})$$

In summary, we can write the nonderivative operator in a pictorial way as a single operator  $\mathbf{U}_{nd}^{(j)}(dt) = \mathbf{U}_R^{(j)}(dt)\mathbf{U}_{trap+int}^{(j)}(dt)$ . The derivative Hamiltonians  $\mathbf{H}_d^{(j)}$  are the Laplacians

$$\mathbf{H}_d^{(j)} = -\frac{1}{2}\nabla_{r_j}^2, \quad (\text{A.10})$$

but we need a different method to solve it. These schemes can be changed depending on boundary conditions, singularities, the order of derivative terms, etc. In general, we can not explicit the evolution operator  $\mathbf{U}_d^{(j)}$ , but we can calculate how it actually operates on the wave functions.

We formulate the problem for real time, i.e, we set the equations to perform the dynamics of the system, but if we consider an imaginary time defined by  $t = -i\tau$ , and we renormalize the wave function every time step, we can find the ground state of the system [93], which is usually called *Relaxation Method*.

## A.2 Two-dimensional spherical shell: Spectral and finite differences method

Consider the spatial discretization  $\theta_p = (p - 1)d\theta$  and  $\phi_q = (q - 1)d\phi$ , and the time discretization  $t_n = (n - 1)dt$  then the wave function is fully described in the discretized system by  $\psi(\theta_p, \phi_q, t_n) = \psi_{p,q}^n$ , where  $p = 1, \dots, N_\theta + 1$ ,  $q = 1, \dots, N_\phi + 1$ , and  $n = 1, \dots, N_T + 1$ , with  $N_\theta = \pi/d\theta$ ,  $N_\phi = 2\pi/d\phi$ ,  $N_T = T/dt$ . The steps sizes  $d\theta$ ,  $d\phi$ , and  $dt$  are chosen according to the required precision. The linear equations we want to solve is

$$c \frac{\partial \psi_j}{\partial t} = -\frac{1}{2} \frac{1}{\sin \theta} \frac{\partial}{\partial \theta} \left( \sin \theta \frac{\partial \psi_j}{\partial \theta} \right) + \frac{1}{2} \frac{1}{\sin^2 \theta} \frac{\partial^2 \psi_j}{\partial \phi^2}, \quad (\text{A.11})$$

with  $c = i$  for a real-time propagation and  $c = -1$  for an imaginary-time propagation. We take the Fourier Transform of  $\psi$  in the  $\phi$  - direction

$$\psi_j(\theta, \phi, t) = \sum_{k_\phi} e^{ik_\phi \phi} \tilde{\psi}_{j,k_\phi}(\theta, t), \quad (\text{A.12})$$

and we get a one-dimensional equation in the transformed space

$$c \frac{\partial \tilde{\psi}_{j,k_\phi}}{\partial t} = -\frac{1}{2} \frac{1}{\sin \theta} \frac{\partial}{\partial \theta} \left( \sin \theta \frac{\partial \tilde{\psi}_{j,k_\phi}}{\partial \theta} \right) - \frac{1}{2} \frac{k_\phi^2}{\sin^2 \theta} \tilde{\psi}_{j,k_\phi}, \quad (\text{A.13})$$

then, once we solve it for each  $k_\phi$ , we are able to get the full wave function  $\psi_j$ .

## A.3 Polar-direction finite differences

Once we consider an ansatz with an azimuthal symmetry in  $\phi$  - coordinate, we have to solve just a single one-dimensional equation for the polar  $\theta$  - coordinate. In the

last Section A.2, we had split a 2D problem in an array of  $N_\phi + 1$  1D equations. In such a way that, for which  $\phi$  - coordinate, we had the ansatz  $\psi = e^{ik_\phi\phi}\tilde{\psi}_{j,k_\phi}(\theta, t)$ . A pretty much easier problem is to considerate that we have a well-defined vorticity  $s_j$  given by the vortex charge in vortex-states for each species  $j$ . In this case, we have  $k_\phi = s_j$  for all values of the coordinate  $\phi$ . It returns an unique explicit dependency on the  $\phi$  variable, then we get an effective one-dimensional problem, and we do not need to split the derivative term of the Hamiltonian into the  $\theta$  and  $\phi$  variables, then it is straightforward to solve the problem by the FD scheme. Therefore, we have to solve only one partial differential equation regarding the function  $\tilde{\psi}_{j,s_j} = f_j(\theta, t)$ . Although we are working with two species, we are going to solve the linear part of the GP equation in the same way for each species separately. Then, for simplicity we denote  $f_j \rightarrow f$ . From now on, the subscripts indexes only stand for spatial-grid discretized indexes

$$c \frac{\partial f}{\partial t} = -\frac{1}{2} \frac{1}{\sin \theta} \frac{\partial}{\partial \theta} \left( \sin \theta \frac{\partial f}{\partial \theta} \right) + \frac{1}{2} \frac{s_j^2}{\sin^2 \theta} f, \quad (\text{A.14})$$

or

$$c \frac{\partial f}{\partial t} = -\frac{1}{2} \frac{\partial^2 f}{\partial \theta^2} - \frac{1}{2} \cot \theta \frac{\partial f}{\partial \theta} + \frac{1}{2} \frac{s_j^2}{\sin^2 \theta} f. \quad (\text{A.15})$$

Nevertheless, we have poles which raise some troubles with singularities, and we have to deal with them. We can set a spatial discretization  $\theta_p = (p - 1)d\theta$ , where  $p = 1, \dots, N_\theta + 1$  and  $d\theta = \pi/N_\theta$  and the time discretization  $t_n = (n - 1)dt$ , where  $n = 1, \dots, N_T$ . The  $(N_\theta + 1)$  and  $(N_T + 1)$  quantities define the size of the grid. The total period is  $T$ , then  $dt = T/N_T$ , with  $N_T$  the number of time steps. We can address the function  $f(\theta, t) = f_p^n$ . Then by trapezium method and CN scheme [89], we can write our problem as

$$f_p^{n+1} = f_p^n - \frac{dt}{4c} \left[ \frac{1}{d\theta^2} \delta_\theta^2 + \frac{\cot \theta}{2d\theta} \delta_\theta - \frac{s_j^2}{\sin^2 \theta} \right] (f_p^{n+1} + f_p^n), \quad (\text{A.16})$$

where  $\delta_\theta^2 f_p^n = (f_{p+1}^n - 2f_p^n + f_{p-1}^n)$  and  $\delta_\theta f_p^n = (f_{p+1}^n - f_{p-1}^n)$ . We also can rewrite Eq. (A.16) as

$$\begin{aligned} \left( 1 + \frac{d\theta \cot \theta_p}{2} \right) f_{p+1}^{n+1} &+ \left( \alpha_\theta - 2 - \frac{s_j^2 d\theta^2}{\sin^2 \theta_p} \right) f_p^{n+1} + \left( 1 - \frac{d\theta \cot \theta_p}{2} \right) f_{p-1}^{n+1} \\ &= - \left( 1 + \frac{d\theta \cot \theta_p}{2} \right) f_{p+1}^n + \left( \alpha_\theta + 2 + \frac{s_j^2 d\theta^2}{\sin^2 \theta_p} \right) f_p^n \\ &- \left( 1 - \frac{d\theta \cot \theta_p}{2} \right) f_{p-1}^n, \end{aligned} \quad (\text{A.17})$$

with  $\alpha_\theta = 4cd\theta^2/dt$ . Note we have singularities at the poles  $\theta = 0$ , and  $\pi$ , or at the discrete points  $p = 1$  and  $p = N_\theta + 1$ , since we have  $1/\sin \theta \rightarrow \infty$  and  $\cot \theta \rightarrow \infty$

at this points. If we consider the cases where the vorticity is different from zero, i.e,  $s_j \neq 0$ , the solutions have density going to zero at the poles, since we have vortices in these regions, then we can just drop the first/last rows/columns. And therefore, we get the system in the matrix form

$$\begin{pmatrix} \gamma_2^- & \beta_2^+ & & \\ \beta_2^- & \ddots & \ddots & \\ & \ddots & \ddots & \beta_{N_\theta}^+ \\ & & \beta_{N_\theta}^- & \gamma_{N_\theta}^- \end{pmatrix} \begin{pmatrix} f_2^{n+1} \\ f_3^{n+1} \\ \vdots \\ f_{N_\theta}^{n+1} \end{pmatrix} = \begin{pmatrix} \gamma_2^+ & \beta_2^- & & \\ \beta_2^+ & \ddots & \ddots & \\ & \ddots & \ddots & \beta_{N_\theta}^- \\ & & \beta_{N_\theta}^+ & \gamma_{N_\theta}^+ \end{pmatrix} \begin{pmatrix} f_2^n \\ f_3^n \\ \vdots \\ f_{N_\theta}^n \end{pmatrix}, \quad (\text{A.18})$$

where blank spaces are zero elements and

$$\beta_p^\pm = 1 \pm d\theta \cot \theta_p/2, \quad (\text{A.19a})$$

$$\gamma_p^\pm = \alpha_\theta \pm (2 + s_j^2 d\theta^2 / \sin^2 \theta_p). \quad (\text{A.19b})$$

But when we have  $s_j = 0$ , the system have no vortices, and the density does not go to zero at the poles, then we have to handle the singularities. We set the values of the solution at the poles by considering forward and backward substitutions [89], since we can state the derivative condition  $df(\theta)/d\theta = 0$  at the poles. Then we get the first point (by forward substitution) and the last one (by backward substitution)

$$f_1 = \frac{4f_2 - f_3}{3}, \quad f_{N_\theta+1} = \frac{4f_{N_\theta} - f_{N_\theta-1}}{3}. \quad (\text{A.20})$$

The system in the matrix form must not contain the divergent terms at the first and last points. Then we get

$$\begin{pmatrix} \gamma_1^- & \beta_1^+ & & \\ \beta_1^- & \ddots & \ddots & \\ & \ddots & \ddots & \beta_{N_\theta+1}^+ \\ & & \beta_{N_\theta+1}^- & \gamma_{N_\theta+1}^- \end{pmatrix} \begin{pmatrix} f_1^{n+1} \\ f_2^{n+1} \\ \vdots \\ f_{N_\theta+1}^{n+1} \end{pmatrix} = \begin{pmatrix} \gamma_1^+ & \beta_1^- & & \\ \beta_1^+ & \ddots & \ddots & \\ & \ddots & \ddots & \beta_{N_\theta+1}^- \\ & & \beta_{N_\theta+1}^+ & \gamma_{N_\theta+1}^+ \end{pmatrix} \begin{pmatrix} f_1^n \\ f_2^n \\ \vdots \\ f_{N_\theta+1}^n \end{pmatrix}, \quad (\text{A.21})$$

but with the first and last terms adapted to

$$\beta_1^\pm = \beta_{N_\theta+1}^\pm = 2, \quad (\text{A.22a})$$

$$\gamma_1^\pm = \gamma_{N_\theta+1}^\pm = \alpha_\theta \pm 2, \quad (\text{A.22b})$$

another points follow the rule of the Eq. (A.19). All these matrices are tridiagonal and can be solved by LU decomposition method [89]. In summary, if we want to solve the 2D problem or a 1D problem with azimuthal symmetry given by the well-defined vorticity, we have to use the same method. However, in the 2D problem we have the solve much more equations, once for each  $k_\phi$ -variable we have a different equation to solve.

## A.4 Polar-direction Bogoliubov de-Gennes method

We can see the BdG equations in the  $\mathbf{M}$  matrix (4.27). In the grid-space, each of the matrix elements are square  $(N_\theta + 1) \times (N_\theta + 1)$  matrix blocks and  $\mathbf{M}$  is a  $(4N_\theta + 4) \times (4N_\theta + 4)$  square matrix. We have 16 block elements, then for short, we write only some of them. We suppose to observe the boundary conditions of the modes  $\{u_{1,m}(\theta), v_{1,m}(\theta), u_{2,m}(\theta), v_{2,m}(\theta)\}$ , they follow the required conditions based on the equations (4.29), i.e,  $(m + s_1)$ ,  $(m - s_1)$ ,  $(m + s_2)$  and  $(m - s_2)$ , respectively. When the factor  $(m \pm s_j) = 0$ , the corresponding mode does not go to zero at the poles, but if  $(m + s_j) \neq 0$ , the mode goes to zero at the poles.

For example, the  $M_{1,1} = \hat{D}_1^+$  element based on Eq. (4.29) is

$$M_{(1,1)} = \begin{pmatrix} \bar{\gamma}_1^{(1)} & \bar{\beta} & & & \\ \tilde{\beta}_2^+ & \tilde{\gamma}_2^{(1,+)} & \tilde{\beta}_2^- & & \\ \cdots & \cdots & \cdots & & \\ & \tilde{\beta}_{N_\theta}^+ & \tilde{\gamma}_{N_\theta}^{(1,+)} & \tilde{\beta}_{N_\theta}^- & \\ & & \bar{\beta} & \bar{\gamma}_{N_{\theta+1}}^{(1)} & \end{pmatrix}, \quad (\text{A.23})$$

which is valid only when we have  $(m + s_1) = 0$ , because the eigenvectors of the matrix do not are zero at the poles. But when  $(m + s_1) \neq 0$ , the eigenvectors are zero at the poles, then the matrix is reduced to

$$M_{(1,1)} = \begin{pmatrix} & & & & \\ \tilde{\beta}_2^+ & \tilde{\gamma}_2^{(1,+)} & \tilde{\beta}_2^- & & \\ \cdots & \cdots & \cdots & & \\ & \tilde{\beta}_{N_\theta}^+ & \tilde{\gamma}_{N_\theta}^{(1,+)} & \tilde{\beta}_{N_\theta}^- & \\ & & & & \end{pmatrix}, \quad (\text{A.24})$$

with

$$\tilde{\beta}_p^{(\pm)} = -0.5 \frac{1}{d\theta^2} \pm 0.25 \frac{\cot \theta_p}{d\theta}, \quad (\text{A.25a})$$

$$\bar{\beta} = -\frac{1}{d\theta^2}, \quad (\text{A.25b})$$

$$\tilde{\gamma}_p^{(j,\pm)} = \frac{1}{d\theta^2} + 0.5 \frac{(m \pm s_j)^2}{\sin^2 \theta_p} + \frac{1}{2\pi} (2g_{jj} + g_{jk}) f_p^2 - \mu_j, \quad (\text{A.25c})$$

$$\bar{\gamma}_p^{(j)} = \frac{1}{d\theta^2} + \frac{1}{2\pi} (2g_{jj} + g_{jk}) f_p^2 - \mu_j. \quad (\text{A.25d})$$

Another example can be a nondiagonal term in the matrix  $\mathbf{M}$ , we take the  $M_{(1,2)} =$

$g_{11}f^2$  from Eq. (4.27) element when  $(m - s_1) = 0$

$$M_{(1,2)} = \begin{pmatrix} \tilde{g}_{11}f_1^2 & & & \\ & \ddots & & \\ & & \ddots & \\ & & & \tilde{g}_{11}f_{N_\theta+1}^2 \end{pmatrix}, \quad (\text{A.26})$$

or when  $(m - s_1) \neq 0$

$$M_{(1,2)} = \begin{pmatrix} & & & & \\ & \tilde{g}_{11}f_2^2 & & & \\ & & \ddots & & \\ & & & \ddots & \\ & & & & \tilde{g}_{11}f_{N_\theta}^2 \end{pmatrix}, \quad (\text{A.27})$$

where  $\tilde{g}_{jk} = g_{jk}/2\pi$  and  $j, k = 1, 2$ . We have a fixed vorticity parameter  $s$ , and  $s_1 = -s_2 = s$ , then we choose a specific mode  $m$  and track it, observing the spectrum. In this process, we vary the interaction parameters and the protocol to study the dynamic stability is to observe if the matrix  $\mathbf{M}$  has at least one eigenvalue with imaginary part different from zero. If so, we consider the system as dynamically unstable, once a complex eigenvalue means that an unstable mode exponentially grows with time.

## A.5 Spatial-homogeneous Time-periodic solutions by Runge-Kutta method

We suppose the condensates in the mixture can be considered spatial-homogeneous, only time-dependent solutions  $\psi_j = \psi_j(t)$  for the GP equations (5.12a) and (5.12b)

$$i\frac{d\psi_1}{dt} = \left[ g|\psi_1|^2 + g_{12}|\psi_2|^2 \right] - i\Omega\psi_2, \quad (\text{A.28a})$$

$$i\frac{d\psi_2}{dt} = \left[ g|\psi_2|^2 + g_{12}|\psi_1|^2 \right] + i\Omega\psi_1. \quad (\text{A.28b})$$

In the discrete formalism, for each time step, we are able to write the wave function solution  $\psi_j(t)$  as  $\psi_j^n$ , where  $t_n = (n-1)dt$ , with  $n = 1, \dots, N_T+1$  and  $N_T = t_f/dt$ . We assume that  $t_f$  is the final time of the simulation, which is performed with a time step  $dt$ . The GP equations (A.28a) and (A.28b) can be written in the matrix form as

$$\frac{d\hat{\psi}^n}{dt} = \hat{F}(\hat{\psi}^n), \quad (\text{A.29})$$

where  $\hat{\psi}$  is a vector with two entries, which stores  $\psi_j$  for each species at the time  $t_n$ , i.e.,  $\hat{\psi} = [\psi_1^n \ \psi_2^n]^T$ . The function  $\hat{F}$  can be written as

$$\hat{F}(\hat{\psi}^n) = -i \begin{pmatrix} g|\psi_1^n|^2 + g_{12}|\psi_2^n|^2 & -i\Omega \\ i\Omega & g|\psi_2^n|^2 + g_{12}|\psi_1^n|^2 \end{pmatrix}. \quad (\text{A.30})$$

We evolve the solutions of both species performing a 4th order Runge-Kutta method. For each time  $t_n$ , we can find the evolved solutions by using the equations (A.31e)

$$\hat{k}_1 = F(\hat{\psi}^n), \quad (\text{A.31a})$$

$$\hat{k}_2 = F(\hat{\psi}^n + dt\hat{k}_1), \quad (\text{A.31b})$$

$$\hat{k}_3 = F(\hat{\psi}^n + dt\hat{k}_2), \quad (\text{A.31c})$$

$$\hat{k}_4 = F(\hat{\psi}^n + dt\hat{k}_3), \quad (\text{A.31d})$$

$$\hat{\psi}^{n+1} = \hat{\psi}^n + \frac{dt}{6} (\hat{k}_1 + 2\hat{k}_2 + 2\hat{k}_3 + \hat{k}_4). \quad (\text{A.31e})$$

This system is periodic since the Rabi coupling induce population oscillations. By considering periodic properties, we observe how the functions  $\psi_j$  evolve in time for a complete period, in order to retrieve the value of the period  $T$ . And in this way, once we assume the solutions are given by  $\psi_j(t) = f_j(t)e^{-i\gamma_j t}$ , following (cite the main text). We are able to get the constants  $\gamma_j$  by comparing the value of  $\psi_j(t = T)$  with  $\psi_j(t = 0)$ , which depends on the initial states. Then, once both values must be the same, we have  $\psi_j(T) = \psi_j(0)e^{-i\gamma_j T}$ . And therefore we write the constant  $\gamma_j$  as a function of the natural logarithm  $\gamma_j = \text{Re}[-i \log(\psi_j(T)/\psi_j(0))/T]$ , or in the discrete formalism  $\gamma_j = \text{Re}[-i \log(\psi_j^{n+1}/\psi_j^1)/T]$ . And finally we are also able to write the function  $f_j$  as  $f_j(t) = e^{i\gamma_j t}\psi_j(t)$ , or  $f_j^n = e^{i\gamma_j t_n}\psi_j^n$ . Actually, both species have almost the same constant  $\gamma_j$ , then we can handle all calculations by considering only one constant  $\gamma_j = \gamma$ .

## A.6 Floquet method for spatial-Homogeneous time-periodic solutions

We are able to solve the Floquet equations by evolving the vector of modes amplitudes  $\mathbf{u}$  by the Floquet matrix  $\tilde{\mathbf{M}}$ . Once we suppose  $\tilde{\mathbf{M}}(t = 0) = \mathbf{1}$ , we must handle the initial conditions  $\mathbf{u}(t = 0) = [1 \ 0]^T$  and  $[0 \ 1]^T$  for a single species problem, and  $\mathbf{u}(t = 0) = [1 \ 0 \ 0 \ 0]^T$ ,  $[0 \ 1 \ 0 \ 0]^T$ ,  $[0 \ 0 \ 1 \ 0]^T$ , and  $[0 \ 0 \ 0 \ 1]^T$  for a binary mixture problem. For each initial condition, we can define vectors  $\mathbf{u}_a$ ,  $\mathbf{u}_b$ ,  $\mathbf{u}_c$ , and  $\mathbf{u}_d$ , and next we individually evolve them from  $t = 0$  to the first complete period  $t = T$ . Once we evolve all possible initial conditions separately, we write a column matrix of all the evolved vectors. For a single species case we have a  $2 \times 2$  matrix  $\mathbf{U} = [\mathbf{u}_a^{N_T+1} \ \mathbf{u}_b^{N_T+1}]$ , and for two-species problem, we have a  $4 \times 4$  matrix  $\mathbf{U} = [\mathbf{u}_a^{N_T+1} \ \mathbf{u}_b^{N_T+1} \ \mathbf{u}_c^{N_T+1} \ \mathbf{u}_d^{N_T+1}]$ . Floquet theorem states that, when we have a linear problem driven by a periodic operator, like  $\tilde{\mathbf{M}}(t)$ , the solution  $\mathbf{u}(t)$  goes with periodic functions  $\mathbf{p}(t)$  as

$$\mathbf{u}(t) = e^{\lambda t} \mathbf{p}(t), \quad (\text{A.32})$$

where both  $\mathbf{u}$  and  $\mathbf{p}$  have the the same period of the operator  $\tilde{\mathbf{M}}$ . The periodic properties can be used in order to obtain the Floquet exponent  $\lambda$ . We get the eigenvalues



$\tilde{\lambda}$  from matrix  $\mathbf{U}$ , and they are related to  $\lambda$  by  $\lambda = \log(\tilde{\lambda}/T)$ . We are able to predict the dynamic stability of the system by evaluating the Floquet exponent. If at least one eigenvalue  $\lambda$  has a positive real part, the system is said to be unstable, once the amplitudes exponentially grow in time, as the protocol introduced in [27]. In the following sections we present the matrix  $\tilde{\mathbf{M}}$  of interest for different physics problems.

We can evaluate the stability profile of the homogeneous time dependent solutions  $f_j$  of the binary mixture with Rabi coupling by observing how the unstable modes evolve in time. In the Appendix section A.5, we have presented how to obtain the solutions  $f_j$ , and here we develop the Floquet method based on these solutions. For each time  $t_n$ , we have a matrix

$$\tilde{\mathbf{M}}(f_1^n, f_2^n) = \begin{pmatrix} D_1^n & g f_1^{n2} & G_{12}^n - i\Omega & g_{12} f_1^n f_2^n \\ -g f_1^{n*2} & -D_1^n & -g_{12} f_1^{n*} f_2^{n*} & -G_{12}^{n*} - i\Omega \\ G_{12}^{n*} + i\Omega & g_{12} f_1^n f_2^n & D_2^n & g f_2^2 \\ -g_{12} f_1^{n*} f_2^{n*} & -G_{12}^n + i\Omega & -g f_2^{n*2} & -D_2^n \end{pmatrix}, \quad (\text{A.33})$$

where  $D_j^n = (\epsilon_\ell - \gamma) + 2g|f_j^n|^2 + g_{12}|f_{j-1}^n|^2$  and  $G_{12}^n = g_{12}f_1^n f_2^{n*}$ . We can define  $\hat{Q}(\mathbf{u}^n) = -i\tilde{\mathbf{M}}(f_1^n, f_2^n)\mathbf{u}^n$ , in such a way that

$$\frac{d}{dt}\mathbf{u}^n = \hat{Q}(\mathbf{u}^n). \quad (\text{A.34})$$

This system can be evolved by a 4th order Runge-Kutta method, where for each time  $t_n$ , the amplitude vector  $\mathbf{u}$  goes with

$$\hat{w}_1 = \hat{Q}(\mathbf{u}^n), \quad (\text{A.35a})$$

$$\hat{w}_2 = \hat{Q}(\mathbf{u}^n + dt\hat{w}_1), \quad (\text{A.35b})$$

$$\hat{w}_3 = \hat{Q}(\mathbf{u}^n + dt\hat{w}_2), \quad (\text{A.35c})$$

$$\hat{w}_4 = \hat{Q}(\mathbf{u}^n + dt\hat{w}_3), \quad (\text{A.35d})$$

$$\mathbf{u}^{n+1} = \mathbf{u}^n + \frac{dt}{6}(\hat{w}_1 + 2\hat{w}_2 + 2\hat{w}_3 + \hat{w}_4). \quad (\text{A.35e})$$